3-1-2019

Application of Metamaterials for Multifunctional Satellite Bus Enabled via Additive Manufacturing

Michael A. Macchia

APPLICATION OF METAMATERIALS FOR MULTIFUNCTIONAL SATELLITE BUS ENABLED VIA ADDITIVE MANUFACTURING

THESIS

Michael A. Macchia, Captain, USAF

AFIT-ENY-MS-19-M-230

DEPARTMENT OF THE AIR FORCE
AIR UNIVERSITY

AIR FORCE INSTITUTE OF TECHNOLOGY

Wright-Patterson Air Force Base, Ohio

AFIT-ENY-MS-19-M-230

APPLICATION OF METAMATERIALS FOR MULTIFUNCTIONAL SATELLITE BUS ENABLED VIA ADDITIVE MANUFACTURING

THESIS

Presented to the Faculty

Department of Aeronautics and Astronautics

Graduate School of Engineering and Management

Air Force Institute of Technology

Air University

Air Education and Training Command

in Partial Fulfillment of the Requirements for the

Degree of Master of Science in Aeronautical Engineering

Michael A. Macchia, M.S.S.E, B.S.A.E

Captain, USAF

March 1, 2019

AFIT-ENY-MS-19-M-230

APPLICATION OF METAMATERIALS FOR MULTIFUNCTIONAL SATELLITE BUS ENABLED VIA ADDITIVE MANUFACTURING

Michael A. Macchia, M.S.S.E, B.S.A.E
Captain, USAF

Committee Membership:

Maj Ryan O'Hara, PhD
Chair

Dr. Richard Cobb
Member

Dr. Anthony Palazotto
Member

Abstract

Space systems require materials with superior stiffness to weight ratios to provide structural integrity while minimizing mass. Additive manufacturing processes enable the design of metamaterials that exceed the performance of naturally occurring materials in addition to allowing the integration of non-structural functions. This research explored the use of a high stiffness, high density, small melt pool track width AM material, Inconel 718, to enable the production of metamaterials with finer features possible than can possibly be created using a lower density aluminum alloy material. Various metamaterials were designed utilizing thin wall triply periodic minimal surface infilled sandwich structures. The performance characteristics of these metamaterials were evaluated through modal analysis; demonstrating a 16-18% greater stiffness-to-weight ratio than 7075-T6 aluminium. These results were successfully applied to a multifunctional, lightweight, 3U CubeSat chassis design, fabricated from Inconel 718; resulting in a structurally mass efficient satellite bus. Additionally, modal analysis was conducted on the CubeSat chassis loaded with representative payload masses to evaluate the dynamic modal response of the final structure. Vibration testing was conducted in accordance with NASA General Environmental Verification Standard qualification standards, demonstrating the survivability of the chassis under launch conditions. It was shown this metamaterial based design approach could provide a lighter, stiffer chassis than manufactured from traditional aluminum alloy components.

Acknowledgments

This research would not have been possible without the assistance and support from the AFIT faculty, my friends, and my family. My advisor, Major Ryan O'Hara, thank you for your guidance both as Master's student and military officer. Ben Doane, Greg Cobb, Chris Sheffield and Travis Shelton, thank you for your lab support, without your assistance I wouldn't have anything to test or the means to evaluate it. Jamie Smith and Michael Ranft, thank you for your ensuring the lab equipment was functioning and the quick turnaround of the equipment that wasn't. To Philip Smith and Randall Sharp, thank you for design and hardware expertise. Brian Crabtree, Chris Harkless, Dean Harshman, and Dan Ryan, thank you for your hard work; overcoming unexpected obstacles to provide a finished chassis. My thesis committee, Dr. Palazotto, Dr. Cobb, and Major Kemnitz, thank you for spending countless hours reviewing my work, providing feedback, and treating me as one of your own students when I had questions. Finally, I would like to dedicate this thesis to my wife and daughter, whose love and support was critical through the long days and late nights spent on this research.

Michael A. Macchia

Table of Contents

Page

Page

List of Figures

List of Tables

Table Page

List of Symbols

ν	Poisson ratio
ω_n	natural frequency
ρ	density
A	area
f	frequency
I	moment of inertia
K	bending stiffness
K	number of criteria
K	stiffness
k_i	periodicity
L	length
L_i	absolute length of TPMS structure
l_t	lattice thickness
m	mass
n_i	number of unit cells
NV	normalized value
r_j	rank of criteria
t	total thickness
w_t	wall thickness
b	base
cc	cubic centimeter
d	TPMS unit cell size
E	modulus of Elasticity
g	gram
h	height
Hz	hertz
J	joule
kg	kilogram
lbf	pound force
mm	millimeter
N	Newton
Pa	Pascal
s	second
V	volt
W	watt

APPLICATION OF METAMATERIALS FOR MULTIFUNCTIONAL SATELLITE BUS ENABLED VIA ADDITIVE MANUFACTURING

I. INTRODUCTION

1.1 Background

Launching a satellite into space is an extremely expensive endeavor. However, the rise of secondary payloads has significantly decreased launch costs from tens or hundreds of millions of dollars to millions of dollars [1]. This trend has been driven by improvements in microelectronics, allowing for payloads and support systems to be packed into very small satellites. Additionally, the introduction of standardized launch containers, such as the Poly Picosatellite Orbital Deployer (PPOD) and the Planetary Systems Corporation (PSC) Canisterized Satellite Dispenser (CSD), provided a standardized platform to design these small satellites [2, 3]. These systems provide a cost effective means to launch multiple secondary payloads to any space mission, by causing any remaining mass and volume not occupied by the primary payload. Satellites launched from these systems are called "CubeSats", in reference to the standard payload size of a 10x10x10 cm cube, or 1U and total mass of 1.33 kg. CubeSats can be scaled up in 1U multiples to increase satellite performance, resulting in 3U, 6U, 12U and 27U satellites [4].

CubeSats began as a means for academic institutions to conduct relatively inexpensive experiments. However, as spacecraft technology has improved, space components and electronics have drastically decreased in size and mass. The size and mass reduction enabled CubeSats to conduct more sophisticated missions, As a re-

sult CubeSats have evolved into a common platform for commercial and government use. The affordable launch cost and low development cost enables high risk, high reward missions that would have previously been unacceptable [4]. Furthermore this has led to the rise of Distributed Satellite Systems (DSS), instead of launching one large satellite, a constellation of smaller satellites can be used to conduct the same mission [5]. Depending on mission requirements DSS can provide significant benefits over traditional single satellites systems. A few of these benefits, identified by Jilla are listed below [6]:

- **Decentralization of Resources:** A satellite payload can be distributed between multiple smaller satellites. This ensures that the entire mission is not compromised by the failure of a single satellite, improving the availability and survivability of the system.

- **Smaller, Simpler Satellites:** Integrating every instrument along with the necessary support equipment on a single platform requires large satellite buses and increases the overall complexity of the satellites. Developing and producing smaller, simpler satellites can provide cost and schedule benefits.

- **"Mass Production" of Satellites:** Multiple identical satellites may be required in a single constellation or used as a part of different constellations requiring the same functionality. This allows for benefits such as learning curve savings and reduced integration and testing to be leveraged due economies of scale.

- **Ramped Deployment and Upgrades:** DSS enables systems to be rolled out incrementally; a few satellites can be launched providing limited capability to meet immediate needs and then ramped up as required [7]. Additionally, when specific payloads become outdated, individual satellites can be replaced with

upgrades at much less cost than replacing a single large satellite.

During the time of this research, historic launches occurred reinforcing the importance of small satellites role in the future of spaceflight. Rocket Lab's Electron Launch Vehicle (LV) completed its first operational mission of six small satellites totalling just over 40 kg [8]; followed by a second launch for the National Aeronautics and Space Administration (NASA) Educational Launch of Nanosatellites (ELaNa) program. The ELaNa mission was comprised exclusively of CubeSats, the first time a launch has ever been dedicated to only CubeSats [9]. The Electron rocket was developed as a first commercial LV intended specifically to meet the growing small satellite market. Additionally, on December 3, 2018 a SpaceX Falcon 9 rocket carried 64 small satellites, 49 of which were CubeSats, making history as the largest ride-share mission in the United States [10].

Due to these trends, significant research and investment has been focused into CubeSat development, resulting in an increase in commercial hardware designed specifically for CubeSat form satellites. One area that is commonly neglected is the design and manufacturing of the CubeSat bus structure. The bus structure is the structural frame that holds the payload and support systems together and ensures the satellite remains intact under the dynamic loads imposed during launch. The mass taken up by the bus structure reduces the available mass for the payload. Therefore, similar to a modern aircraft, the design objective of the bus structure is to minimize mass while maintaining the structural requirements dictated by the launch vehicle. Achieving this objective requires developing new lightweight high strength structures. Traditional manufacturing methods provide limited means to achieve this goal. Karson Roberts, a previous master's student at Air Force Institute of Technology (AFIT), investigated using the expanded design envelope enabled by Additive Manufacturing (AM) to tackle this problem. Roberts' research specifically investigated the use of

a lattice sandwich structure instead of solid aluminum. His research demonstrated that the lattice structures provide increased stiffness at a reduced mass [11]. In the research herein, the use of Triply Periodic Minimal Surface (TPMS) structures to develop a metamaterial with superior material properties was investigated in lieu of lattices. TPMS structures have been found to have even greater stiffness-to-weight ratios than lattice structures, along with other advantages [12]. The benefits of TPMS structures will be discussed in detail in Chapter II.

1.2 Problem

Generating, modeling, and analyzing TPMS structures has been a very difficult process and until recently there has not been commercially available software capable of accomplishing these tasks [12]. nTopology's newly developed software uses implicit functions to quickly generate TPMS structures and provides a process to turn these implicits into 3-D meshes which can be analyzed using Finite Element Analysis (FEA) methods.

Modal analysis of these TPMS structures has not been extensively conducted and high-fidelity Finite Element Model (FEM)s do not currently exist. These lapses severely limit the design benefits that can be achieved by improving CubeSat bus structure designs.

1.3 Research Questions and Objectives

The overall objective of this research is to evaluate the benefits of TPMS structures in designing a metamaterial for space structure applications and compare a CubeSat bus structure utilizing TPMS structures and AM versus traditionally manufactured processes and design.

This research will strive to answer the following questions:

- Can a metamaterial with a greater stiffness-to-weight ratio than traditional materials used for space application be designed through the use of TPMS structures?
- Can a mass efficient CubeSat 3U bus structure be designed through the application of metamaterials?
- Is it possible to generate an accurate FEM of TPMS based structures?
- Can components be integrated into the satellite structure demonstrating the the use of AM processes to enable multi-functional structures?

1.4 Justification

Identifying a metamaterial that provides superior lightweight structures than traditional solid alloys and the capability to model and analyze these structures through FEA will provide a means to push the design boundaries of satellite buses. The capability to model these superior structures will enhance the ability for spacecraft manufacturers to rapidly develop and qualify new designs. Reducing the time and cost to develop and manufacture satellite buses will greatly reduce the space system's overall development time. The use of AM and the ability to analyze the design through FEA also enables iterative design improvements, allowing the satellite bus to be improved and modified throughout production. Additionally, AM opens the door to future improvements such as multi-functional structures. For example, through AM, the pressure tank for a cold gas or mono-propellant could be designed into the structure of the bus or plumbing could be designed into the exterior walls of the satellite to create a heat exchanger [13]. Finally, using AM can provide a cost effective means to fabricate bus structures as monolithic structures, reducing the number of fasteners required to assemble the structure and further increasing its overall stiffness [14].

1.5 Scope

The research was limited to a 3U CubeSat designed for the PPOD standardized launch container. The CubeSat bus structure was evaluated against the design of an aluminum chassis from previous research at AFIT. The aluminum chassis incorporated a lattice sandwich structure utilizing additive manufacturing. The performance measurements of the two bus structures were limited to the first fundamental frequency and total mass, validated through laser vibrometry and vibrational testing.

1.6 Assumptions

It is known that AM results in anisotropy based off build direction [15]. However, the effects of anisotropy will have a minimal influence on the modal analysis relative to the design factors and geometry of the structure. This assertion is supported by tensile testing of Inconel 718 bars conducted at AFIT. Test results demonstrated the negligible differences of modulus of elasticity for varying build directions. Therefore, the material properties of the FEM, were assumed to be isotropic for simplification.

1.7 Approach

The research was divided into four phases, bus structure topology design, material selection, metamaterial design and selection, and finally experimental modal analysis of the final design.

The first phase explored various topology designs of the overall bus structure focusing on meeting the PPOD and CubeSat specifications and maximizing the stiffness-to-mass of a solid body's design. Phase II consisted of a material trade study to determine the optimal metal powder for AM of thin wall fine featured structures. The third phase involved designing and comparing equivalent sized beams with var-

ious TPMS structures (gyroid, scwarz-P, diamond, lidinoid) when measured using laser vibrometery to determine the metamaterial that provides the greatest stiffness to mass ratio. The final phase consists of an experimental modal analysis conducted through laser vibrometry and vibrational qualification testing to evaluate the final design and compare the results to the previous aluminum lattices based bus structure.

1.8 Materials/Equipment/Support

A variety of software packages were leveraged to successfully design the complex structures in this research. The primary software utilized in this research was nTopology's novel Platform. The capability to incorporate TPMS structures in the model was critical to enabling the design and fabrication of the metamaterials explored in this research. Every metal part printed in this research was modeled and sliced in Turbo then exported to the printer as a Common Layer Interface (CLI) file. SolidWorks was used to generate the model and drawings that were used for post processing; providing essential features such as hole locations, tolerances, and surface finishes. Finally, all FEM simulations were conducted in Abaqus CAE [16].

This research was conducted with two Laser Powder Bed Fusion (LPBF) metal printers , the Concept Laser MLab cusing 200R and M2 cusing. The specifications for each printer are shown in Table 1.1. Due to the limited build size the MLab cusing 200R was used for early test builds to verify the feasibility of complex geometries before printing full scale specimens. Full scale specimens for the metamaterial design study and final chassis build were conducted in the larger M2 cusing. Laser parameters and print settings varied for each build and will be specified in the methodology sections for each test setup.

Modal analysis was conducted with the Polytec PSV-400 Scanning Vibrometer

Table 1.1. Concept Laser AM Printer Specifications [17, 18]

Parameter	MLab cusing 200R	M2 cusing
Build Envelope (X x Y x Z)	100 x 100 x 100 mm^3	250 x 250 x 250 mm^3
Layer Thickness	15-30 µm	20-80 um
Laser System	Fibre Laser 200 W	Fibre Laser 400 W
Scan Speed	7 m/s	7 m/s
Focus Diameter	75 µm	50 - 500 µm

(Figure 1.1). The PSV-400 provided the ability to rapidly measure and analysis structural vibrations within a 2D plane; enabling the identification natural frequencies and visualization of their corresponding mode shapes [19]. The PSV-400 collects velocity and displacement through its laser Doppler vibrometer by sensing the frequency shift of back scattered light from a moving surface [19]. This system provided significant advantages over traditional accelerometers. Accelerometers add additional mass to a system, while the wires can alter the system's boundary conditions; adversely affecting the accuracy of modal analysis. Additionally, an accelerometer must be mounted at each location a data point is desired; the PSV-400 incorporates two scanning mirrors allowing it rapidly scan a large number of data points within a 2D plane with ease.

NASA's General Environmental Verification Standard (GEVS) qualification testing was conducted on a MB Dynamics Electro-Dynamic Shaker System C40HP vibration table. This system provided the ability to test the final CubeSat chassis at levels required by GEVS in all 3 axis orientations. Ultra-lightweight accelerometers were used to monitor the process and measure the combined chassis-PPOD system Power Spectral Density (PSD) before and after vibration for each axis.

Figure 1.1. Polytec PSV-400 Scanning Vibrometer

1.9 Overview

This research was conducted through multiple studies in an iterative process. The results of each study drove the decisions and methodology of the succeeding study. Therefore, instead of a chapter covering the methodology followed by a chapter discussing the results, chapters will be divided into specific studies. Each of these chapters will cover both the methodology and results associated with the research conducted for the study. The final chapter will provide a comprehensive summary and conclusions for the research conducted.

- Chapter I: Introduction - States the objective of this thesis, establishes the motivation, and briefly discusses the background and methodology of the research.
- Chapter II: Background - Provides context and discusses theory presented in relative literature related to CubeSats, Space Launch, AM, FEA, and TPMS structures.

- Chapter III: Topology Study - Discusses the methodology and results of the topology study conducted to determine the topology of the CubeSat bus structure.
- Chapter IV: Material Selection Trade Study - Discusses the methodology and results of the trade study conducted to determine the preferred AM material.
- Chapter V: TPMS Metamaterial Design Study - Discusses the methodology and results the study conducted to maximize the performance characteristics of the metamaterial used for the CubeSat bus structure design.
- Chapter VI: CubeSat bus structure Study - Discusses the methodology and results of the CubeSat bus structure design and the tests conducted to evaluate its structural characteristics.
- Chapter VII: Conclusions and Recommendations - Summarizes the results, draws conclusions, and discusses recommendations for future research.

II. BACKGROUND

2.1 Chapter Overview

This chapter will provide background on the various topics covered by this research based off currently available technical literature. A brief discussion of CubeSats and the space launch environment will be covered to provide context of the requirements, common components that make up a functional CubeSat, and the conditions a CubeSat must survive to reach orbit. Additionally, this chapter will discuss the Additive Manufacturing (AM) process used in this research as well as the benefits of the Triply Periodic Minimal Surface (TPMS) structures enabled by AM. Finally, Finite Element Analysis (FEA) will be discussed to better understand how it will be used for design and qualification.

2.2 CubeSat

The original CubeSat design was the outcome of a collaborative effort between California Polytechnic (Cal Poly) State University, San Luis Obispo and Stanford University's Space Systems Development Laboratory (SSDL). The objective of the CubeSat was to "reduce cost and development time, increase accessibility to space, and sustain frequent launches" [20]. The initial design consisted of a 10 cm cube limited to a mass of 1.33 kg, currently referred as a 1U CubeSat [20]. The 1U has evolved into a standard unit size for larger CubeSats. As the CubeSat design became more popular, the size has expanded to as large as 27Us [20]. This standard unit volume ensures components and payloads are designed to fit in any other CubeSat, encouraging modular designs.

The primary payload of a CubeSat can vary greatly depending on the purpose of its mission. However, there are a few common subsystems that are required for basic

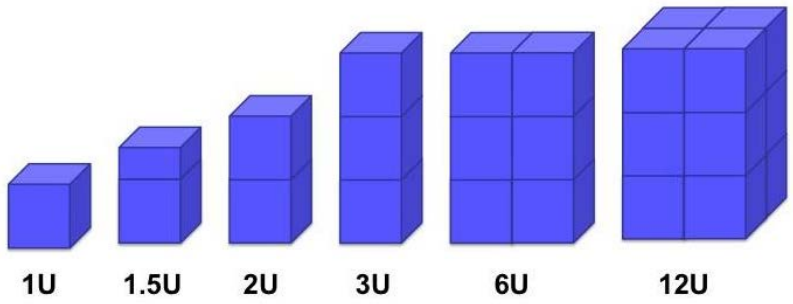

Figure 2.1. Examples of common CubeSat sizes [21]

functionality of a CubeSat. These subsystems are necessary for daily operations providing support functions such as attitude control, ground communication, and power management. A list of these subsystems can be found in Table 2.1 along with a short description of their function.

Table 2.1. List of Common Spacecraft Subsystems [22]

Subsystem Name	Function
Propulsion	Spacecraft thrust , including fuel storage and plumbing
Attitude Determination and Control System (ADCS)	Sensors, actuators, and software necessary to control spacecraft pointing
Command and Data Handling (CD&H)	Electronics and software used to receive and distribute commands and to store and forward payload data and spacecraft telemetry
Telemetry, Tracking, and Command (TT&C)	Radio and associated hardware, such as cabling and antennas, used to communicate with the ground and other spacecraft
Power	Electronics, power generation, and power storage devices, as well as harnessing for power distribution

The common need for these subsystems has led to availability of affordable Commercial Off-The-Shelf (COTS) components designed specifically to fit within the 1U envelope. These COTS components vary in performance enabling a satellite developer to choose an option that fits their specific need without designing hardware unique to their satellite. The modularity of the CubeSat design is critical to the original objectives of reducing spacecraft cost and development time.

The two most common launch platforms used to deploy CubeSats as a secondary payload are Cal Poly's Poly Picosatellite Orbital Deployer (PPOD) and the Planetary Systems Corporation (PSC) Canisterized Satellite Dispenser (CSD).

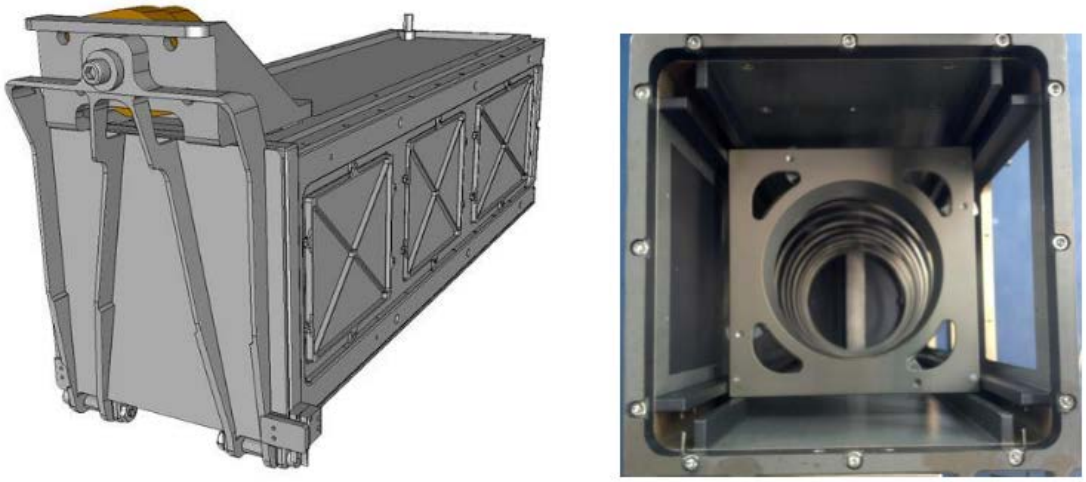

Figure 2.2. PPOD and cross section (3U) [20]

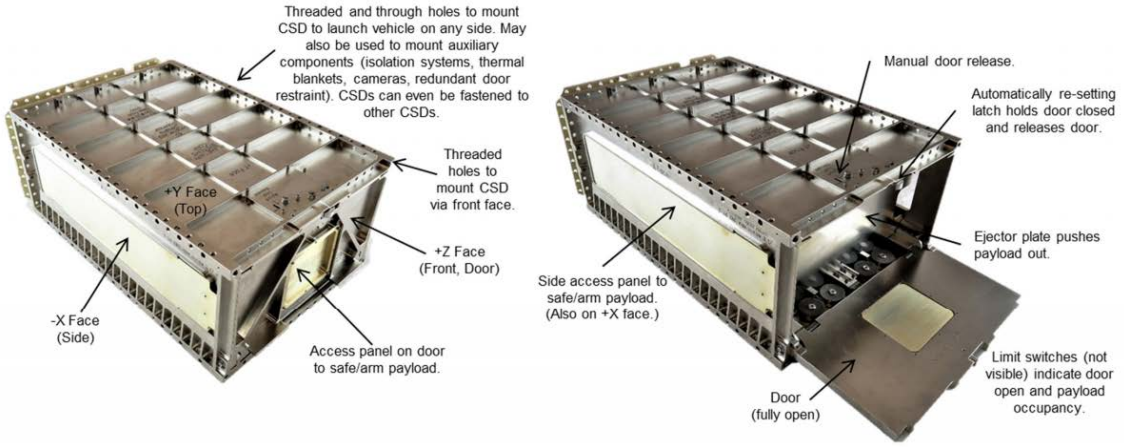

Figure 2.3. CSD and features (6U) [23]

Both systems follow the basic design of a contained structure with a spring loaded ejector plate. The CubeSat is loaded into the deployer and door is latched preventing the CubeSat from prematurely ejecting. During the deployment phase, this door will be released allowing the CubeSat to be pushed out into space by the compressed spring. The main difference in the CSD and PPOD designs lie in how the CubeSat is

contained within the deployer. The PPOD uses a rail system, requiring the CubeSat structure to meet specific tolerances to ensure it slides correctly into the PPOD [21]. The CSD on the other hand uses a clamping system. The CubeSat chassis must be designed with a tab along the edges of the bottom corner; when the CSD door closes a lever is actuated, clamping down on the tabs locking the CubeSat in place [24].

2.3 Spacecraft Launch

Before a spacecraft can become operational it must first make the journey to its mission orbit. During the launch process the spacecraft undergoes extreme accelerations and vibrations; surviving the launch without any damage to payload or support equipment is essential to mission success. Independent of the survivability of the spacecraft there is also an inherent risk of failure from the launch vehicle as well. Despite the fact that currently available launch vehicles have provided a relatively high success rate, there is no guarantee that a failure will not occur [22]. To reduce the risk of failure, stringent qualification testing of the secondary payloads is required by launch providers to ensure the additional payload will not adversely impact the launch. The primary purpose of the spacecraft chassis is to provide structural support to ensure mechanical failure does not occur during launch. This sections will cover the general qualification testing a CubeSat undergoes and some of the common failures modes.

2.3.1 Launch Environment

The primary forces a spacecraft experiences during launch are vibration and shock. Shocks are large excitations that occur in a short time span and quickly die off. Shock occurs during specific events such as ignition, engine shut-off, and payload separation. This research will focus on vibrational forces. Vibrational forces are prevalent

throughout launch for sustained periods and provide greater overall excitation energy than shock forces. These vibrational loads are generally caused by the Launch Vehicle (LV)'s propulsion system, control system, and via acoustic mechanisms. Additionally, it should be noted that shock loads are incorporated in the random vibrational loads that are conducted in vibrational testing [25]. In addition to surviving these significant vibrational forces, it also important that coupled modes of the launch vehicle and its payload are accounted for. The fundamental resonance frequency of launch vehicles are generally below 35 Hz [22], it is highly recommended that spacecraft are designed with a first fundamental frequency above this value. If the first fundamental frequency is lower, additional analysis is generally required to ensure the coupled loads do not adversely affect the guidance, navigation, and control systems or exceed stress margins [26, 25].

Every launch vehicle exhibits its own unique loading and vibrations during launch. As a result, each launch provider has its own specific requirements that a spacecraft must meet. In the ride-share environment, knowing the exact launch vehicle during development is not always guaranteed. Fortunately, the National Aeronautics and Space Administration (NASA) established the General Environmental Verification Standard (GEVS) providing general requirements encompassing the worst case load conditions of common launch vehicles [26].

Figure 2.4 provides an example of how GEVS accounts for the worst case scenario. The acceleration magnitude at the corresponding frequency is plotted for each LV. The vibration profile dictated by GEVS exceeds the profile of the other four launch vehicles shown, providing a conservative estimation of vibrational loads that must be accounted for. Designing to GEVS will ensure that a spacecraft will meet the specific requirements of a variety of launch vehicles. This design strategy is essential for spacecraft utilizing ride-shares; increasing the probability the spacecraft can launch

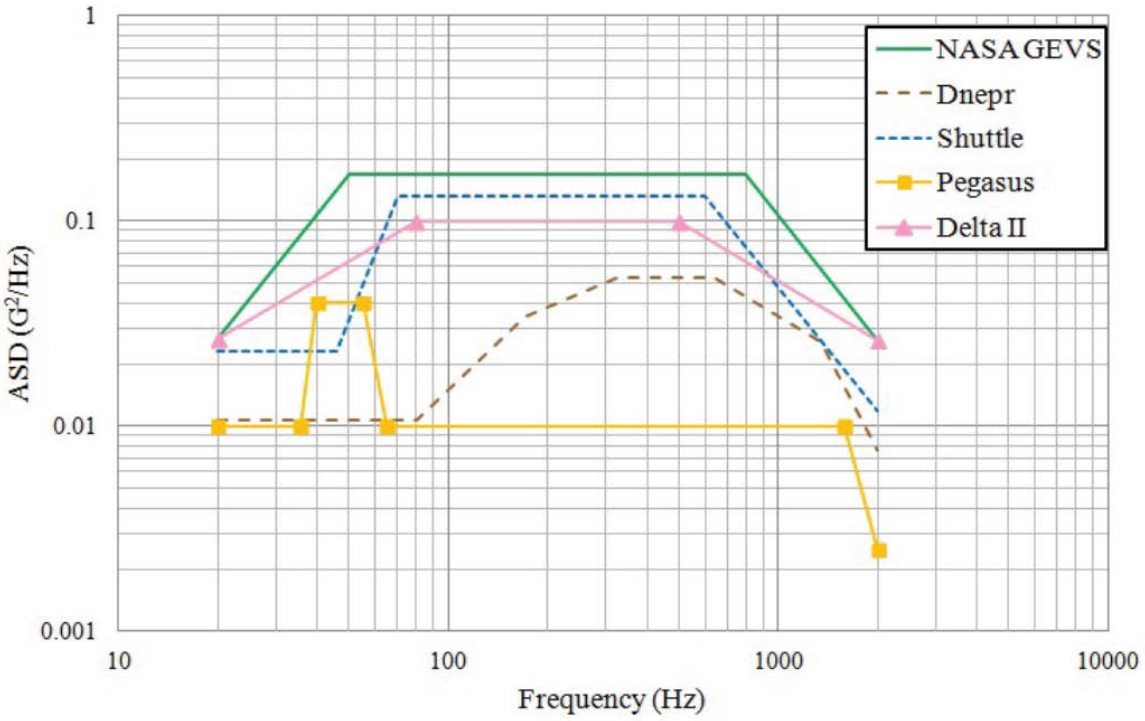

Figure 2.4. Vibration profile NASA GEVS profile which meets or exceeds the vibrational profile of every launch system [25]

on the first available platform.

2.3.2 Spacecraft Qualification

GEVS encompasses a range of environmental requirements a spacecraft must meet, including structural and mechanical verification, electromagnetic compatibility, thermal, and contamination control. Vibration testing requires the satellite to undergo sine sweep and random vibration loading in all three axes to verify the satellite can withstand the forces it will experience during launch [26]. The sine sweep provides a means to quantitatively evaluate the satellite after the random vibration load. Prior to conducting the random vibration profile, a sine sweep is conducted between 20-2000 Hz to provide a baseline of the satellite modes. A second sine sweep is conducted after the random vibration profile is executed to evaluate whether any of the peaks of the

modes shifted. These shifts indicate there was a change in stiffness within the satellite indicating a structural or mechanical failure. Two common failure modes that can cause this shift are fastener rotation (reducing applied torque and corresponding load) and payload support failure [27]. If the frequency shift is not significant the structure may have "loosened" due to the fasteners backing out, reducing the overall stiffness. Larger shifts are commonly caused from payload supports or fasteners shearing. The sine sweep is also the primary means of identifying the frequency of the first mode (fundamental frequency) of the satellite. As mentioned previously it is essential to design the satellite with a first fundamental frequency greater than 35 Hz, however GEVS exceeds this value, recommending coupled loads analyses between satellite and booster for modes below 70 Hz [26]. In this research the more conservative value of 70 Hz will be the assumed threshold for the first fundamental frequency, a typical requirement for secondary payloads.

$$\omega_n \propto \sqrt{\frac{k}{m}} \tag{2.1}$$

The natural frequency of a system is proportional to its mass and stiffness as denoted by Eq 2.1 [28]. Therefore, two options are available to increase the natural frequency, increase the stiffness or decrease the mass. To maximize the outcome, the satellite's chassis should be designed to maximize its stiffness to mass ratio. This can be achieved through the physical design of the chassis as well as through the use of materials with a high stiffness-to-weight.

The GEVS random vibration profile for a 3U CubeSat (less than 22.7 kg) can be found in Table 2.2 and Figure 2.5. The more conservative (higher level) qualification profile will be used for this research.

Table 2.2. Generalized Random Vibration Test Levels (22.7 kg or less) [26]

Frequency (Hz)	ASD Level (g^2/Hz)	
	Qualification	Acceptance
20 20-50 50-800 800-2000 2000	0.026 +6 dB/oct 0.16 -6 dB/oct 0.026	0.013 +6 dB/oct 0.08 -6 dB/oct 0.013
Overall	14.1 G_{rms}	10.0 G_{rms}

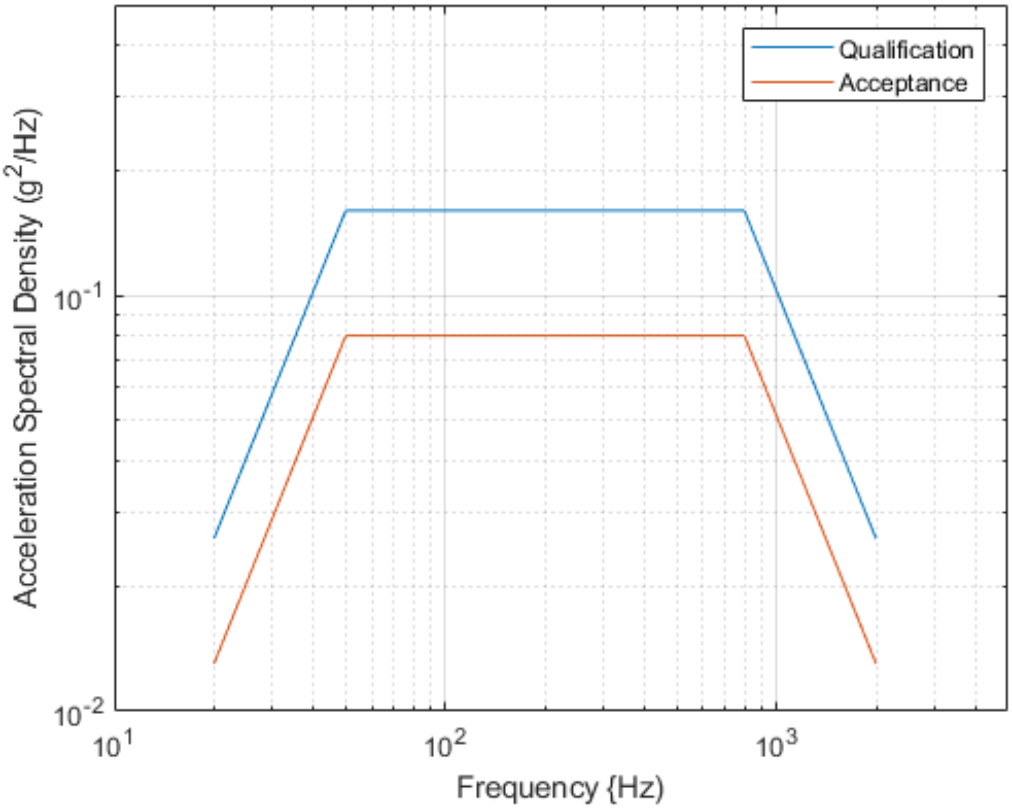

Figure 2.5. Generalized Random Vibration Test Levels [26]

2.4 Additive Manufacturing

The origins of metal AM trace back to the first polymer Selective Laser Sintering (SLS) printer developed at the University of Texas at Austin's Mechanical Engineering Department in 1986 [29]. The first prototype, 'Betsy', proved the feasibility of AM producing crude shapes such as the one shown in Figure 2.6 [29]. The capabilities

Figure 2.6. Initial parts printed by Betsy [29]

of AM has made great leaps over the last three decades, but still has many more obstacles to overcome. Figure 2.7 provides a timeline of significant events that have furthered the progress of AM.

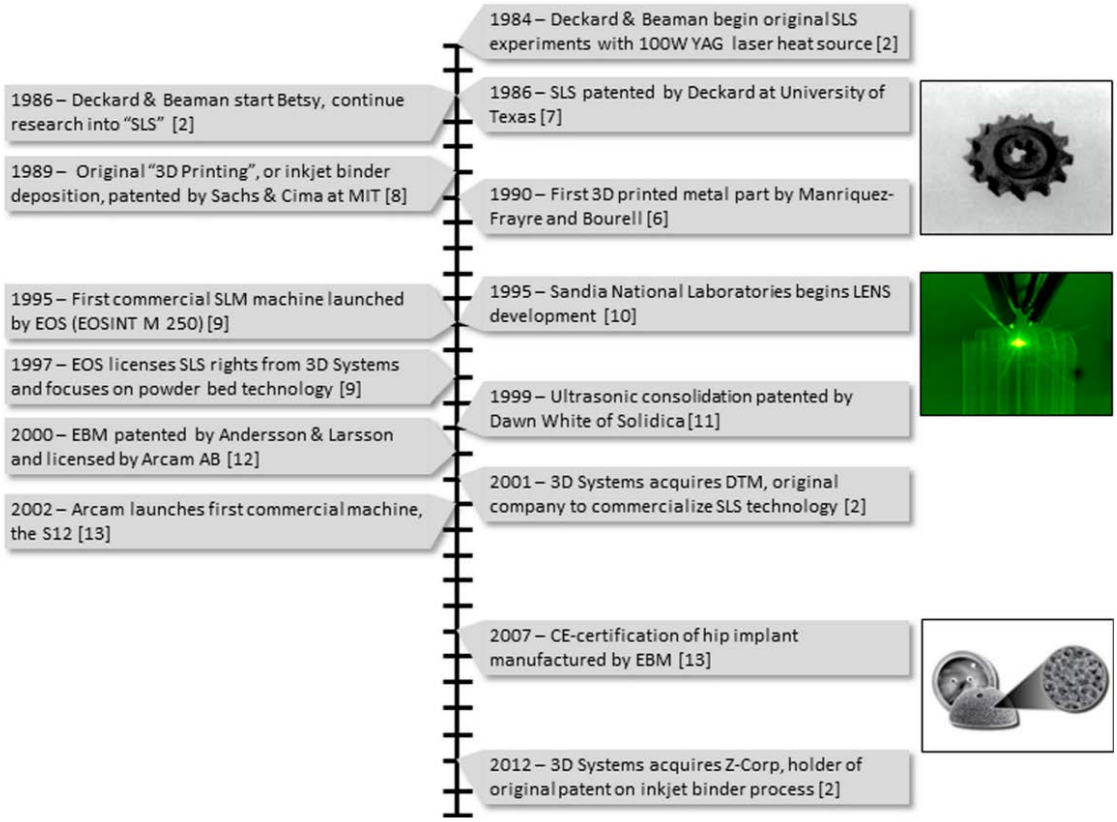

Figure 2.7. Timeline of significant events in AM development [15, 30, 31, 32]

There are many AM processes currently in use today. Table 2.3 provides an

overview of the various AM categories. This research will focus on Laser Powder Bed Fusion (LPBF) due to its strengths and the availability of equipment at the Air Force Institute of Technology (AFIT). The characteristics of LPBF and manufacturing approach of Design for Additive Manufacturing (DfAM) will be covered in greater detail in this section.

Table 2.3. Classification of AM processes [33, 34]

CATEGORIES	TECHNOLOGIES	PRINTED "INK"	POWER SOURCE	STRENGTHS / DOWNSIDES
Material Extrusion	Fused Deposition Modeling (FDM)	Thermoplastics, Ceramic slurries, Metal pastes	Thermal Energy	• Inexpensive extrusion machine • Multi-material printing • Limited part resolution • Poor surface finish
	Contour Crafting			
Powder Bed Fusion	Selective Laser Sintering (SLS)	Polyamides /Polymer	High-powered Laser Beam	• High Accuracy and Details • Fully dense parts • High specific strength & stiffness • Powder handling & recycling • Support and anchor structure • Fully dense parts • High specific strength and stiffness
	Direct Metal Laser Sintering (DMLS)	Atomized metal powder (17-4 PH stainless steel, cobalt chromium, titanium Ti6Al-4V), ceramic powder		
	Selective Laser Melting (SLM)			
	Electron Beam Melting (EBM)		Electron Beam	
Vat Photopolymerization	Stereolithography (SLA)	Photopolymer, Ceramics (alumina, zirconia, PZT)	Ultraviolet Laser	• High building speed • Good part resolution • Overcuring, scanned line shape • High cost for supplies and materials
Material Jetting	Polyjet / Inkjet Printing	Photopolymer, Wax	Thermal Energy / Photocuring	• Multi-material printing • High surface finish • Low-strength material
Binder Jetting	Indirect Inkjet Printing (Binder 3DP)	Polymer Powder (Plaster, Resin), Ceramic powder, Metal powder	Thermal Energy	• Full-color objects printing • Require infiltration during post-processing • Wide material selection • High porosites on finished parts
Sheet Lamination	Laminated Object Manufacturing (LOM)	Plastic Film, Metallic Sheet, Ceramic Tape	Laser Beam	• High surface finish • Low material, machine, process cost • Decubing issues
Directed Energy Deposition	Laser Engineered Net Shaping (LENS) Electronic Beam Welding (EBW)	Molten metal powder	Laser Beam	• Repair of damaged / worn parts • Functionally graded material printing • Require post-processing machine

2.4.1 Laser Powder Bed Fusion

LPBF is an AM process that utilizes a focused laser to melt powder particles layer by layer [35, 15]. Figure 2.8 provides a basic schematic of a LPBF and its components. The LPBF process begins with the recoater blade dragging metal powder over

the initial substrate, commonly referred to as the 'build plate' [15]. The first layer of powder is melted to the build plate by the laser. The scanning mirror and focal lens are used to steer and focus the laser to the desired locations. After the desired path has been melted, a new layer of powder is spread across the build chamber and an additional layer of the part is melted [36]. This process continues until the full part has been printed. Unlike laser sintering processes, the previous layers are re-melted during the current layer in LPBF, allowing for adherence to the current layer and the remainder of the part [15]. Figure 2.9 illustrates the interaction between the laser beam, powder layer, and previous layers. The build plate serves two purposes during the build process; mechanical and thermal support [15]. The build plate is bolted or clamped down to ensure that existing layers do not move during the printing process [15]. The build plate also provides thermal support allowing a thermal path to dissipate the large quantity of heat output by the laser [15]. Heat dissipation is extremely important to build quality; as it greatly affects the ability to print overhanging parts and affects the residual stresses in the part [37]. At the end of the LPBF printing process the part must be removed from the build plate; this is commonly done using abrasive saws or wire electrical discharge machining (EDM) [15, 38].

2.4.2 Additive Manufacturing Process Parameters

The use of AM parts is predicated on the ability to produce quality parts without voids or defects. Many factors and parameters affect build quality, ranging from the powder used, printing parameters, and post-processing. The density of AM parts are crucial to their mechanical properties; achieving densities approaching 100% is the primary objective of optimizing AM process parameters [41]. Countless studies have been conducted on determining the optimal parameters for various powder alloys. The most common parameters investigated are laser power, scan speed (velocity of

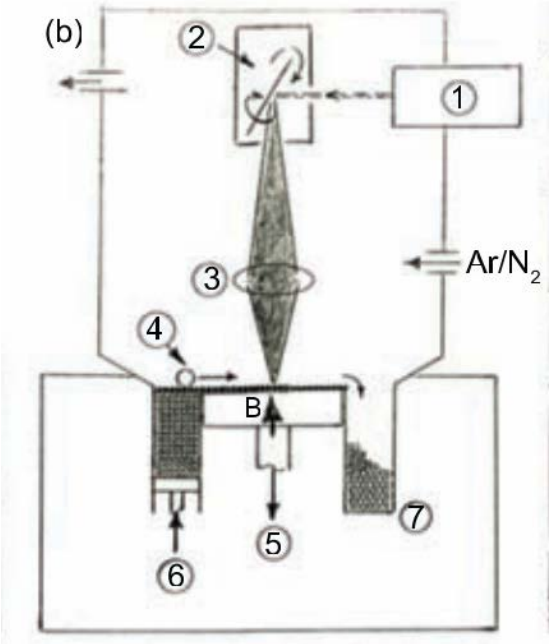

ID	Component
1	Laser
2	Scanning Mirror
3	Focus Lens
4	Recoater Blade
5	Build Piston
6	Powder Dispenser Piston
7	Overflow Chamber
B	Build Platform

Figure 2.8. LPBF system schematics [35, 15, 39]

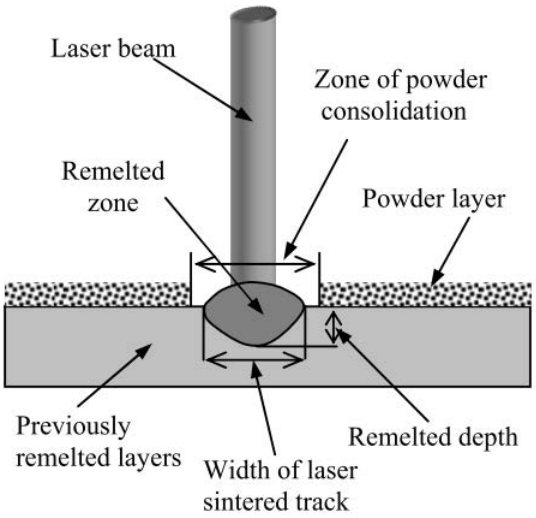

Figure 2.9. Typical cross-section of a laser melted track from metal powder [40]

laser along melt track), hatch spacing (distance between parallel melt tracks), spot size (diameter of focused laser), and layer thickness (thickness of each powder layer), and scan strategy (the path of the laser throughout the print layer) [41]. The research herein will focus on the effects these parameters have on build quality based off of part density.

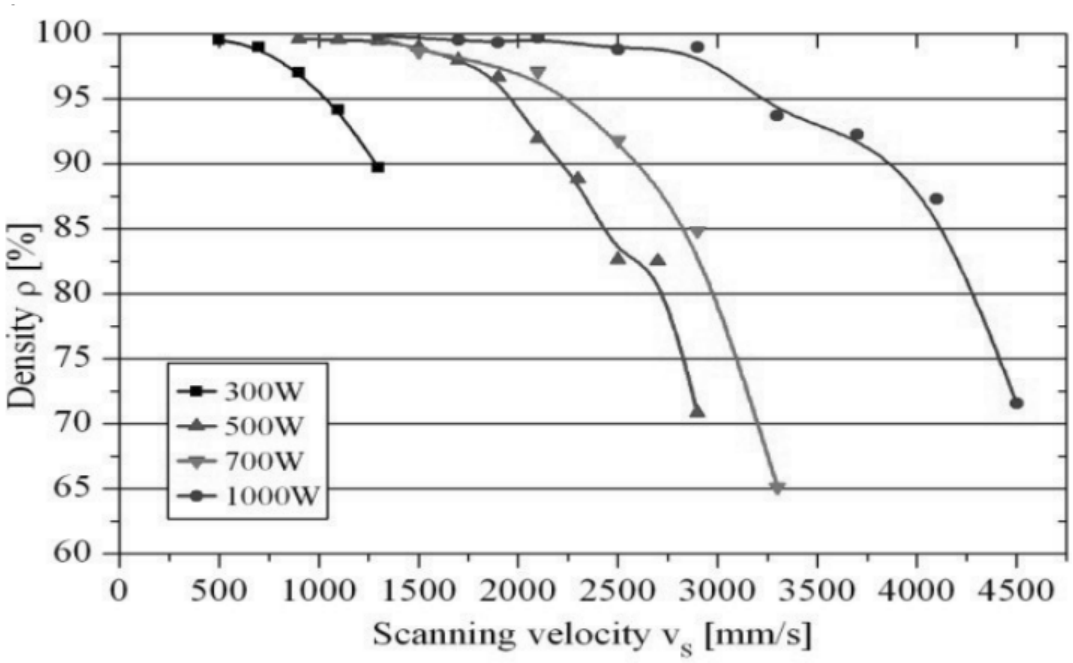

Figure 2.10. Density versus scanning velocity and laser power [41]

Increasing the scan speed while maintaining other parameters constant reduces the total energy transferred to the powder, resulting in lower part densities [41]. Figure 2.10 shows the effect of varying the scan speed and laser power on the part density. Increasing the laser power and scanning speed simultaneously allows high density parts to be manufactured at a faster build rate [41].

Figure 2.11 demonstrates the effect of increasing the hatch spacing while maintaining other parameters constant. Similar to the scan speed, the density decreases as hatch spacing increases. The effects of increasing hatch spacing is accelerated when exceeding the spot size as there is no longer overlap of melt tracks resulting

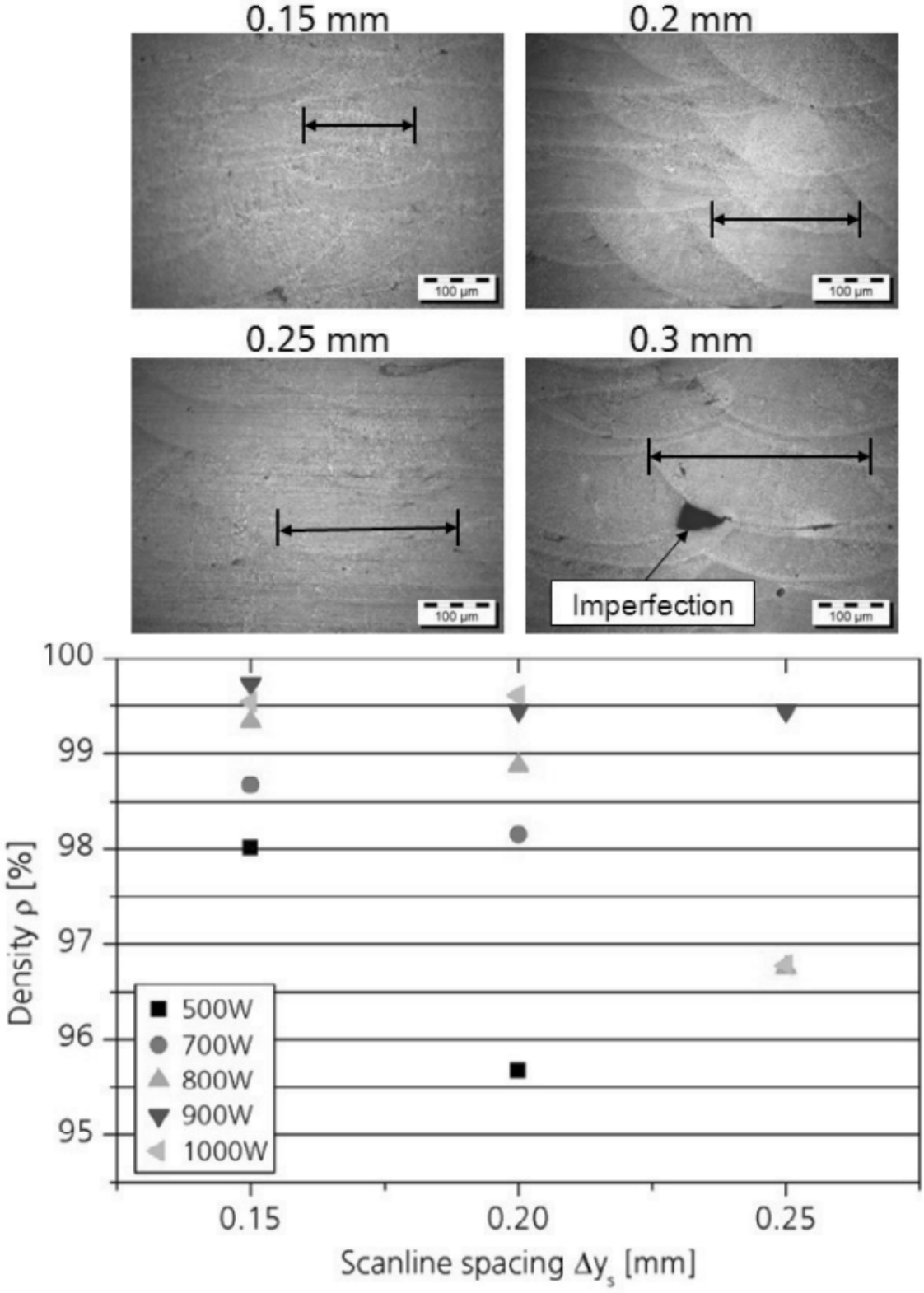

Figure 2.11. Density depending on the hatch spacing (spot size 0.2 mm) [41]

in imperfections between tracks as annotated in Figure 2.11 [41, 42]. Generally, it is recommended that 60-80% overlap is maintained to avoid this issue; increasing the probability of producing high density parts.

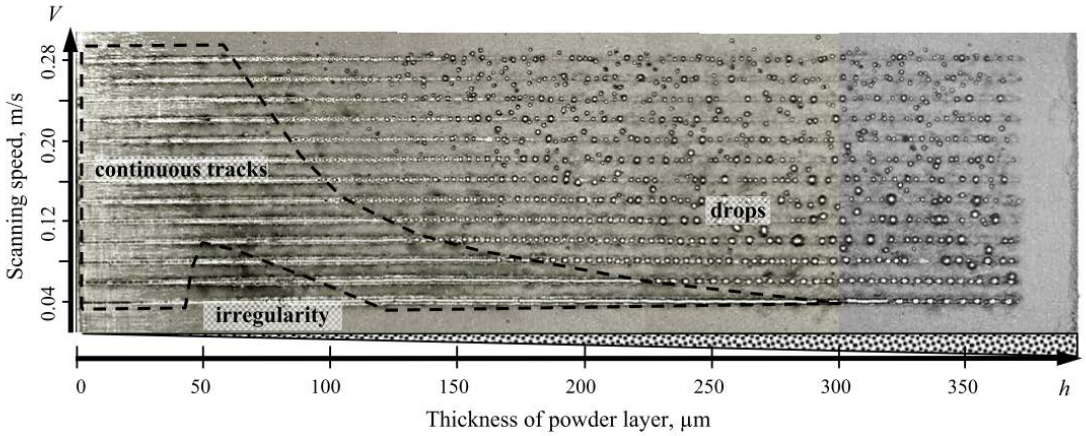

Figure 2.12. Top view of laser melted tracks at various scan speeds and layer thicknesses [40]

As the layer thickness increases, the amount of powder that must be melted and adhered increases. To maintain continuous tracks, the total input energy must also increase to match this thickness change. Figure 2.12 demonstrates the effect of increasing layer thickness at various scan speeds. As expected, there are no longer continuous tracks as the thickness and scan speed increase.

The last print parameter discussed is scan strategy. A study conducted at the University of Leuven, on fine-structure aluminum products, investigated how varying the scan parameters affected the relative density and micro-structure of additively manufactured parts. A summary of the density results are shown in Figure 2.13. The study demonstrated that the micro-structure can be tailored depending on scan strategy and that conducting two scan paths over each layer provides the greatest density [43]. It is important to note that conducting two passes for each track also doubles the time required to produce an AM part.

Sample	A	B	C	D	E
Scanning parameters					
Laser power (W)	200	200	200	200	200
Scanning speed (mm s^{-1})	1400	1400	1400	1400	1400
Hatch spacing (μm)	105	105	105	105	105
Scanning vector bidirectional (Bi) or unidirectional (Uni)	Bi	Uni	Bi	Bi	Bi
Rotation between layers	0°	0°	90°[a]	90°	90°
Islands 5 × 5 mm^2	No	No	No	Yes	Yes
Shift 1 mm	No	No	No	No	Yes
Relative Archimedes density (%) ($\rho_{theor} = 2.68$ g cm^{-3})	99.0	98.9	99.4	98.2	98.7
Texture index (according to Eq. (1))	1.974	1.982	1.266	1.127	1.079

[a] Rotating the long vector strategy 90° is not possible with the current Concept Laser© software. To get an idea of creating melt tracks rotated 90° to the previous scan direction, every layer was scanned twice with the second scanned tracks rotated over 90° to the first scanned ones.

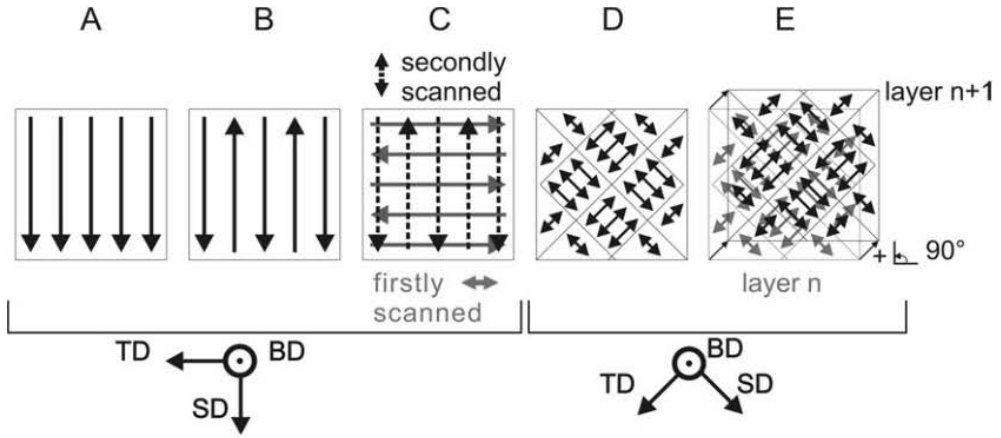

Figure 2.13. Overview of scanning strategy and scanning parameters and their relative density [43]

2.4.3 Design for Additive Manufacturing

AM has transformed what parts should look like and how they should be designed. AM enables significantly greater design flexibility than traditional subtractive methods; however, AM is still not without its own limitations. Layer by layer fabrication enables the production of nearly any complex shape [33]. Subtractive processes are constrained by the need for fixtures, specialized tooling, and the inability to access internal volumes [33]. This section will focus on DfAM specifically for the LPBF AM process to be used in the research herein.

2.4.3.1 Design Limitations

Before discussing the advantages and design freedom AM enables, it is important to discuss its current limitations and shortcomings. A common misconception of AM is there are no geometric limitations. Although the geometries enabled through AM are much greater than subtractive methods, they are still not without constraints.

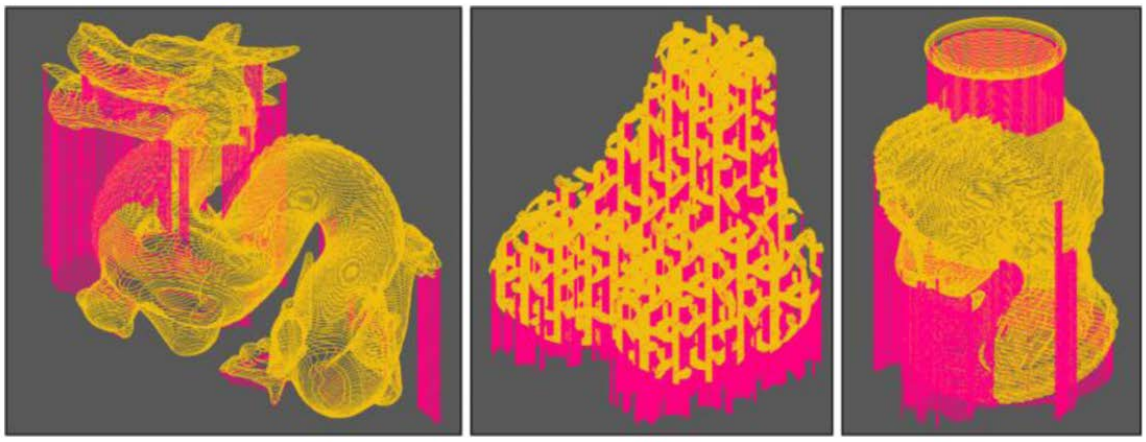

Figure 2.14. Example of support structures [33]

Support Structure. One of the greatest limitations is the need for support structure due to large thermal gradients and large overhangs. An overhang is any part of the structure that spans a horizontal distance without supporting structure below

it. Examples of these structures are shown in Figure 2.14 [44]. Support structures may be necessary to avoid part warping due to the large internal stresses from the high thermal gradients introduced by the LPBF process [44]. Parts with horizontal spans are limited in the distance that can be self-supported without additional support structures. The length that can be self-supported is highly dependent on the angle in relation to the horizontal build plane [44]. An AM topology optimization study conducted by the Wolfson School of Mechanical and Manufacturing Engineering has shown that overhangs with an angle of 45 degrees or more can support any length of overhang [45]. Removal of support structure requires additional post processing and depending on the location may not be feasible. Therefore, it is common to limit designs to overhang angles of 45 degrees or less [44].

Encapsulated Powder. An additional limitation is the inability to print fully enclosed hollow structures. Due to the process of LPBF there must be a way to remove encapsulated powder from internal geometries [44]. If not considered in the design process the powder will remain trapped within the structure reducing functionality and adding unnecessary mass. Powder removal can be done through access ports, however, this imposes difficulties ensuring the internal volumes are fully clean and free of metal particles. Depending on the function of the structure, residual metal powder may pose serious concerns. Residual powder causing short circuits within electronics is a significant concern in space system applications.

Dimensional Accuracy. The dimensional accuracy of a part evaluates how well the printed part compares to the original Computer Aided Design (CAD) model [33]. Currently, AM processes are significantly behind subtractive methods in this area. AM machines have the capability to build parts with tolerances within a several hundredths of centimeters [33]. Meanwhile, equipment employing traditional machining methods are capable of tolerances within a few thousandths of a millimeter [46]. Ad-

ditionally, the surface finish of a print part may varying significantly depending on the build direction. For parts that require tight tolerances and smooth surface finishes, significant post processing via traditional manufacturing methods are required. This requires those areas to be accessible to traditional tools limiting the location of high tolerance geometries.

2.4.3.2 Design Advantages

Considering the limitations of AM, the design freedom is still significantly greater than that of traditional manufacturing methods. AM enables additional benefits as well. In order to maximize the potential of DfAM, design engineers need to rethink how a part should be designed and interact with the rest of the system [44]. This would require designers to eliminate preconceived notions of what a part should look like based off more traditional manufacturing methods [44].

Shape Complexity. With AM, there is no additional cost to manufacture highly complex shapes. While in traditional manufacturing, methods such as injection molding the cost to produce highly complex geometries is proportional to the complexity of the mold required [33]. This cost makes complex parts prohibitively expensive, especially in low production environments such as the spacecraft industry [47]. The reduced cost of complexity enables the use of lattice and TPMS structures, which provide high strength-to-weight ratios, good energy absorption, good thermal, and acoustic insulation characteristics [48].

Internal Structures. One of the most significant characteristics of AM is the ability to include internal structures. The ability to include internal structures drastically increases the available design space. Internal structures enable designers to remove unnecessary mass from structures and tailor the design specifically to the parts functionality [44]. Additionally, AM allows for lattice and TPMS structures

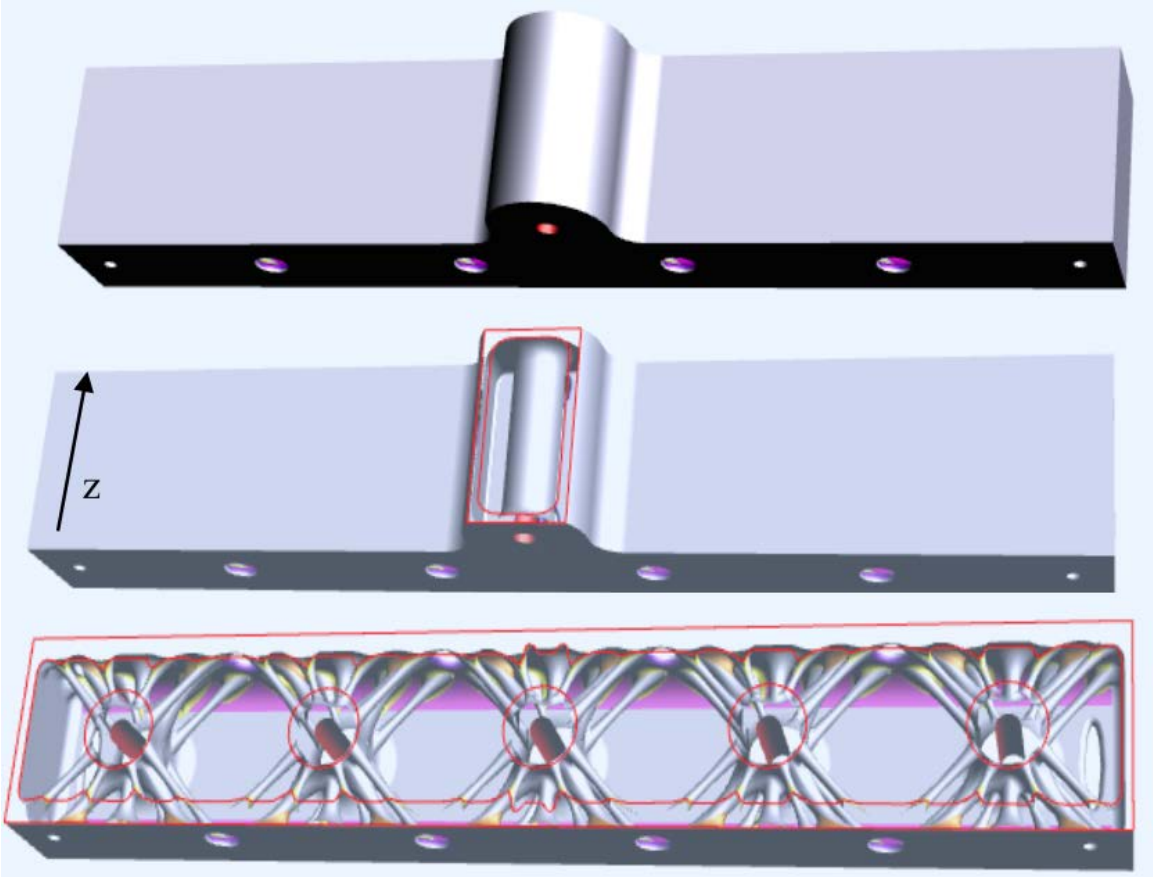

Figure 2.15. Example of internal structures enabled through AM [44]

to be integrated into shell structures to reduce overall mass while maintaining the outer surface. Figure 2.15 demonstrates how DfAM practices and the use of internal structures can be used to tailor a part's design to its functionality.

Design Consolidation. AM allows the fabrication of an assembly that would normally require integration of multiple parts as one monolithic structure [33]. Design consolidation eliminates the need for assembly after production, reducing required lead times and decreasing total part count of a system. Additionally by eliminating the joint interfaces between parts, the stiffness of the structure increases and the failure modes associated with these interfaces are eliminated.

Optimization and Customization. The use of CAD and FEA can be leveraged to generate parts that are optimized for their specific purposes. For components that

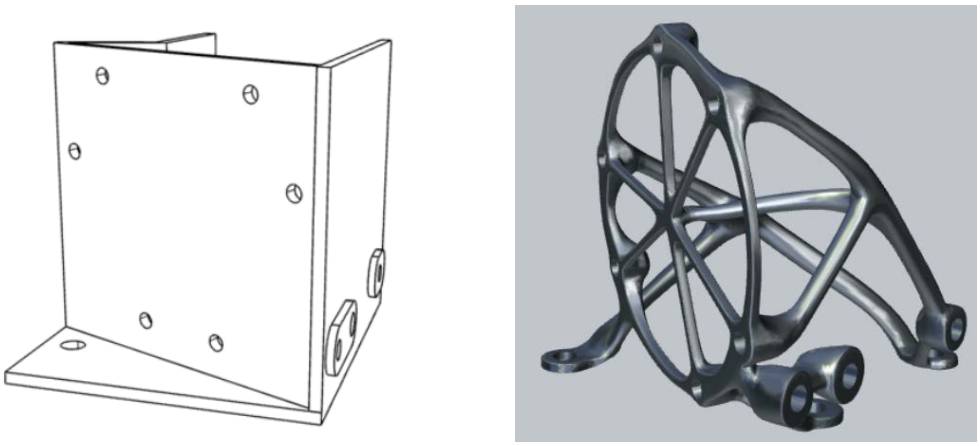

Figure 2.16. Camera star tracker bracket: traditional design vs DfAM [44]

have strict lower bound frequency requirements, FEA can be conducted to verify its modal characteristics and tailor the structure to meet those requirements [44]. Figure 2.16 shows how in such a situation a traditional bracket can be optimized to mount a star tracker, a typical spacecraft component. Topology Optimization (TopOpt) is a commonly applied process used to optimize AM designs. TopOpt is a numerical method that optimizes the distribution of material within a specified design space based off the boundary conditions, loads, and constraints [48]. The ability to fabricate highly complex parts complements the solutions provided by TopOpt algorithms.

2.4.3.3 Multi-Functional

The design flexibility of AM has resulted in research and development of multi-functional parts. This approach has significant appeal in systems that are limited in size and mass such as a CubeSat. Through AM, parts can be designed to accomplish more that just their primary function. Figure 2.17 demonstrates the potential of multi-functional structures. Using AM, a rectangular shaped propellant tank, including the plumbing and nozzles of a propulsion system can be designed into the primary structure of the CubeSat chassis [13]. Additional applications of multifunc-

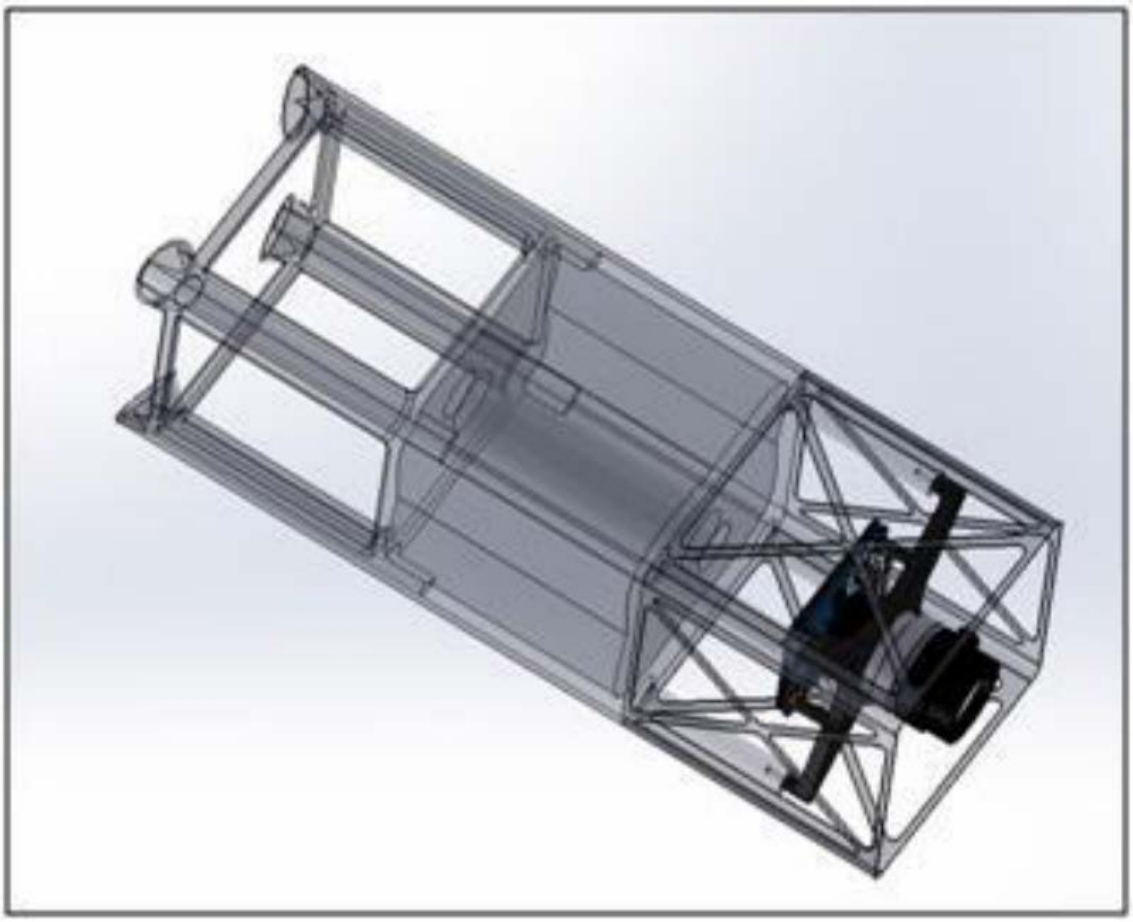

Figure 2.17. 3U CubeSat structure with integrated propellant tank AM [13]

tional parts could be thermal management, utilizing of cooling channels throughout the outer structure of the chassis; or embedding electronic components within support structure [13, 49]. The use of these types of multi-functional structures has been estimated to dramatically reduce the volume and mass of a spacecraft and decrease the assembly and required finishing rework labor [13].

2.5 TPMS Structures

TPMS structure were discovered in biological systems such as weevils, butterflies, and beetle shells [50, 51, 52]. Studies have shown that these structures can be used to provide superior physical and mechanical properties [53, 54]. TPMS structures are

composed of complex 3D structures with minimal surface area that repeat periodically in three dimensions [55, 56, 57]. These structures provide an array of beneficial characteristics such as a high stiffness-to-weight ratio, heat dissipation and heat transfer control, and mechanical energy absorption [12]. TPMS structures have also been found to offer beneficial vibrational damping characteristics [58]. These characteristics make TPMS structures a strong suitor for developing lightweight structures in the aerospace industry [59, 60]. This section will discuss the various types of TPMS structures and their structural characteristics.

2.5.1 Types of TPMS Structures

There are numerous different TPMS structures that can be generated utilizing mathematical periodic geomteric or sinusoidal relationships. An equation for a gyroid is presented in Eq 2.2,

$$G = cos(k_x x)sin(k_y y) + cos(k_y y)sin(k_z z) + cos(k_z z)sin(k_x x) \tag{2.2}$$

with the periodicities defined by

$$k_i = 2\pi \frac{n_i}{L_i} \tag{2.3}$$

where n_i are the number of unit cells repeated in x, y, and z directions, and L_i are the absolute sizes of the structure in those directions [61, 62, 63].

Various TPMS structures can be based on these equations by either thickening the minimal surface or by solidifying the volumes enclosed by the minimal surface [52]. Thickening the minimal surface results in a sheet-based TPMS structure; while solidifying the enclosed volume results in a structure composed of TPMS struts referred to in the literature as a skeletal-based TPMS structure [52]. Figure 2.18 shows a few examples of common skeletal-based and sheet-based TPMS structures.

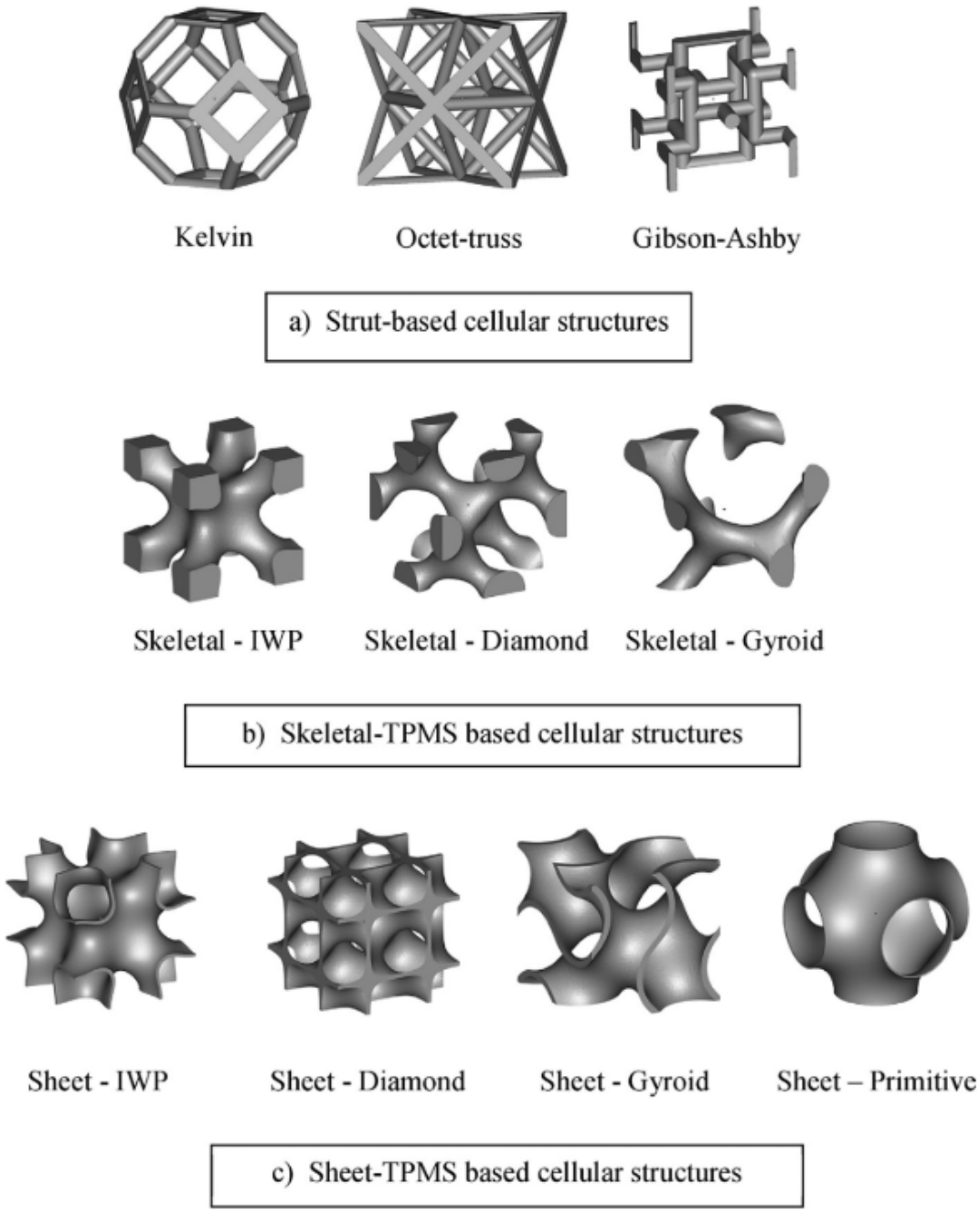

Figure 2.18. Unit cell of different TPMS geometries [12]

2.5.2 Structural Characteristics

The continuous and smooth contours of TPMS structures provide greater structural integrity in comparison to other high stiffness-to-weight structures such as tra-

ditional lattices [64, 53]. In lattice structures, the strut joints are much weaker than the interfaces of the continuous surfaces of TPMS structures due to stress concentrations in the the strut joints [65]. The elastic and plastic properties of a traditional lattice can be severely impacted by imperfections at the joints [53]. The continuous surfaces also eliminates the issue of unconnected struts occurring if the dimensions of the structure is not a multiple of the unit cell of the lattice. An example of this phenomena is depicted in Figure 2.19. These unconnected struts provide no additional strength at the cost of their weight, reducing the effective weight-to-stiffness ratio of the structure.

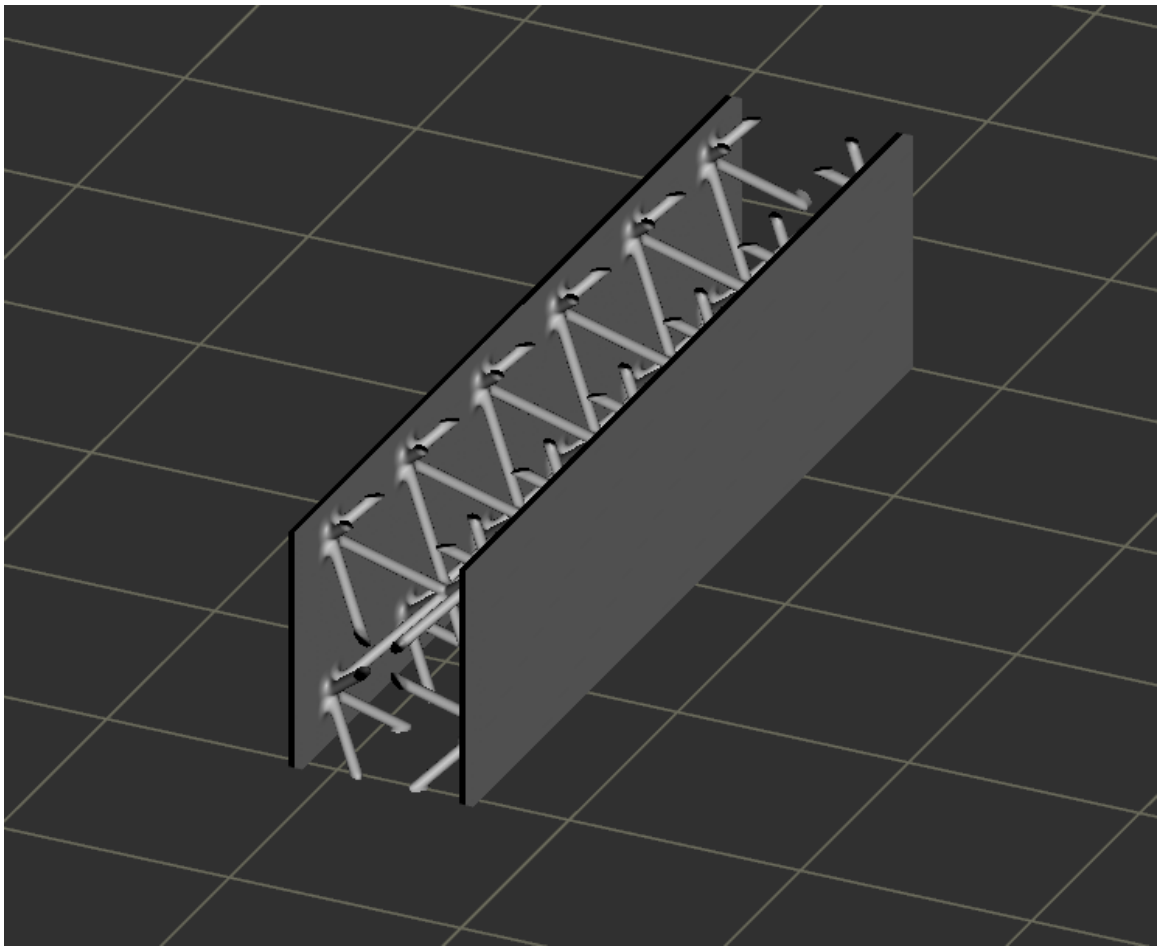

Figure 2.19. Example of unconnected lattice struts in a sandwich beam

A study from the Masdar Institute of Science and Technology evaluated the struc-

tural characteristics of various TPMS structures through compression testing of equivalent sized cubes [12]. Figures 2.20-2.22 provide the results for the Young's Modulus, peak stress, and toughness of various types of TPMS at equivalent relative densities. As can be seen from these figures, the sheet-based structures significantly outperformed the skeletal-based structures in all three properties regardless of density. The high toughness and Young's Modulus of these structures is promising for the design of sandwich panels due to their corresponding suitability for energy absorption and higher stiffness-to-weight ratio [12]. Of the various sheet-based structures, the diamond geometry performed best with the gyroid geometry second. The gyroid and diamond structures were additionally found to exhibit more uniform stress distributions than the other geometries [61]. For these reasons the research herein will focus on the use of sheet-based TPMS structures.

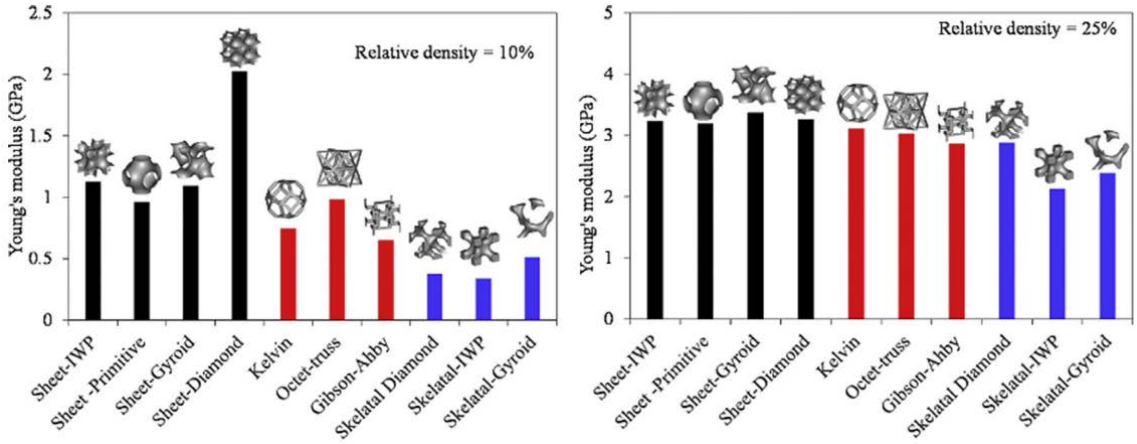

Figure 2.20. Young's Modulus of TPMS structures at relative densities of 10% and 25% [12]

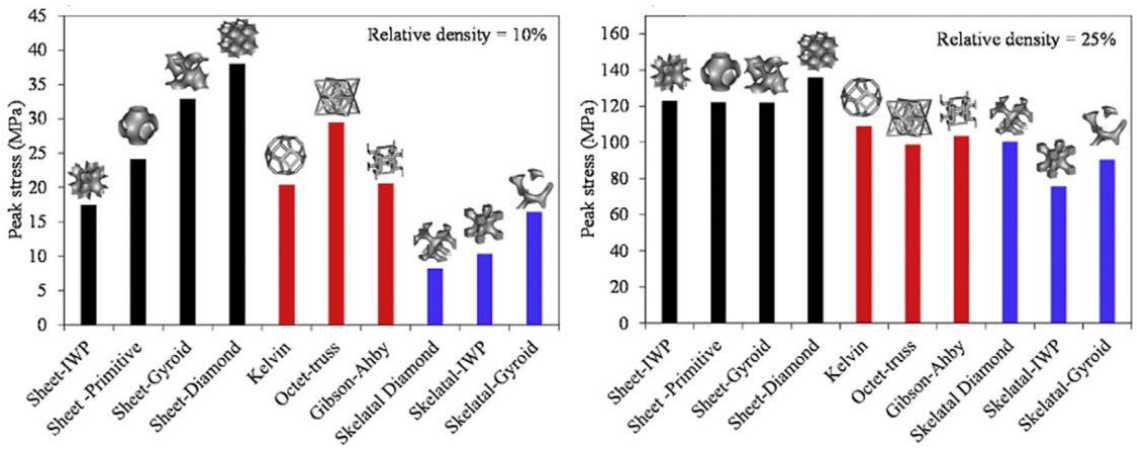

Figure 2.21. Peak Stress of TPMS structures at relative densities of 10% and 25% [12]

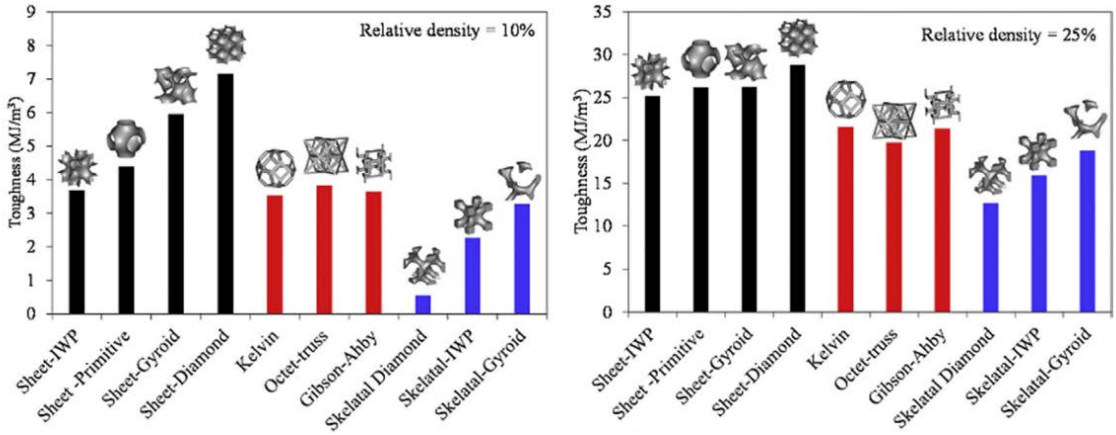

Figure 2.22. Toughness of TPMS structures at relative densities of 10% and 25% [12]

2.6 Summary

This chapter provided background information covering, the basic elements of a CubeSat, the launch environment, and the requirements a satellite must meet, AM parameters, and the benefits of TPMS structures. Knowledge in these areas is essential to developing a "high performance" additively manufactured CubeSat chassis. The information covered in this chapter along with methodologies from previous work in this area will have significant influence on the methodology employed in this research. The following chapter will discuss the methodology and results of the topology study; the first of four studies conducted to achieve the goals in this

research.

III. CubeSat Topology Study

3.1 Chapter Overview

The objective of the study conducted in this chapter was to determine the best topology of the bus structure. As discussed in Chapter 2.4, Additive Manufacturing (AM) greatly expands the design space while adding its own unique constraints. Multiple structures employing Design for Additive Manufacturing (DfAM) practices were designed to meet the CubeSat and payload interface requirements. The designs were evaluated based on their stiffness-to-weight ratio as determined by Finite Element Analysis (FEA). The FEA was limited to evaluating competing designs in this chapter, not for evaluating the experimental results of the final design in Chapter VI. The sections in this chapter provide further details on the design parameters, evaluation criteria, and results of the study.

3.2 Methodology

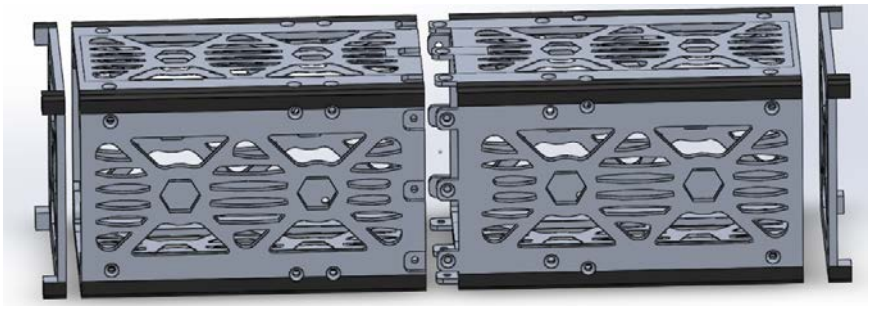

Figure 3.1. Roberts' Male/Female Interface Design [11]

The size limitation of the M2 build chamber required the bus structure to be fabricated in two connecting halves which also may have unintended utility during payload assembly and integration. Roberts explored the potential interface designs for his lattices based aluminum CubeSat bus structure. Leveraging the conclusions in Roberts'

research the male/female design shown in Figure 3.1 established the blueprint for the topology designs explored in this chapter [11]. The focus of the study herein was on the remaining structure with goal to maximize stiffness and minimize weight.

The topology of the design was constrained by the requirements set by the CubeSat specification and the Poly Picosatellite Orbital Deployer (PPOD) [20]. It was essential these requirements were incorporated into the design. The dimensional requirements established by the PPOD constrain the outer dimensions of the CubeSat bus structure and specify requirements for the rail interface. The PPOD specifications for a 3U CubeSat are shown in Figure 3.4.

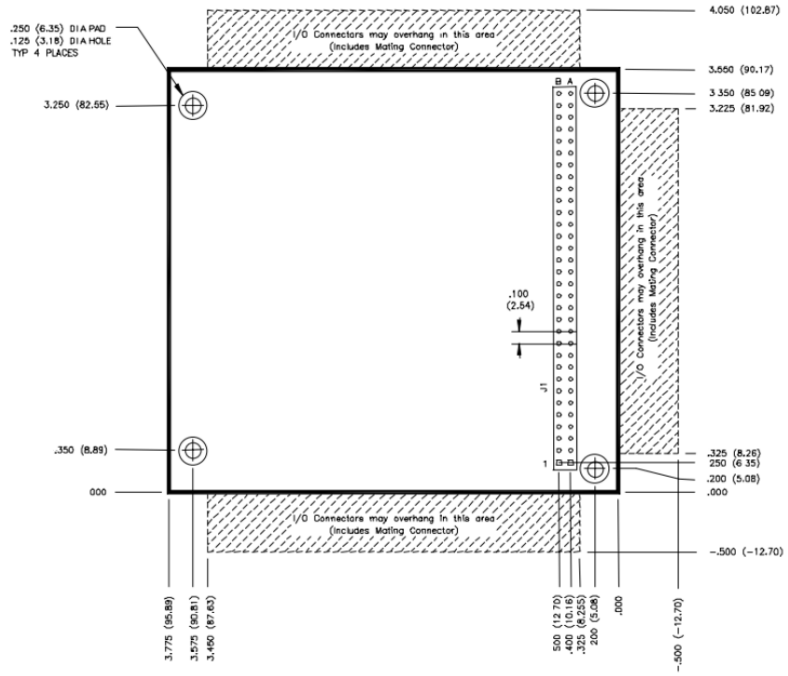

Figure 3.2. PC/104 Layout [66]

The internal dimensions are limited by the volume required by the payload. The PC/104 specification is a commonly used architecture for the circuit boards and electronic stacks within a CubeSat. Figure 3.2 provides the specification of the PC-104 circuit board. Generally, subsystems are comprised of components following this form factor to remain consistent with their corresponding circuit boards. Therefore,

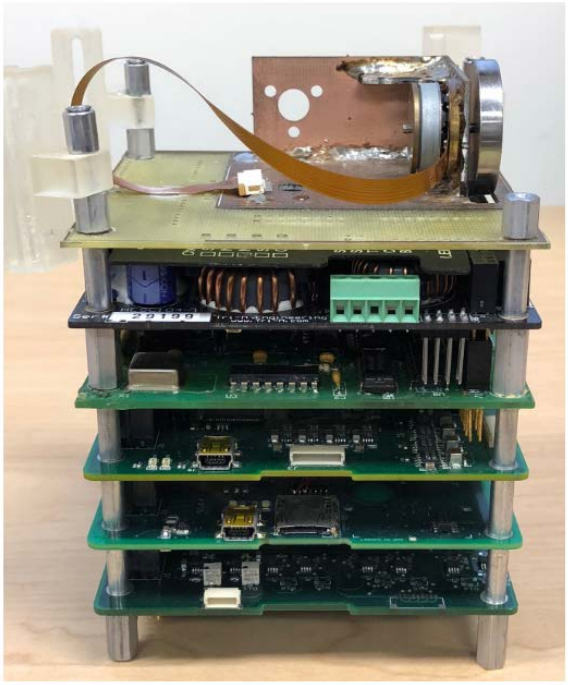

Figure 3.3. CubeSat PC/104 Payload stack [11]

the internal volume was designed to support payloads following this form factor. Additionally, it was essential the structure provided interfaces compatible with the PC/104 mounting pattern at the four corners of each board for payload integration.

The PPOD and PC/104 specifications limited the maximum wall thickness of the structure to 4.9 mm. As the thickness of a beam increases, the bending stiffness significantly increases, especially in sandwich structures. To maximize this benefit while providing a buffer to ensure the PC/104 stacks would fit within the payload, a total wall thickness was utilized throughout the designs. Considering the constraints and DfAM principles discussed in Section 2.4, four topologies were designed in SolidWorks (Figure 3.5).

The four piece design was modeled as single solid monolithic structure to reduce complexity. This decision was justified because the objective of the study was to determine relative performance of the topology designs rather than the actual performance. Additionally, the screw rods from the PC/104 stacks were included as they

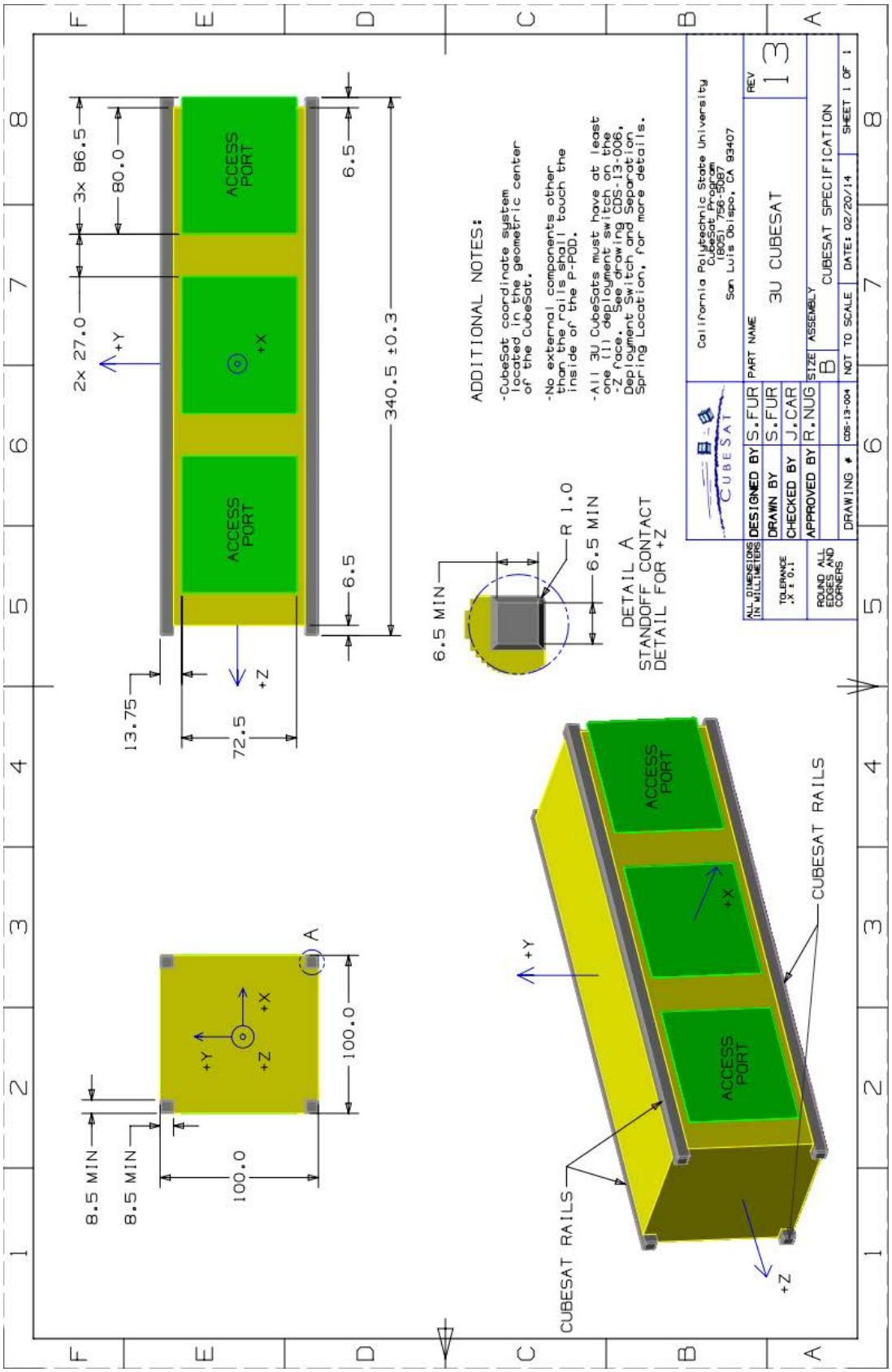

Figure 3.4. 3U CubeSat Specifications [20]

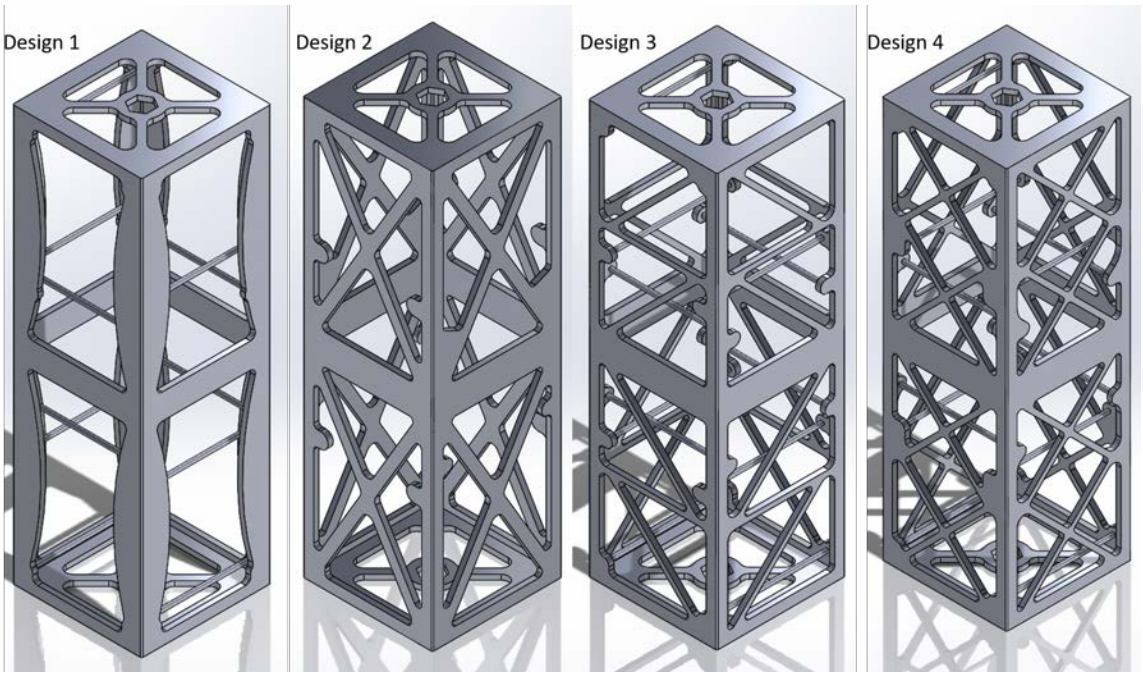

Figure 3.5. CubeSat Topology Design Options

provide significant structural support when the stacks are integrated into the CubeSat. The solid band at the center of the design represents the volume required for the male/female tab interface. Finally, it should be noted that these designs contain at least one overhang, violating a DfAM rule discussed in Section 2.4. This decision was made purposely as the locations of the overhangs permits access to use wire electrical discharge machining (EDM) to burn the desired contour. The "as built" model would abide by the 45 degree rule and final shape would be obtained by machining away the additional material.

The first design explored a minimalist approach with the objective of maintaining access ports throughout the chassis. The increasing thickness at the center of the beams was intended to provide additional bending support in the absence of additional supports. The three remaining designs embodied a truss design approach. Trusses are commonly used in structures ranging from bridges to skyscrapers due their ability to provide superior structural support while minimizing mass. This makes trusses ideal

for this application. For all three designs the widths of the rails were reduced to the minimal requirement of 8.5 mm in accordance with the CubeSat specification. Tabs were added to provide attachment points at the various PC/104 locations. The second design incorporated a simple X truss pattern spanning the corners. The diagonal truss elements provided additional support to the structure, significantly increasing the bending stiffness. Design 3 followed a Z truss pattern known as a Pratt or Howe truss, a simple design commonly used in bridges [67]. This design is generally used for loads in line with the horizontal member, corresponding with the plane where bending is expected to be greatest. Additionally, this design enabled the span and thickness of the individual truss elements to be reduced; minimizing total volume. The width of the truss elements were reduced to 4mm, matching the thickness, resulting in 4 mm x 4 mm truss elements. A square cross section provides the optimal moment of inertia $I = \frac{bh^3}{12} = \frac{b^4}{12}$, as $b = h$. Decreasing the width further would provide diminishing returns for the mass savings. The fourth and final design incorporated two X truss supports following the same width dimensions as design 3. Incorporating two X truss patterns further reduced the span of the truss elements at minimal increase of total volume. Additionally, eliminating the horizontal truss members reduced the required post processing.

The designs were evaluated through an FEA simulation conducted in Abaqus. Solid structure was used in the FEA simulation due to the computational demand required to incorporate a Triply Periodic Minimal Surface (TPMS) sandwich structure. This decision was made under the same considerations as modeling the structure as a single structure. A solid structure drastically reduces the complexity of the model and by maintaining equivalent material properties between all four designs, the objective of determining the best topology was achieved. The Inconel 718 material properties from Special Metals data sheet were used for this simulation resulting in the following

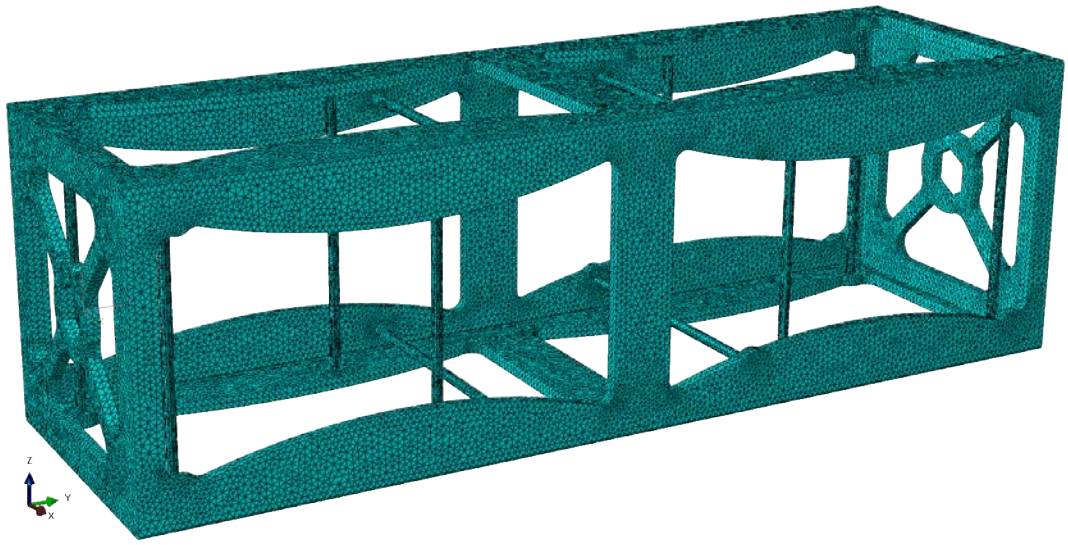

Figure 3.6. Design 1 - 2mm Global Mesh

values after converting to consistent units (Table 3.1): Density, $\rho = 8.19\text{e-}9$; Modulus of Elasticity, $E = 2.08\text{e-}5$; Poisson's Ratio, $\nu = 0.294$ [68].

Table 3.1. Consistent Units

Quantity	SI	SI (mm)	US Unit (ft)	US Unit (inch)
Length	m	mm	ft	in
Force	N	N	lbf	lbf
Mass	kg	tonne (10^3 kg)	slug	lbf s^2/in
Time	s	s	s	s
Stress	Pa (N/m^2)	MPa (N/mm^2)	lbf/ft^2	psi (lbf/in^2)
Energy	J	mJ (10^{-3} J)	ft lbf	in lbf
Density	kg/m^3	$tonne/mm^3$	$slug/ft^3$	lbf s^2/in^4

The designs were evaluated under a free-free boundary condition. This decision was made because the PPOD rail interfaces only constrain large deflections the CubeSat; sufficient tolerance remains for small deflections to occur in all directions. Thus, a free-free boundary condition was determined to be the most representative environment of the system while in the PPOD. A convergence study was conducted for each design to ensure a sufficient number of elements were employed in the mesh.

Convergence was defined as a less than one percent change in frequency from the previous iteration. An example of a 2 mm element mesh for design 1 was depicted in Figure 3.6. After verifying convergence was achieved, the fundamental frequency corresponding to the first mode for each design was recorded and tabulated. The design with highest frequency was considered the "best" design to be used in the final bus structure study discussed in Chapter VI.

3.3 Results

Table 3.2. Convergence Study

Model	Element Size (mm)	Total Elements	Total Nodes	Frequency (hz)	% Change
Design 1	4	140551	240065	492.54	-0.22%
	2	452376	729635	491.47	
Design 2	4	202253	335791	1007	-0.10%
	2	757231	464891	1006	
Design 3	4	219527	365032	862.14	-0.35%
	2	558945	901369	859.08	
Design 4	4	259789	425263	1183.5	-0.61%
	2	541794	879431	1176.3	

Table 3.3. FEA Results

Model	Frequency (Hz)	Volume (mm^3)	Elements	Nodes
Design 1	491.5	210.6	452,376	729,635
Design 2	1006.0	205.4	464,891	757,231
Design 3	859.1	163.6	558,945	901,369
Design 4	**1176.3**	**178.2**	**541,794**	**879,431**

The convergence study was conducted using C3D10 quadratic tetrahedral elements beginning with a 4 mm global element size. After one iteration to a 2 mm global element size, it was demonstrated that all models had already achieved convergence as portrayed in Table 3.2. Although the 4 mm models were determined to be converged,

the 2 mm models were used for higher resolution. Figure 3.7 shows the first mode shape for each model. The corresponding natural frequencies and mesh parameters were listed in Table 3.3. From these results it was clear that the X pattern trusses provided superior stiffness. The mode shapes of Design 1 and Design 3 were both characterised by similar deformation where the entire midsection of the chassis was compressed. The X pattern in Design 2 and Design 4 prevented this from occurring at a low frequency; instead the mode shapes of these design were characterized by first bend in the individual truss elements. Due to the greater span of the truss elements of Design 2, its natural frequency was lower than Design 4. Therefore, Design 4 exhibited the highest frequency and was determined to be the "best" topology. This topology will be the foundation for the final structural design covered in Chapter VI.

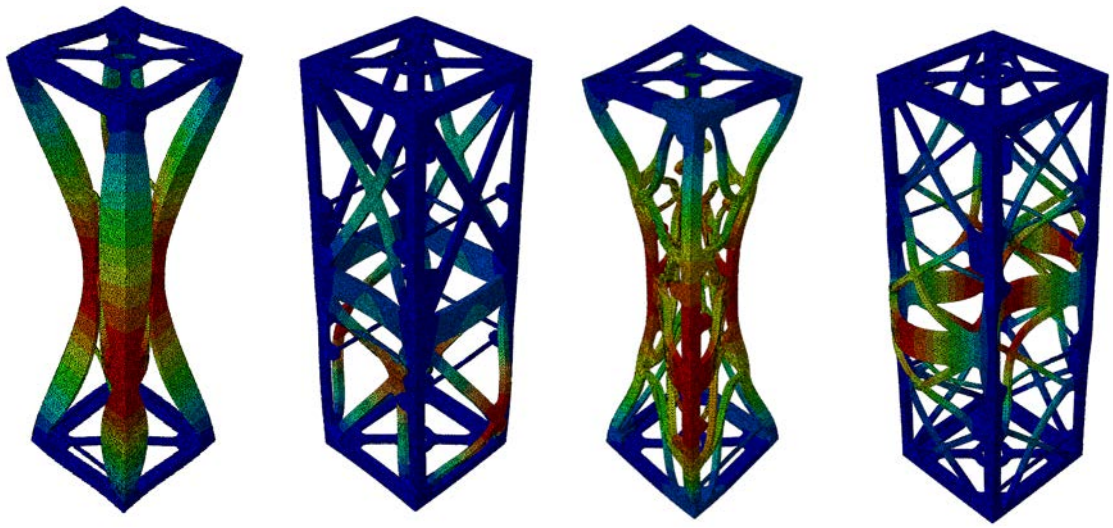

(a) Design 1 **(b)** Design 2 **(c)** Design 3 **(d)** Design 4

Figure 3.7. Mode Shape corresponding to the First Fundamental Frequency for each Design

3.4 Summary

This chapter covered the methodology and results for the topology study conducted, which provided pertinent data on the topology to be used in the final design

and manufacturing of the bus structure. Additionally the topology provided an initial estimate of the chassis' total volume. With this information a maximum density of the metamaterial could be established to ensure the chassis would be structurally mass efficient. The rule of thumb for an efficient structure is 8-12% of the total allowable mass [22]. The total allowable mass for a 3U CubeSat is 4 kg [20], corresponding to structurally efficient mass of 320-480 g. Based off the final volume of the chosen design, 178.2 cc, the maximum density was calculated to be 2.37 g/cc after factoring the mass volume. This calculation accounted for mass and volume estimates of interface regions such as the male tabs and hole locations that would require solid structure. The maximum density provided a means to discriminate metamaterials evaluated in Chapter V. The following chapter covers the trade study conducted to determine the optimal metal powder for this research.

IV. Material Selection Trade Study

4.1 Chapter Overview

In this chapter a trade study was conducted to determine the preferred material for designing and fabricating a metamaterial with a high stiffness-to-weight ratio via Additive Manufacturing (AM). The alloys evaluated were limited to common metals used in Laser Powder Bed Fusion (LPBF) AM processes. The following alloys were considered: Inconel 718 (nickel-based), SS 316 (iron-based), AlSi10Mg (aluminum-based), and Ti6Al4V (titanium-based). The material properties of an AM alloy can vary significantly based off the printer used and printing parameters. To reduce this variation, the material properties from Concept Laser's material data sheets were used in this evaluation. Table 4.1 lists the alloys and their corresponding material property values. The sections in this chapter cover the methodologies employed in this study, establish the evaluation success criteria, and provide analysis of the data.

Table 4.1. Material Properties of Concept Laser Powder Alloys [69, 70, 71, 72]

Material	Density (g/cc)	Yield Strength (MPa)	Modulus of Elasticity (GPa)	Coefficient Thermal Expansion (µm/m-K)
AlSi10Mg	2.68	205	75	20
Inconel 718	8.19	951	200	13
SS 316	7.99	330	200	15
Ti6Al4V	4.42	989	110	9

4.2 Methodology

Five criteria, as shown in the heading row of Table 4.2, were chosen to evaluate the various alloys. The criteria were ranked in the following order from greatest

to least important: Specific Stiffness, Printability, Coefficient of Thermal Expansion (CTE), Cost, and Specific Strength. Specific stiffness ($\frac{E}{\rho}$) was ranked highest because it provides a direct relation to the stiffness-to-weight ratio of the metamaterial.

Table 4.2. Material Trade Study Criteria Values

Material	Specific Stiffness (10^6 m^2/s^2)	Printability	Coefficient Thermal Expansion (µm/m-K)	Cost ($/kg)	Specific Strength (kN-m/kg)
AlSi10Mg	28.0	3	20	85.47	76.5
Inconel 718	24.4	8	13	125.36	116.1
SS 316	25.0	10	15	91.17	41.3
Ti6Al4V	24.9	9	9	313.39	223.8

Printability was ranked second due to the importance of being able to print structures with extremely fine features. The ability to print fine features expands the geometric design envelope of the metamaterial and enable structures with greater stiffness-to-weight characteristics. Due to limited scope of the research, printability could not be determined quantitatively, therefore a scale of 1-10 was utilized, with ten being the best. The values were based on past experience at Air Force Institute of Technology (AFIT) and data available in current literature. The AlSi10Mg, aluminum based powder was given the lowest rating of 3. Literature has shown that aluminum powders are much more difficult to print than steel or titanium alloys due to their high reflectivity, high transfer of heat away from the melt pool, and the formation of oxides that occur [43]. Additionally, the inability to print fine structures (<250 micron) in aluminum was demonstrated in Roberts' research as shown in Figure 4.1. Based off samples printed at AFIT, stainless steel was evaluated to be the best in terms of printability and thus rated as ten. Literature has shown that titanium alloys allow similar control to stainless steels, however the greater melting temperature, requiring greater input power, adversely effects the material's printability [43]. Based

off this information and considering Ti6Al4V powder is highly reactive, Ti6Al4V was rated as a nine. Inconel 718 was rated as an eight based off comparisons of Inconel 718 samples to SS 316 samples printed at AFIT as will be shown in the Chapter V.

Figure 4.1. AlSi10Mg Lattice Based CubeSat Chassis [11]

Satellite payloads generally consist of sensitive instruments that can be adversely affected by small variations in the environment. A significant portion of development is devoted to engineering systems to protect and isolate these instruments. A chassis fabricated from a material with a low CTE reduces the deformation the satellite and the payload experience due to the large temperature fluctuations that occur as the satellite transitions in and out of the Earth's shadow. Considering these factors, CTE was ranked third in importance, and is an easily quantifiable metric.

The final two criteria and least important were cost and specific strength. Although reducing cost is a top priority of satellite developers, the cost of the material is only a percentage of the total cost to manufacture part through AM. Equipment and labor costs for setting up, removal, and material post processing account for majority of the manufacturing costs. The cost of each powder was obtained through directly quotes from Concept Laser's sales department [73]. Specific strength is ranked as

the least important criterion because satellites undergo minimal static loading during their lifetime. The satellite chassis must be able to withstand the compression loads due the Launch Vehicle (LV)'s acceleration during launch and the ejection force from the Poly Picosatellite Orbital Deployer (PPOD). Generally, the specific strengths of all four alloys will be sufficient to meet the minimum static loading requirements if the fundamental frequency requirement is met.

The criteria weighting values were determined using a rank order centroid calculation as shown by Equation 4.3. This weighting was chosen because it provided a greater weighting to specific stiffness and printability. Only these two criteria directly impact the stiffness-to-weight ratio of the structure. The remaining criteria provide ancillary benefits that may be desired and should be considerations. However, their value is significantly less than that of the primary two criteria, which account for 72% of the total score. Table 4.3 illustrates these values along with the minimum and maximum values of the value function for each criterion. The minimum range values were set to zero for each criterion and the maximum range values were set to the maximum value of the materials for the given criterion. The normalized criteria value for criteria with an increasing value function was established from Equation 4.1. The normalized criteria values for decreasing value functions were computed using Equation 4.2.

$$NV_{increasing} = \frac{value}{max\ value} \tag{4.1}$$

$$NV_{decreasing} = 1 - \frac{value}{max\ value} \tag{4.2}$$

$$w_t = \frac{1}{K} \sum_{j=1}^{k} \frac{1}{r_j} \tag{4.3}$$

Table 4.3. Material Criteria Weighting and Ranges

			Criteria Range		
Criteria	Weighting	Units	Minimum	Maximum	Value Function
Specific Stiffness	0.46	10^6 m^2/s^2	0	28.0	Increasing
Printability	0.26		0	10	Increasing
Coefficient Thermal Expansion	0.16	µm/m-K	0	20	Decreasing
Cost	0.09	$/kg	0	313.39	Decreasing
Specific Strength	0.04	kN-m/kg	0	223.8	Increasing

Where:

K = number of criteria; r_j = rank of jth criterion [74]

4.3 Results

Table 4.4. Material Trade Study Results

			Material Alternatives			
Criteria	Criteria Weighting	Units	AlSi10Mg	Inconel 718	SS 316	Ti6Al4V
Specific Stiffness	0.46	10^6 m^2/s^2	1.00	0.87	0.89	0.89
Printability	0.26		0.30	0.80	1.00	0.90
Coefficient Thermal Expansion	0.16	µm/m-K	0.00	0.35	0.25	0.55
Cost	0.09	$/kg	0.73	0.60	0.71	0.00
Specific Strength	0.04	kN-m/kg	0.34	0.52	0.18	1.00
			0.61	0.73	0.78	0.76

Following the criteria ranges established in Section 4.2 the normalized criterion values for each material were calculated. Table 4.4 summarizes these values in a tabular form and provides the total weighted scores for each material. Despite ranking highest in specific stiffness and cost, AlSi10Mg received the highest score due to its poor printability, CTE, and specific strength. Although the specific stiffness score contributed encompassed nearly half the final score, there was not significant deviation between the remaining materials, reducing the impact of this criterion. SS

316 was determined to be the best material under the criteria and rankings by this trade study. However, it should be noted that Ti6Al4V and Inconel 718 scored 0.76 and 0.73, compared to SS 316's score of 0.78, resulting in a delta of 0.02 and 0.05 respectively. Considering subjectivity of the inputs of the trade study, especially the criteria values for printability, it could be concluded that any of these three materials could be suitable candidates. A common trend of high specific stiffness and superior printability can be associated with these materials. Furthermore, all three of these materials are high stiffness, high density, and small melt pool track width materials.

4.4 Summary

This chapter covered the methodology used to evaluate various AM materials and provided an analysis of the results. Based off the results of the study, the materials were ranked accordingly, from best to worst, SS 316, Ti6Al4V, Inconel 718, and AlSi10Mg. Additionally, it was concluded that due to the small deviation in final scores, any of the three high stiffness, high density, and small melt pool track width materials could be viable materials for designing a metamaterial with fine features. Due to resource constraints, SS 316 could only be printed on AFIT's MLab, restricting the build size to 100 mm. Large parts were required to be printed using Inconel 718 in the larger M2 cusing. AlSi10Mg and Ti6Al4v powder were not permitted at AFIT due their reactive properties. Considering these constraints, the metamaterial design study in Chapter V and final CubeSat Structural bus designed in Chapter VI were mainly comprised of builds from Inconel 718. The following chapter will cover methodology and results of the metamaterial design study conducted for this research.

V. TPMS Metamaterial Design Study

5.1 Chapter Overview

The objective of this study was the design and evaluation of a metamaterial with performance characteristics superior to materials commonly used in current space systems. As discussed in Section 2.3, stiffness is the most important structural performance characteristic of the satellite bus structure. Generally, and specifically due to the shape of a 3U CubeSat, the primary mode shape of the structure is in bending. With this in consideration, metamaterial based off a Triply Periodic Minimal Surface (TPMS) sandwich structure was pursued due to the superior bending stiffness sandwich structures afford. The thickness of the sandwich structure has a significant effect on the bending stiffness of the metamaterial. As the overall thickness of the sandwich structure increases, the sandwich walls move further from the centroid drastically increasing the moment of inertia and the corresponding bending stiffness of the metamaterial. However, the greater the overall wall thickness the smaller the internal volume for the payload. The overall wall thickness was chosen to be 4 mm based of the results of the topology study conducted in Chapter III. It was determined this provided the optimal stiffness while meeting dimensional requirements. The width and height of the test specimens where chosen to be 25.4 mm x 175 mm respectively. This decision allowed the TPMS based metamaterials to be evaluated against the lattice based metamaterials tested in Roberts' research.

As discussed in Section 2.2, the primary objective of designing CubeSat bus structure was to maximize stiffness while minimizing weight. To meet this objective each metamaterial was evaluated based off equivalent density and natural frequency. To ensure that the final mass of the bus structure was under the 480 gram goal, only metamaterials with densities less than 2.37 g/cc were considered based off the results

from the Topology study conducted in Chapter III. The natural frequency was chosen due to the direct relation between the natural frequency and stiffness-weight-ratio. This relationship was discussed in Section 2.3, and illustrated through Equation 2.1. Therefore, the metamaterial with highest natural frequency within the required density range will be used for the final chassis design.

5.2 Methodology

5.2.1 Beam Design and Manufacturing

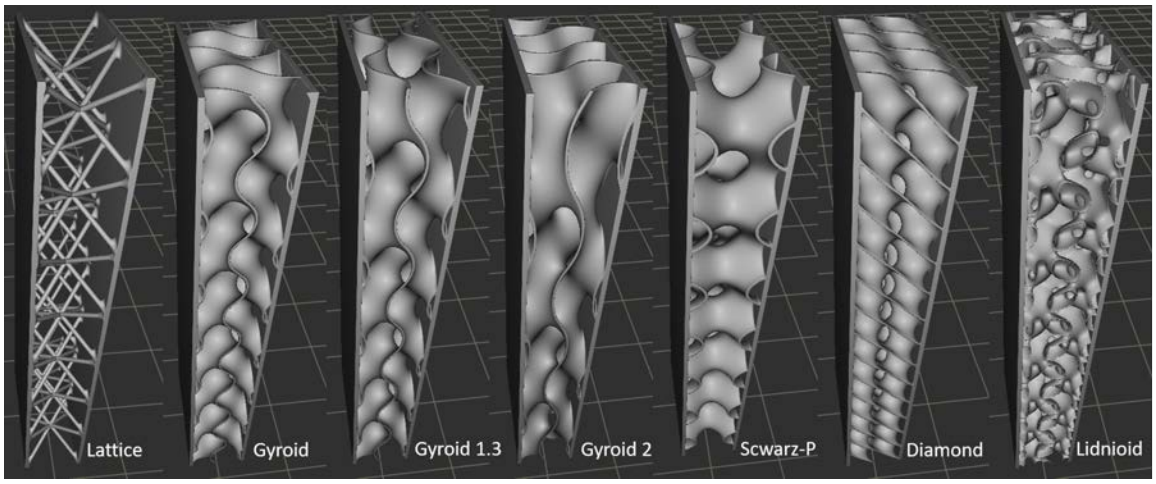

Figure 5.1. Implicit nTopology Models

The first challenge of this research was modeling and printing the TPMS structures. nToplogy's latest software reduced the complexity of the first step of this process. Primitive implicit shapes could be quickly generated and converted into TPMS volumes. Through boolean operations, the walls and TPMS infill could be combined to form the desired beams as seen in Figure 5.1. Additionally, nTopology's software enables the implicit volumes to be sliced, contoured, and hatched without generating a Standard Tessellation Language (STL). Figure 5.2 illustrates a beam sliced at 5 mm intervals, while Figure 5.3 depicts an expanded view of a single layer. The contours and hatching were directly exported as a Common Layer Interface (CLI) file. Elimi-

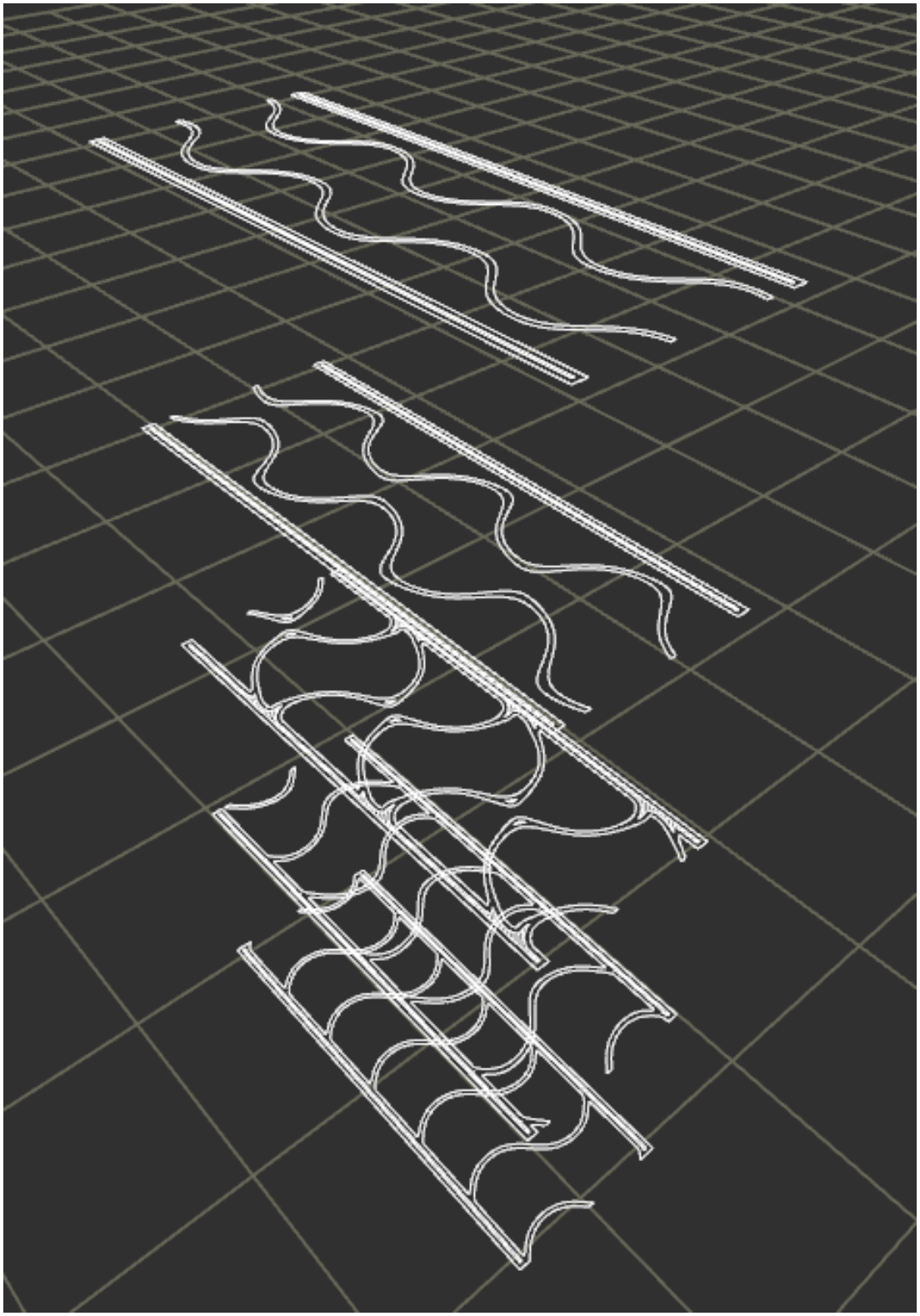

Figure 5.2. nTopology CLI generation

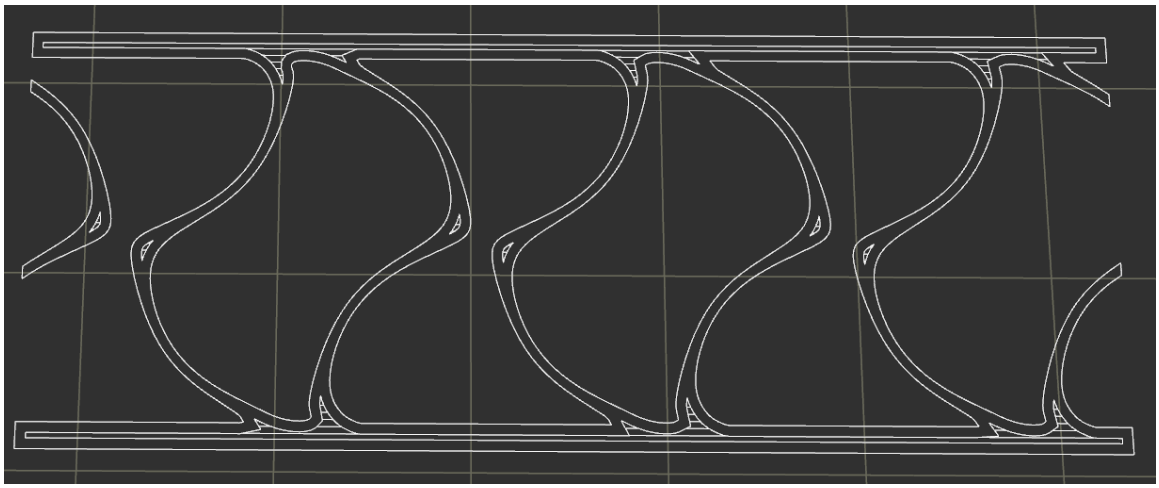

Figure 5.3. CLI Single Slice

nating the need to convert the implicit to a STL ensured the contours maintained the continuous sinusoidal paths generated by the implicit model. Prior to printing a full size build on the M2 cusing, a smaller test build was conducted on the MLab printer to verify printability of TPMS features and to ensure the equivalent densities of the metamaterials were within the required limit.

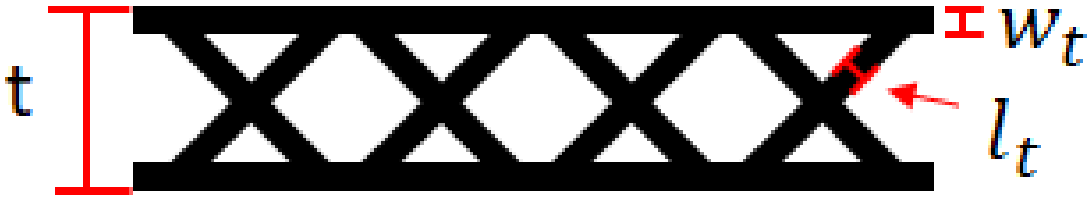

Figure 5.4. Lattice Wall Variable Descriptions

For the initial test build, four types of TPMS structures and a lattice structure were explored. The lattice structure was included to provide a direct comparison to the optimal lattice metamaterial tested in Roberts' research. According to Roberts the best thickness value for the lattice struts (l_t) and sandwich walls (w_t) were found to be 0.25 mm [11]. Figure 5.4 provides clarification of these thicknesses in relation to the overall thickness (t). The same thickness values were utilized in this study. The

size of the unit cell of a TPMS structure is determined by its assigned periodicity in nTopology. The desired unit cell size was determined to be 4 mm, ensuring a full period was obtained in the smallest dimension. The relation between periodicity, unit cell size, and engineering units in nTopology is defined by Equation 5.1. The resulting periodicity for a 4 mm unit cell was calculated to be 0.638. This periodicity was applied in each direction for all four types TPMS structures providing a uniformly distributed infill. Two additional gyroid based beams were designed with periodicities scaled by 133% and 200% in the z direction to examine the effect this would have on mass and bending stiffness.

$$Periodicity = \frac{\pi}{2} * \frac{d}{10} \tag{5.1}$$

where d = unit cell size.

Table 5.1. MLab cusing Print Parameters

Parameter Type	Power (W)	Speed (mm/s)	Spot Size (µm)	Print Layer (µm)	Hatch Spacing (µm)	Contour Offset (µm)
Contour	130	1300	100	30	N/A	N/A
Surface Area	140	1000	100	30	66	100

As discussed in Chapter IV, the MLab cusing was limited to printing in SS 316. The print parameters shown in Table 5.1 were chosen based off Concept Lasers' recommendation for SS 316 powder. The height and width dimensions were 56 mm and 8 mm respectively, allowing for two periods along the width and maintaining approximately the same 7-to-1 height to width ratio as the final beam dimensions. The beams were printed in a vertical orientation in the direction annotated in Figure 5.5. The test print verified the TPMS features could be successfully and accurately printed at the desired thicknesses. Additionally, the printed beams were weighed and measured to determine their equivalent densities as listed in Table 5.2. All metamaterials except the lidinoid based beam and the solid beam met the density

requirement.

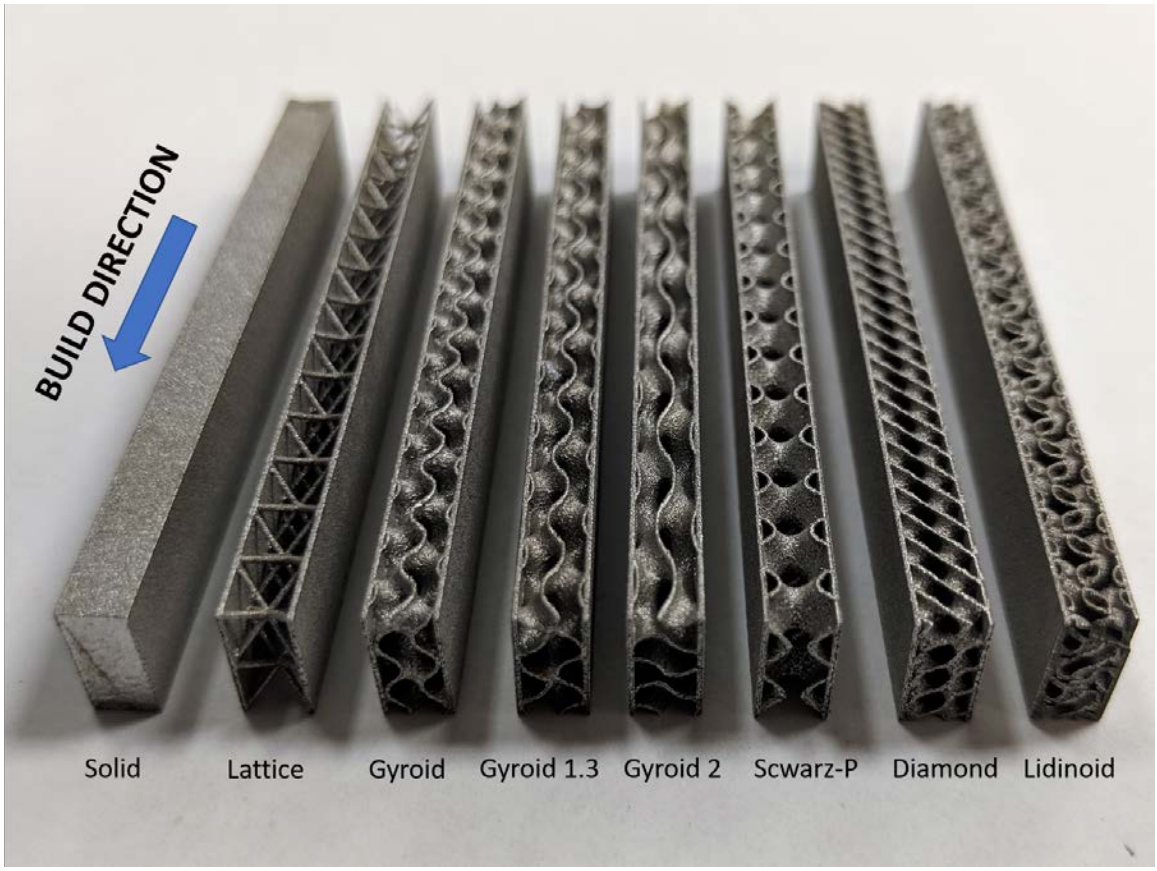

Figure 5.5. Mlab Test Print

Table 5.2. Test Build Measurements

Beam	Length (mm)	Height (mm)	Width (mm)	Mass (g)	Density (g/cc)
Lattice	56.0	4.00	8.00	2.5	1.40
ScwarzP	56.0	4.00	8.00	3.5	1.95
Gyroid 2	56.0	4.00	8.00	3.6	2.01
Gyroid 1.3	56.0	4.00	8.00	3.7	2.06
Gyroid	56.0	4.00	8.00	3.8	2.12
Diamond	56.0	4.00	8.00	4.2	2.34
Solid	56.0	4.00	8.00	14.2	7.92
Lidinoid	56.0	4.00	8.00	5.7	3.18

*red shading indicates values not meeting requirements

Table 5.3. M2 cusing Print Parameters

Parameter Type	Power (W)	Speed (mm/s)	Spot Size (µm)	Print Layer (µm)	Hatch Spacing (µm)	Contour Offset (µm)
Contour	120	280	50	40	N/A	N/A
Surface Area	370	700	180	40	130	130

The models from the test build were scaled to the full size dimensions of 4 mm x 25.4 mm x 175 mm holding the wall, TPMS, and lattices thicknesses the same. Following the same process as the test build, Concept Laser's recommended print settings for Inconel 718 were used; these parameters are listed in Table 5.3. It should be noted that the parameters for Inconel 718 on the M2 cusing vary significantly from printing SS 316 on the MLab cusing. Additionally, due to constraints on the quantity of Inconel powder at the time of the build, the beams were printed in a horizontal build direction instead of vertically. To increase the thermal load path to the build plate, the base of the beam was lofted to a cross sectional area 4 mm offset from the base area. Figure 5.6 depicts this design and is representative of the remaining beams.

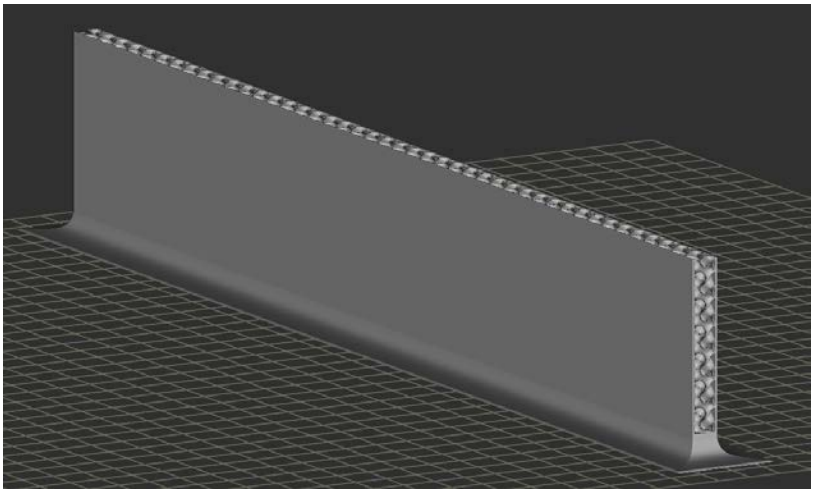

Figure 5.6. Gyroid Horizontal Beam Model

The equivalent density for each metamaterial was calculated from its measured mass and the its equivalent solid volume. This volume represents the space the

metamaterial would fill if it was a solid beam and allows the density to be applied to solid model developed in Chapter III to determine a final mass.

5.2.2 Modal Analysis

The natural frequencies of each beam were measured with the PSV-400 laser vibrometer discussed in Section 1.8. A pseudo free-free boundary condition was employed to reduce the error imparted on the test specimens from the experimental setup. This boundary condition was achieved by hanging the beams by a nylon string, illustrated in Figure 5.7a. Although the string constrained the beam in the Z direction the expected mode shape is first bend out of the X-Z plane. The effects of the nylon string are expected to be insignificant to this mode shape. Input excitation was achieved through an air horn placed near enough to the hanging beam to acoustically excite the beam without contacting it. Depending on the mass of the test specimen the amplitude of the acoustic signal and/or distance from the test specimen were adjusted to ensure contact would not occur. The acoustic excitation from the air horn was driven by a continually repeating chirp signal generated from the Polytec's controller and data acquisition software. The mode shape of the beam was measured by capturing a grid of data points along the 2D face (Figure 5.7c). Polytec's built in spectrum analyzer collects the input signal and velocity data and computes the frequency response function at each scan point. This data can be reconstructed into a 3D animation of the mode shape at the natural frequency.

The natural frequency of a 7075 T-6 aluminum beam was calculated analytically from Equation 5.2 to compare the performance of the metamaterials to an equivalent solid aluminum beam [75]. The dimensions for the analytical model of the aluminum beams were calculated by averaging the dimensions of the printed beams. The elastic modulus and density of 7075-T6 were 71.7 GPa and 2.81 g/cc respectively [76]. Ad-

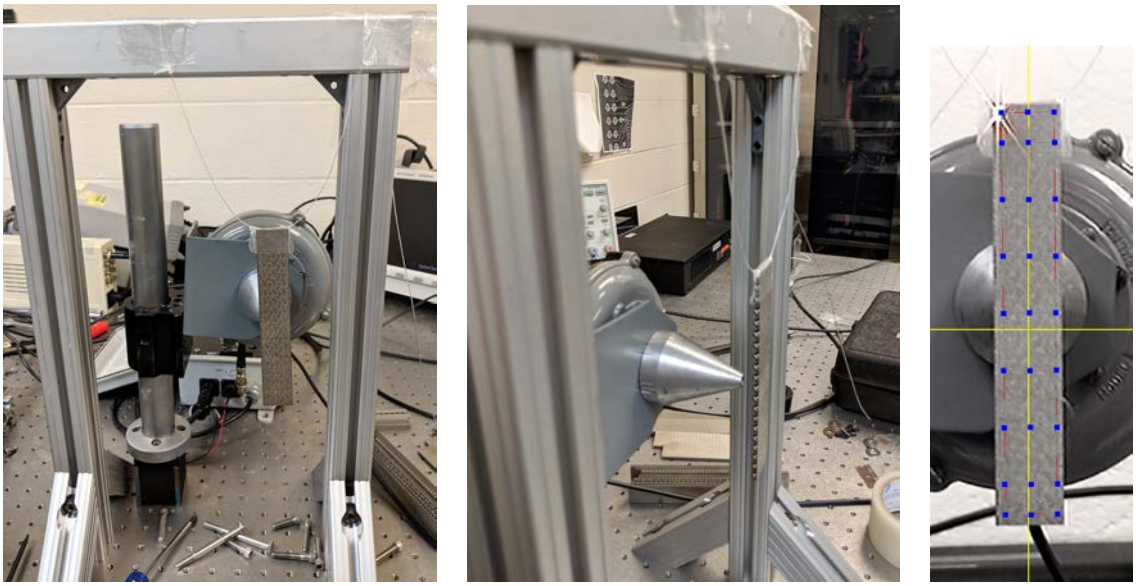

(a) Free-Free Boundary Condition **(b)** Air Horn **(c)** Scan Grid

Figure 5.7. Laser Vibrometer Test Setup

ditionally, the bending stiffness, $k = \frac{EI}{L^3}$, of each beam was calculated by substituting k into Equation 5.2 to obtain Equation 5.3. Solving for k yielded Equation 5.4 where f and m could be measured experimentally.

$$f = \frac{1}{2\pi}\frac{22.373}{L^2}\sqrt{\frac{EI}{A\rho}} \tag{5.2}$$

$$f = \frac{1}{2\pi}22.373\sqrt{\frac{k}{m}} \tag{5.3}$$

$$k = \frac{1}{m}\left(\frac{2\pi f}{22.373}\right)^2 \tag{5.4}$$

5.2.3 Finite Element Analysis

Experimental data provides great insight into the material properties of a metamaterial, however the range of variables that can be evaluated are stymied by the cost and time associated with fabricating and testing each specimen. A validated Finite

Element Model (FEM) vastly expands the metamaterial parameters that can evaluated than feasible in an experimental study. This section covers the methodology employed to build and validate an FEM incorporating the complex TPMS explored in the research. Due to the geometric complexity of TPMS there are no commercial solvers with the native ability to model and evaluate TPMS structures.

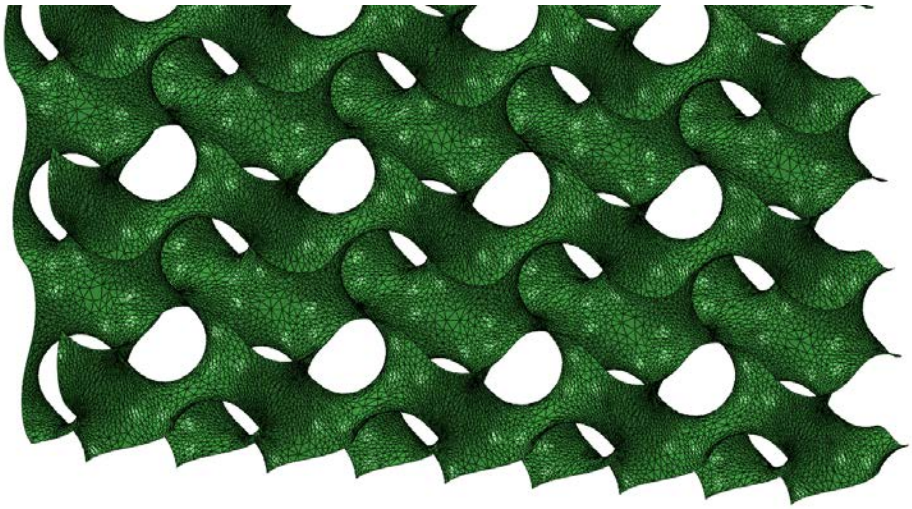

Figure 5.8. Section of Gyroid Beam (0.01 mm Mesh)

Although nTopology's Turbo software provided the ground breaking ability to generate implicit TPMS structures, it was not capable of generating a TPMS shell model at the time of this research. Due to the fine features required for the beams a volume-based model required an exorbitant number of elements to accurately model TPMS structures. A shell model vastly reduces the element count and was determined to be more appropriate due to the thin structures of the TPMS beams. A Matlab script originally used to generate STL files of TPMS cubes of varying periodicity was modified to generate rectangular TPMS structures. The Matlab code and function required for generating these STL files were included in the Appendix A and B. Before the STL files could be imported into Abaqus they were edited in Materialise's Magics software to reduce the mesh and repair any overlapping triangles. Figure 5.8 depicts a section of a final mesh after reducing the minimum triangle element size to 0.01

mm in Magics.

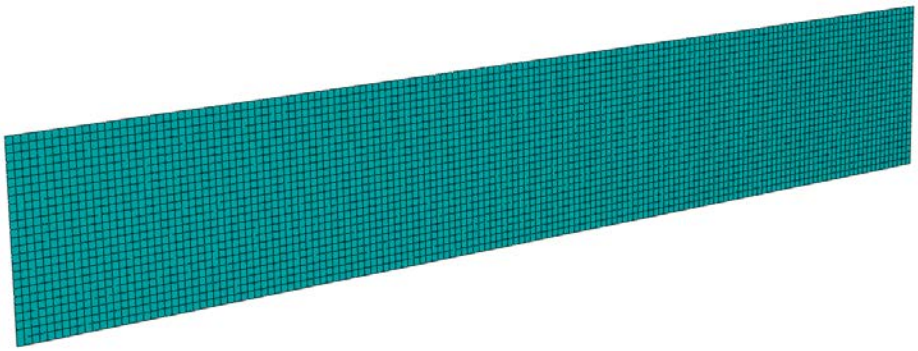

Figure 5.9. Sidewall Mesh (1 mm Element Size)

After modifying the meshes in Magics they were imported into Abaqus. The default element type of linear tetrahedral elements (S3R) were kept for the TPMS mesh elements. The sidewall of the beams were generated directly in Abaqus as 3D deformable planar shell geometries. The sidewalls were meshed independently with quadratic quadrilateral shell elements (S8R). The final sandwich beam structure was created by applying tie constraints to the nodes of TPMS mesh within the defined thickness for the sidewall geometry. The resulting model was illustrated in Figure 5.10.

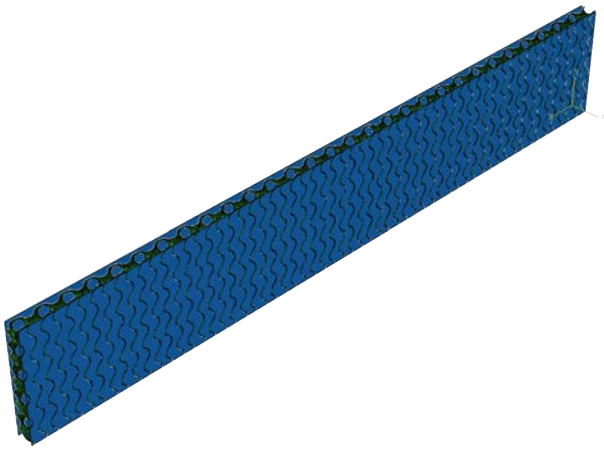

Figure 5.10. Gyroid Beam Model

A two part convergence study was conducted to ensure the appropriate mesh size

was used in the simulation. The first convergence study was conducted on only the TPMS mesh. The triangle reduction minimum element size was varied from 0.1 mm to 0.001 mm in Magics providing coarse to ultra fine meshes. A simple free-free modal analysis was conducted in Abaqus to evaluate mesh convergence. Convergence was defined as the mesh with a frequency within 1% of the subsequent iteration. The second convergence study was conducted on the mesh size of the sidewall after applying tie constraints. The same mesh convergence criteria of 1% was utilized in this study.

The final step of the Finite Element Analysis (FEA) was updating the model to best match the data from the experimental results. Four input variables were available to achieve this objective. The first three input variables were the material properties of Inconel 718; density, modulus of elasticity, and the poisson ratio. The final variable was thickness of the shell structures. The density and modulus of elasticity of a printed part can vary significantly under print conditions. The results from the solid beam provide the means to calculate the printed density by measuring the printed dimensions and mass. Leveraging the measured frequency the modulus elasticity can also be calculated by manipulating Equation 5.2 to solve for E. Updating the thickness was performed by measuring the printed values and comparing the models total mass to ensure it is representative of the printed mass.

$$E = \frac{mL^3}{I}\left(\frac{2\pi f}{22.373}\right)^2 \tag{5.5}$$

5.3 Results

5.3.1 Experimental Analysis

The build on the M2 was successful, however the print quality was poor in comparison to the test build on the MLab. The TPMS infill and sidewalls were noticeably

Table 5.4. Beam Results

Beam	Natural Frequency (hz)	Length (mm)	Height (mm)	Width (mm)	Mass (g)	Stiffness (N /m)	Density (g/cc)
Lattice	793.0	174.0	4.26	25.61	54.1	2683	2.85
ScwarzP	744.5	174.0	4.23	25.70	66.3	2899	3.51
Gyroid 2	741.4	174.0	4.23	25.73	66.2	2870	3.50
Gyroid	720.3	174.0	4.19	25.66	70.4	2881	3.76
Gyroid 1.3	716.4	174.0	4.18	25.21	65.7	2659	3.58
Diamond	697.7	174.0	4.25	25.64	78.5	3013	4.14
Solid	628.9	174.0	4.20	25.34	148.6	4635	8.02
Lidinoid	625.8	174.0	4.17	25.63	104.2	3218	5.60
Aluminum	686.0	174.0	4.21	25.57	52.7	1955	2.81

*red shading indicates values not meeting requirements

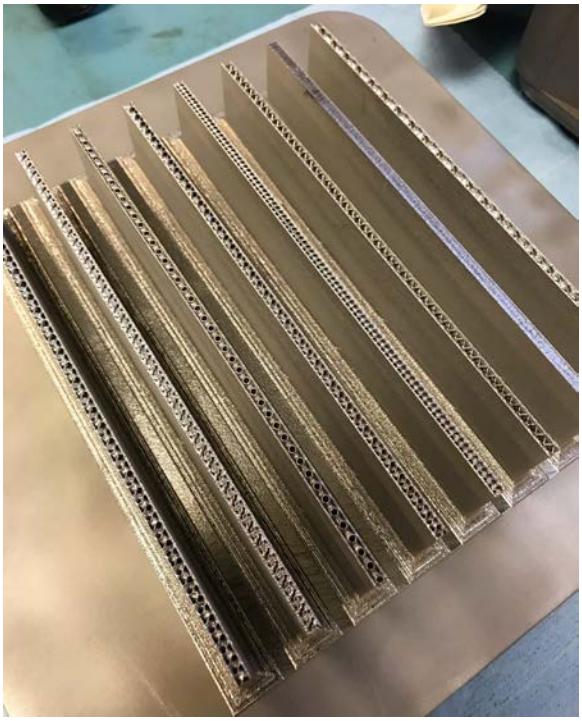

Figure 5.11. Completed Print on the Build Plate

thicker than the test build. This qualitative analysis was verified by the printed dimensions and calculating the equivalent densities, listed in Table 5.4. The equivalent

Figure 5.12. Printed Beams

densities of the TPMS based beams increased by 73-77% while the lattice increased by 104%. The densities of all the Inconel 718 metamaterials exceeded the required density established in Chapter III. It was determined that the poor quality was due to the higher temperature Inconel 718 alloy and corresponding high power required to form a continuous melt pool.

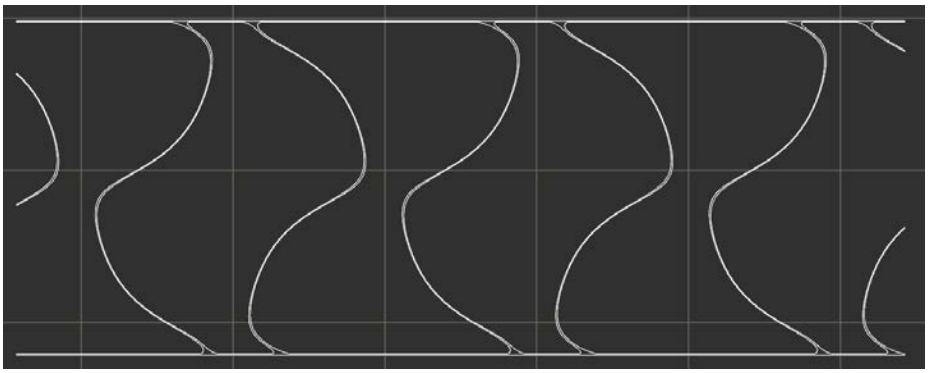

Figure 5.13. CLI Single Slice at 0.025 mm Wall Thickness

Although the densities exceeded the desired target, the results of the modal analysis provided promising results. The frequency response was measured by scanning 27 points along the beam at sufficient sampling rate to capture frequencies up to 5 kHz.

Table 5.5. PSV-400 Laser Vibrometer Acquisition Settings

Settings	Build 1	Build 2
Averages	6	6
Bandwidth	5 kHz	2 kHz
Spectral Lines	6400	1600
Sample Time	1.28 s	800 ms
Frequency Interval	781.25 mHz	1.25 Hz
Sensitivity	VD-08 1 mm/s/V	VD-08 10 mm/s/V

Table 5.5 includes further information on the acquisition settings used. The response of the scwarzP based beam shown in Figure 5.14 is representative of the responses of the beams measured. The measured frequencies listed in Table 5.4 demonstrated all the TPMS based metamaterials, except the lidinoid based beam, possessed stiffness-to-weight properties exceeding the theoretical value of a solid 7075-T6 aluminum and solid Icnonel 718 beam. The lattice beam exhibited the highest frequency, achieved by maintaining a nearly equivalent bending stiffness while shedding significantly more mass than the TPMS based beams. As expected, it was shown that increasing the periodicity of the gyroid in the length direction decreased the overall density; however the effect on frequency provided mixed results. Comparing the stiffness and mass of the metamaterials to the aluminum beam resulted in a 33.6%, 17.8%, and 16.8% increase in stiffness-to-weight ratio for the lattice, ScwarzP, and gyroid 2 beams, respectively.

It was not within the scope of this research to conduct a parameter study to determine the optimal print setting for exceptionally thin walled structures (¡ 0.5 mm). To reduce the equivalent density of the beams, the TPMS and wall/lattice thicknesses were decreased to 0.025 mm within the nTopoogy model. This approach eliminated any hatching in the CLI and collapsed the contour line so that the laser would essentially trace the same path twice. Figure 5.13 shows the same slice from Figure 5.3 under these new settings. The resulting thicknesses would be approxi-

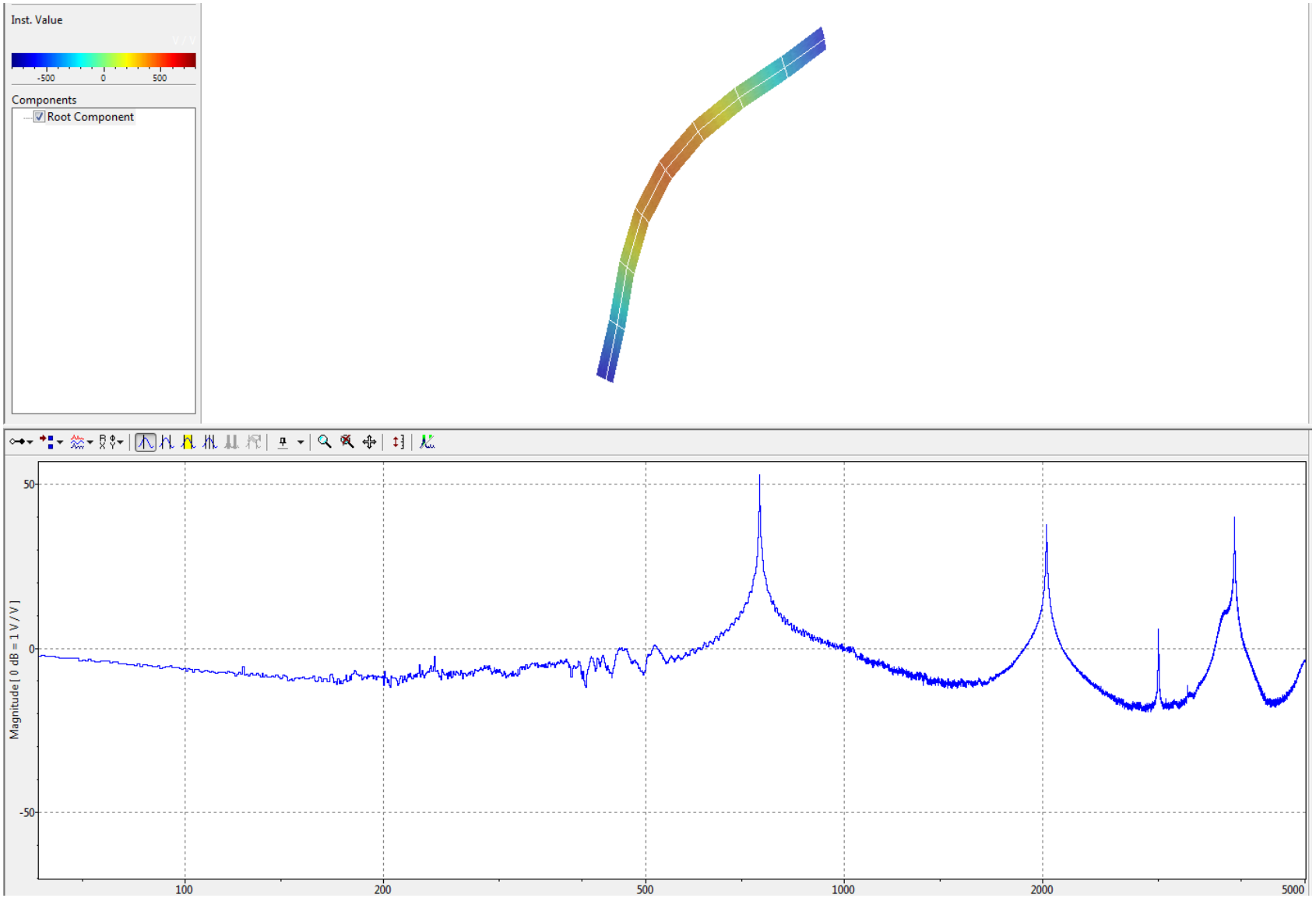

Figure 5.14. Modal Response - ScwarzP (First Mode = 744.5 Hz)

mately equivalent to the width of the laser's melt pool track, providing the thinnest walls possible.

Based off the results of the initial build a few changes were made for the second build. The lidniod based metamaterial was excluded due to its poor properties. Instead of only increasing the periodicity of the gyroid based beam in the length direction the periodicity was scaled equally in all three dimensions. By increasing the periodicity in all directions the total mass could be reduced significantly with the intent of imitating the minimalist design of the lattice beam. Additionally, sufficient Inconel 718 was available to print the second build in the intended vertical orientation.

During the second build a printer error occurred requiring the M2 to be restarted. Generally this type of error is not a concern however an alignment issue ensued causing the final 17 mm of the build to separate from one of the gyroid based beam. In lieu of printing a third build to the original 175 mm height, it was concluded that the necessary comparison data could be acquired by machining all the beams to an equivalent length of 156mm. The resulting dimensions were tabulated in Table 5.6.

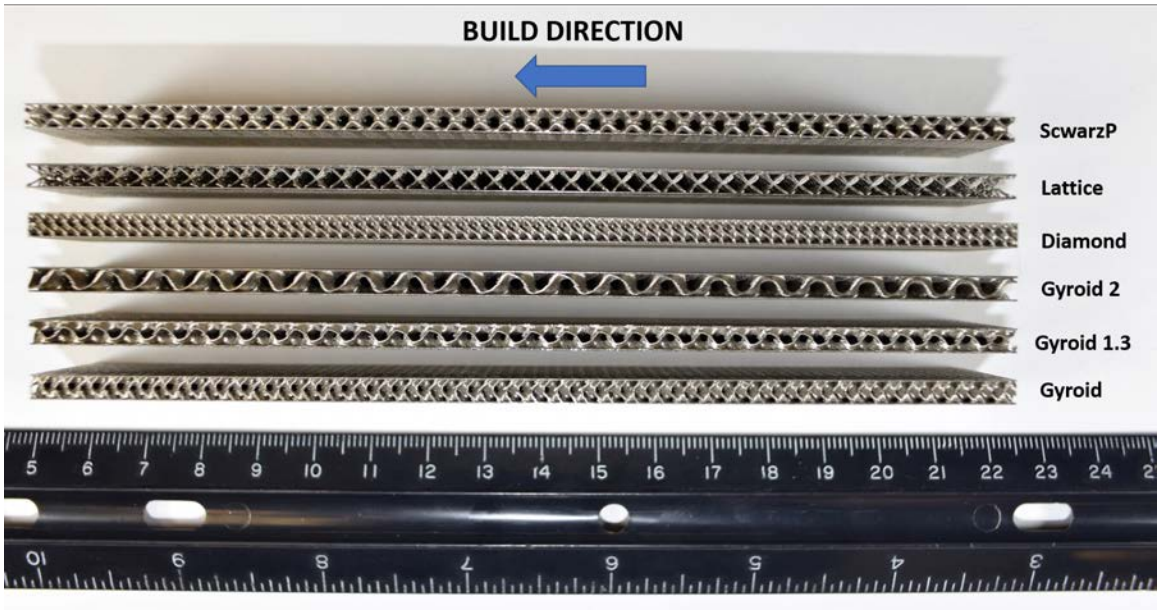

Figure 5.15. Printed Beams - Second Build

Table 5.6. Second Build Results

Beam	Natural Frequency (hz)	Length (mm)	Height (mm)	Width (mm)	Mass (g)	Stiffness (N /m)	Density (g/cc)
Lattice	970.0	156.0	4.05	25.30	18.2	1351	1.14
ScwarzP	786.3	156.0	3.99	25.33	34.7	1692	2.20
Gyroid 2	843.8	156.0	4.02	25.29	24.5	1376	1.54
Gyroid 1.3	816.3	156.0	4.02	25.24	29.5	1550	1.86
Gyroid	782.5	156.0	3.96	25.35	40.5	1956	2.59
Diamond	741.3	156.0	4.05	25.22	42.2	1829	2.65

*red shading indicates values not meeting requirements

The second build yielded significantly lighter beams with dimensions more accurately matching the "As Designed" values than initial build. Despite these improvements the standard gyroid and diamond based beams did not satisfy the equivalent density requirement. Although the mass and exterior dimensional accuracy improved, it was apparent the print quality was still inferior to the SS 316 test build, illustrated in Figure 5.15. Collapsing the contours and eliminating hatches precipitated voids at the intersections of the periodic structures where the surface was normal to the Z axis. At these intersections the distance between contours exceeds the overlap of the melt pool tracks resulting in voids. Due to the discretization of the continuous structure adding hatching or offsetting contours will not always remedy this issue. This phenomena was depicted in Figure 5.16 where the slices on the right do not coincide with the exact height of the intersection resulting in a void. Figure 5.17 illustrates why this does not occur for larger thicknesses such as 0.25 mm.

The same 27 point scan grid was captured for the second build providing a slightly improved fidelity of the mode shape in comparison to the longer beams from the first build. The frequency range was reduced to 2 kHz because only the first mode was of interest. Figure 5.19 illustrates the frequency response and mode shape for the

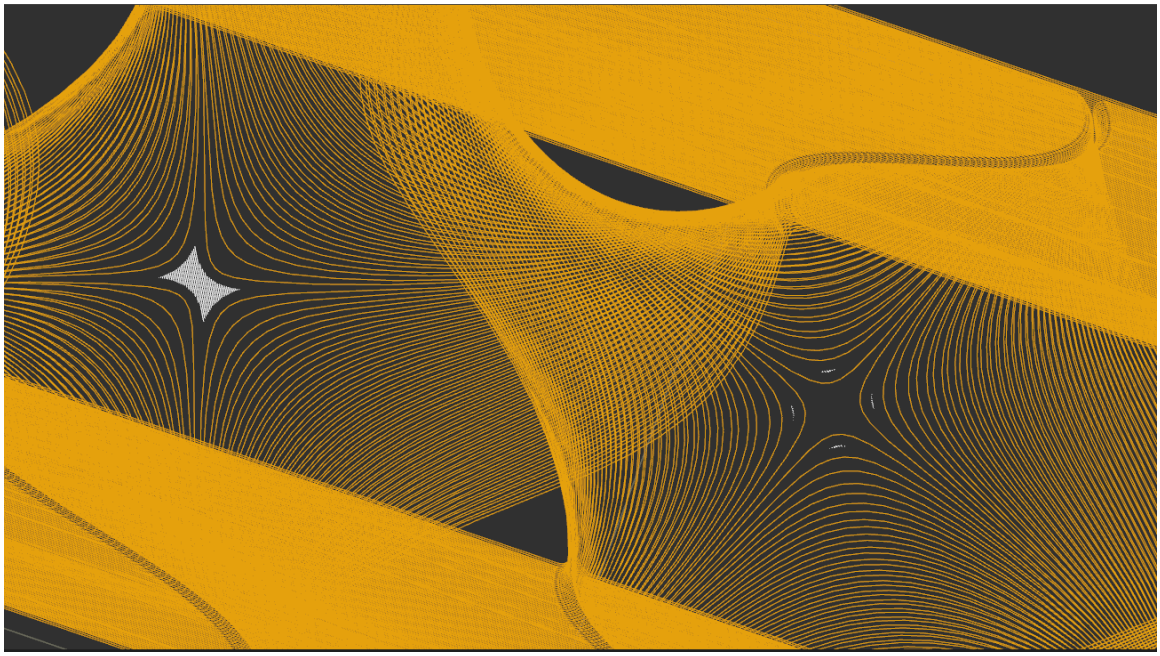

Figure 5.16. Intersection at Surfaces Normal to Z axis at 0.025 mm Thickness (Contours - Yellow; Hatching - White)

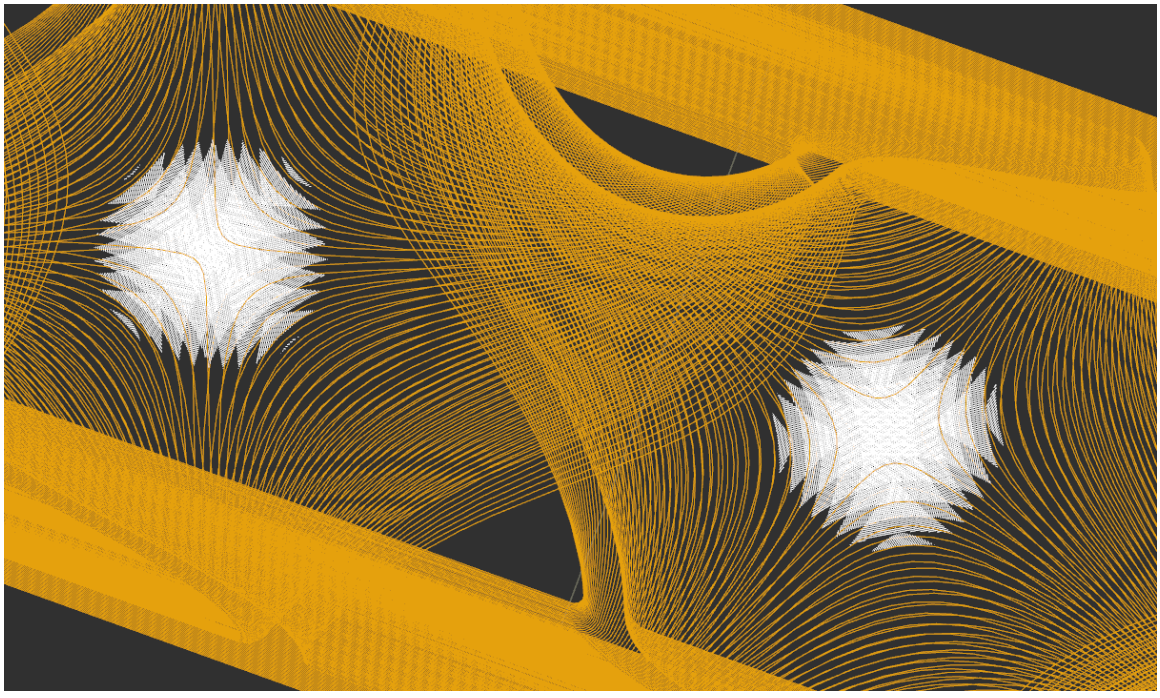

Figure 5.17. Intersection at Surfaces Normal to Z axis at 0.25 mm Thickness (Contours - Yellow; Hatching - White)

gyroid 2 beam, this response is representative of the remaining beams. As shown in Table 5.6, the lattice based beam remained the superior beam in terms of purely frequency and equivalent density. The lattice was succeeded by the gyroid 2, gyroid 1.3, and scwarzP beams respectively. Due to the reasoning discussed in Section 2.5 the lattice was only evaluated for comparison and was eliminated as a viable option going forward. Although gyroid 2 exhibited superior performance parameters it was also eliminated due to concerns that such a large periodicity could result in unsupported structure in a 4 mm x 4 mm element. This issue was evident in Figure 5.18 where a significant portion of the TPMS structure is not contacting the sidewalls. Considering beams of widths as narrow as 4 mm were incorporated in the topology design the stiffness could be severely compromised if this phenomena occurs. Based on this reasoning the metamaterial derived from gyroid 1.3 with a periodicity of 0.838 was selected as the structure to be used in the final bus structure design.

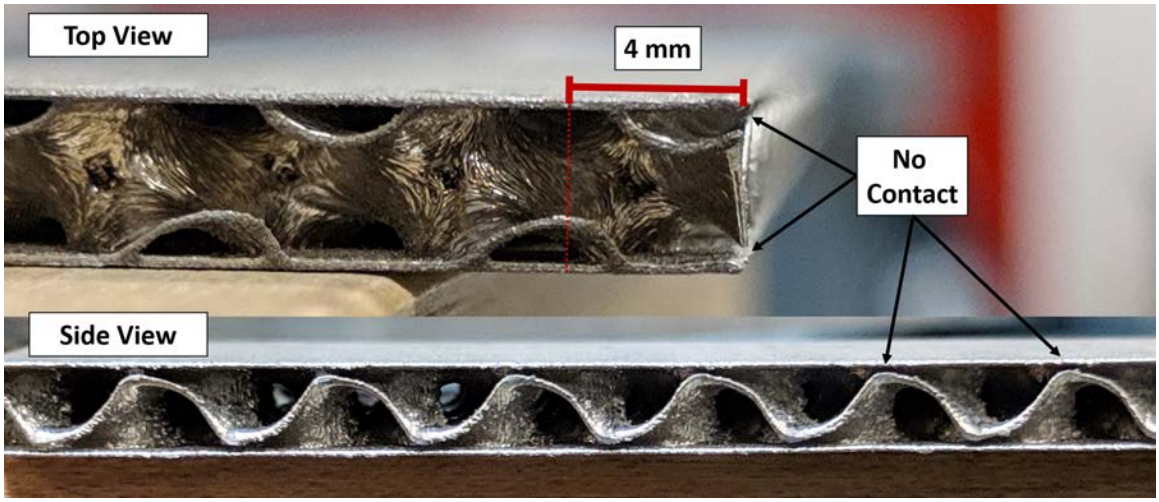

Figure 5.18. Gyroid 2 Beam

5.3.2 Finite Element Analysis

Models were created for the scwzrzP, gyroid, and gyroid 1.3 based metamaterials from the second build. The scwarzP and gyroid 1.3 were chosen because they were

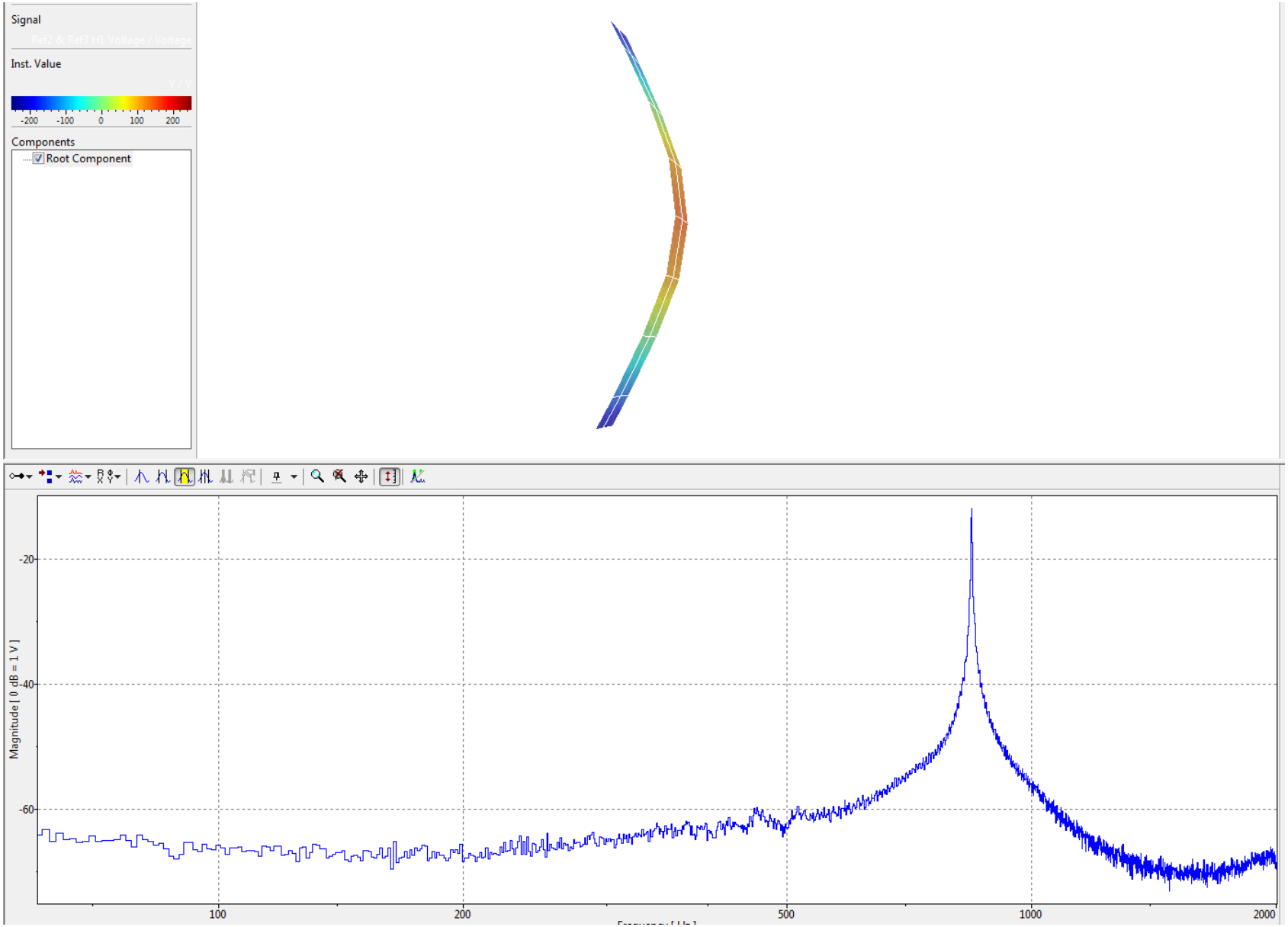

Figure 5.19. Modal Response - Gyroid 2 Build 2 (First Mode = 843.8 Hz)

Table 5.7. ScwarzP Convergence Study

Run	Element Size (mm)	Total Elements	Total Nodes	Frequency (Hz)	% Change
1	0.1	69,216	39,145	247.12	
2	0.05	130,942	72,489	236.4	-4.3%
3	***0.01***	***634,002***	***333,415***	***225.21***	-4.7%
4	0.005	1,286,371	670,470	223.61	***-0.7%***
5	0.001	2,362,285	4,660,785	222.8	-0.4%

the only two that met the density requirement and were not eliminated for qualitative considerations. Although the third gyroid beam did not meet the density requirement it was included to verify the model could accurately account variations in periodicity. A full 0.1 mm to 0.001 mm minimum element size convergence study was conducted for only the scwarzP model. The results were tabulated in Table 5.7. The third iteration met the desired convergence criteria of within 1% of the following iteration. An accelerated convergence study was conducted for the gyroid models beginning at 0.01 mm. The accelerated study verified these models achieved convergence at a 0.01 mm minimum element size as well. Figure 5.20 illustrates the resulting first mode deformation of the simulations completed for the convergence test. After verifying the TPMS structure had achieved convergence the wall convergence study was conducted next.

The results of the sidewall convergence study for the gyroid 1.3 sandwich beam were listed in Table 5.8. The convergence study indicated the initial sidewall element size of 1 mm had already met the convergence requirement. The results of the study verified that a final beam model with a 0.01 mm minimum element size TPMS S3R

Table 5.8. Sidewall Convergence Study (gyroid 1.3)

Run	Element Size (mm)	Total Elements	Total Nodes	Frequency (Hz)	% Change
1	***1***	***3,900***	***12,063***	***1006***	
2	0.5	15,912	48,463	1003.2	***-0.3%***

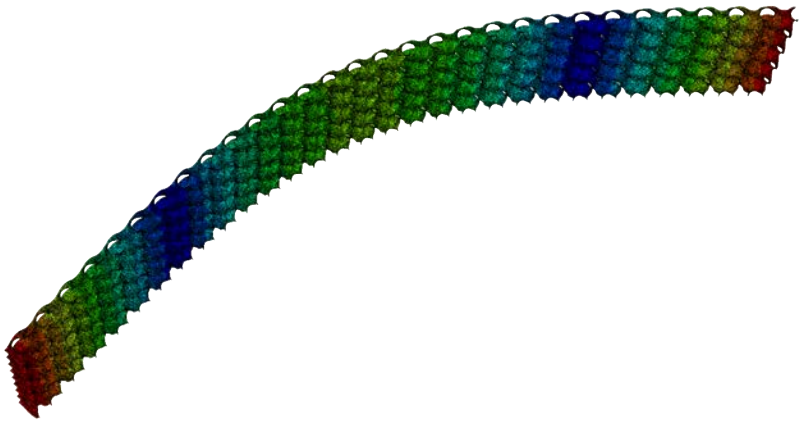

Figure 5.20. Deformed Gyroid Infill

mesh and a 1 mm sidewall element size S8R mesh met convergence requirements. Upon completion of the convergence study, model updating was conducted to refine the initial model.

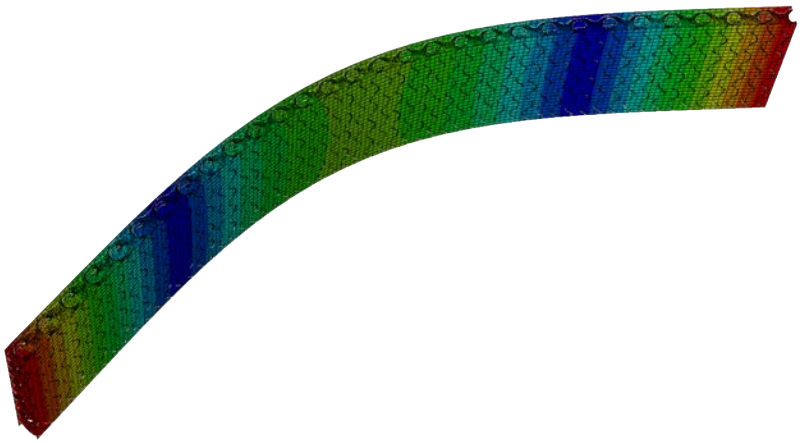

Figure 5.21. Deformed Gyroid Beam Model

An initial model was ran under ideal parameters, as shown in Table 5.9. The resulting frequency was significantly higher than the experimental value. The first update was accomplished by adjusting the material properties for Inconel 718. The density and elastic modulus of the solid beam from the experimental data were calculated to be 8.02 g/cc and 156 GPa respectively. The updated parameters reduced

the frequency of the first mode to 880.38 Hz corresponding to a 7.9% difference in relation to experimental value of 816.3 Hz. The next objective of the next update was to refine the thickness of the model to match the printed beam. The total mass of the model (33.4 g) after updating the material properties was greater than the printed beam (29.5 g). To compensate for this difference the thickness of the TPMS and sidewalls were reduced proportionally to 0.221 from 0.25, resulting in a total model mass of 29.5. Measurements of the thicknesses of the printed beam ranged from 0.20 to 0.235 therefore this value was deemed realistic and acceptable. Refining the thickness and mass of the model further decreased the frequency from 880.38 Hz to 878.69 Hz, a 7.6% difference from the experimental value.

Table 5.9. Model Updating Results (Gyroid 1.3)

Run	Wall Thickness (mm)	TPMS Thickness (mm)	Modulus of Elasticity (GPa)	Density (g/cc)	Total Mass (g)	Frequency (Hz)	% Difference
Experimental	**N/A**	**N/A**	**N/A**	**N/A**	**29.5**	**816.3**	N/A
Initial Model	0.25	0.25	208	8.19	34.1	1006	**23.2%**
Material Update	0.25	0.25	156	8.02	33.4	880.38	**7.9%**
Mass Update	0.221	0.221	156	8.02	29.5	878.69	**7.6%**
Modulus Update	0.221	0.221	134.75	8.02	29.5	816.65	**0.04%**

The final simulation conducted attempted to minimize the deviation from the experimental result by reducing the elastic modulus parameter. A modulus of 134.75 GPa was found following this process reducing the percent difference to 0.04% for the gyroid 1.3 model. Tensile tests of Inconel 718 at AFIT have measured modulus of elasticity values as low as 88 GPa therefore. Additionally, it was believed the voids identified in Section 5.3.1 would reduce the effective stiffness of the metamaterial. Based of these conclusions a modulus value of 134.75 GPa was determined to be within a reasonable range. These parameters were applied to the remaining beam models to ensure the model provided a generalized solution and was not a product of overfitting the gyroid 1.3 model.

As shown in Table 5.10, the results from the gyroid and scwarzP models validated

Table 5.10. FEA Results

TPMS	Experimental (Hz)	FEA (Hz)	% Difference
ScwarzP	786.3	792.99	0.85%
Gyroid	782.5	767.83	-1.87%
Gyroid1.3	816.3	816.6	0.04%

the assumptions made to refine the model. Although greater deviation occurred between these models than the gyroid 1.3 model the percent difference remained under 2% for all three models. Validation of this model provides a beneficial design tool to aid in the optimization of TPMS metamaterial performance characteristics. Unfortunately the model in this section was not completed before design decisions were made for the final bus structure in Chapter VI. Therefore, no additional metamaterial structures were evaluated computationally to determine the thickness and periodicity values that would provided the optimal stiffness-to-weight ratio.

5.4 Summary

This chapter covered the methodology and analysis conducted to determine the appropriate metamaterial to be used in the final bus structure design. Significant insights were ascertained through qualitative and quantitative analysis of the thin wall TPMS structures. The scope of this study was limited due to time constraints, and significant research remains in this area to fully optimize the benefits of these complex structures. Chapter VII will expand on these future research opportunities. The following chapter and final study will leverage the data and analysis discussed in the previous chapters to finalize the CubeSat design and ultimately evaluate its performance.

VI. CubeSat Bus Structure Study

6.1 Chapter Overview

The design, evaluation, and qualification of the final CubeSat bus structure will be covered in this chapter. The design portion will cover the workflow employed to integrate the results of the previous studies, CubeSat requirements, and interfaces into a functional design. Evaluation of the bus structure will be conducted based off the final mass and through laser vibrometry to determine the natural frequencies and mode shapes of the chassis. The results will be compared against two other bus structures; the aluminum lattice based chassis designed by Roberts and a commercial design by Pumpkin Inc (Figure 6.1). The final section in this chapter will cover qualification of the bus structure in accordance with the General Environmental Verification Standard (GEVS) vibration qualification guidelines.

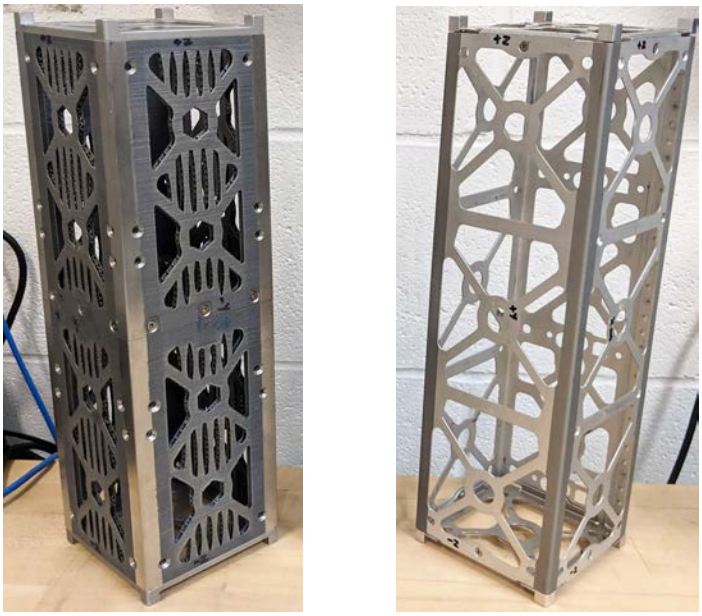

(a) Lattice Based **(b)** Pumpkin Inc.

Figure 6.1. Aluminum 3U CubeSat Chassis

6.2 Bus Structure Design

6.2.1 Bus Structure Design Methodology

The previous studies yielded critical data regarding the design, material, and metamaterial to design a lightweight high stiffness structure. Integrating these results and incorporating the necessary interfaces provided additional design challenge. Two separate models were required to complete this task. The first model represented the "As Designed" parts, capturing of the final dimensions and tolerances required for post processing. The second model consisted the "As Printed" parts required for the Additive Manufacturing (AM) process. The "As Designed" parts were modeled as solid parts in Solidworks, building off the final design from the topology study in Chapter III. The "As Printed" parts were modeled in nTopology's Turbo software enabling the incorporation of the Triply Periodic Minimal Surface (TPMS) metamaterial and capability to generate Common Layer Interface (CLI) files.

Table 6.1. List of Fasteners

Fastener Description	Interface	Quantity	Material	Vendor	Part Number
M2 x 0.4 mm x 4 mm Flat Head Screw	Male/Female Tabs	12	18-8 SS	McMaster-Carr	92010A001
M2 x 0.4 mm x 6 mm Socket Head Screw	End Plates	16	18-8 SS	McMaster-Carr	91292A831
M3 x 0.5 mm x 6 mm Flat Head Screw	Payload	24	18-8 SS	McMaster-Carr	92703A148

The "As Designed" parts integrated the X truss design (Design 4) and the male/female design interface resulting in two separate parts for each half of the chassis. In addition to these elements the interfaces for the payload stacks, tabs, and end caps were included in the model. The fasteners required for these interfaces were included in Figure 6.1. The end plates depicted in Figure 6.2 were modeled as separate parts to be fabricated from 6061-T6 aluminum. It was determined that incorporating the TPMS metamaterials would not provide a significant structural benefit due to the

orientation of the standoffs and simple geometry.

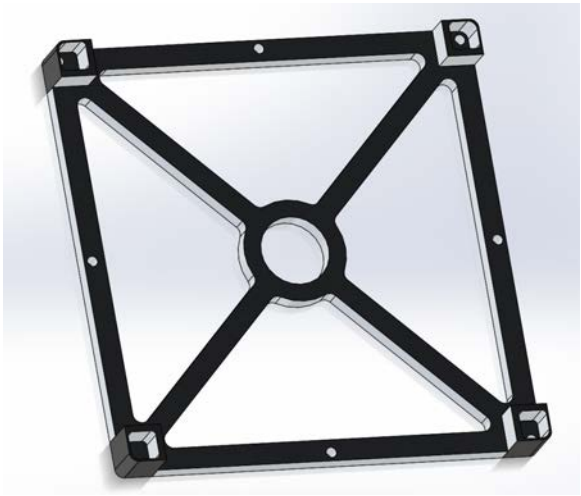

Figure 6.2. Endplate Model

The final features included in the "As Designed" parts were integrated solar panel mounts as shown in Figure 6.3. Support structure was incorporated directly on the base of the chassis to demonstrate the use of AM for multifunctional structures. Two simple support tabs were extruded from outer skin of the chassis to provide a mounting point for 3 mm solar panel hinges. Generally, these mounts are attached using additional adapter structures, increasing the complexity and total part count of the assembly. AM enables these types of structure to be integrated directly with the structure. Figure 6.4 shows the final "As Designed" parts incorporating the necessary features for a functional 3U Cubesat bus structure.

The second model was required to integrate the TPMS metamaterial into the as designed parts. Additionally, it was critical for Design for Additive Manufacturing (DfAM) principles to be accounted for in the Turbo model. Initially, a parameterized model of the TPMS metamaterial based walls were generated without the truss pattern. The sidewalls of the metamaterial sandwich structure were designed such that the centerline and thickness were explicitly defined. This allowing the thickness to be varied without altering the location of the wall; thus enabling the thickness

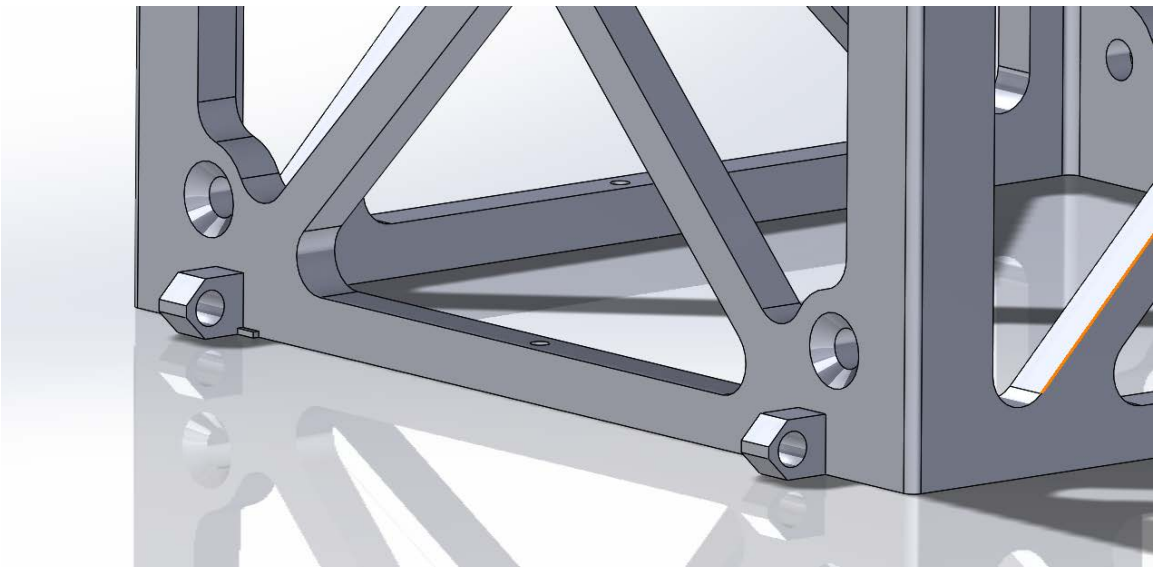

Figure 6.3. Integrated Solar Panel Mounts

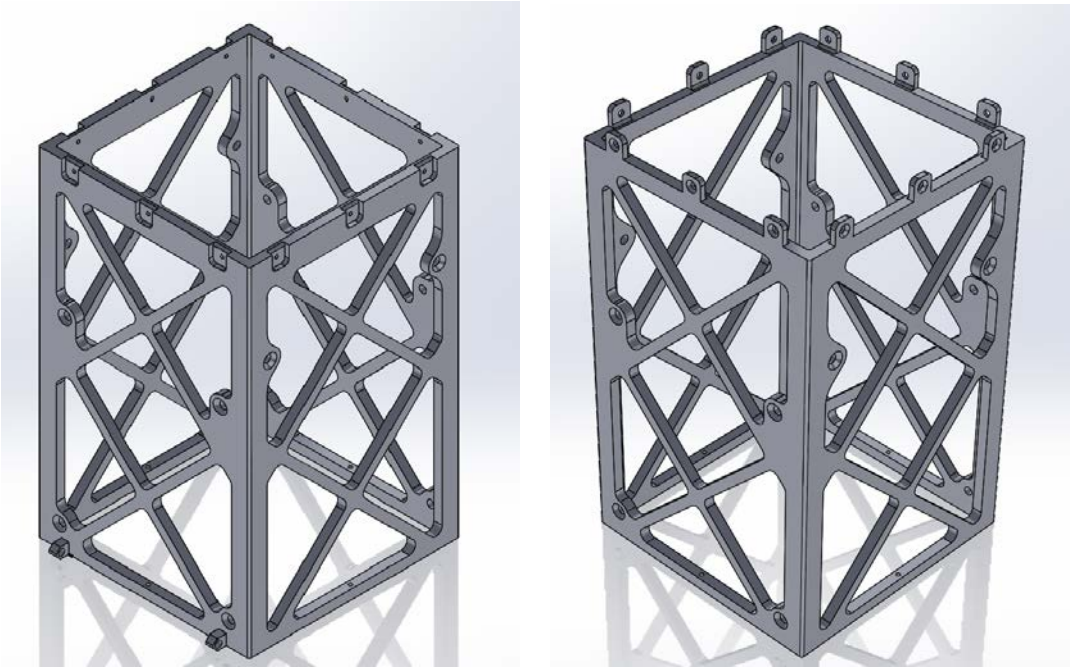

(a) Female Part **(b)** Male Part

Figure 6.4. Final "As Designed" Model

to be reduced in the model to match the print parameters in Chapter V. One of the disadvantages of a sandwich structure skin was the incorporating interfaces such as fasteners and the male/female tabs. To overcome this issue, solid structure was

added to the model at interface locations through boolean operations. Build direction was taken into account to ensure there were no overhang angles less than 45 degrees. Figure 6.5 demonstrated how these structures were included with the model.

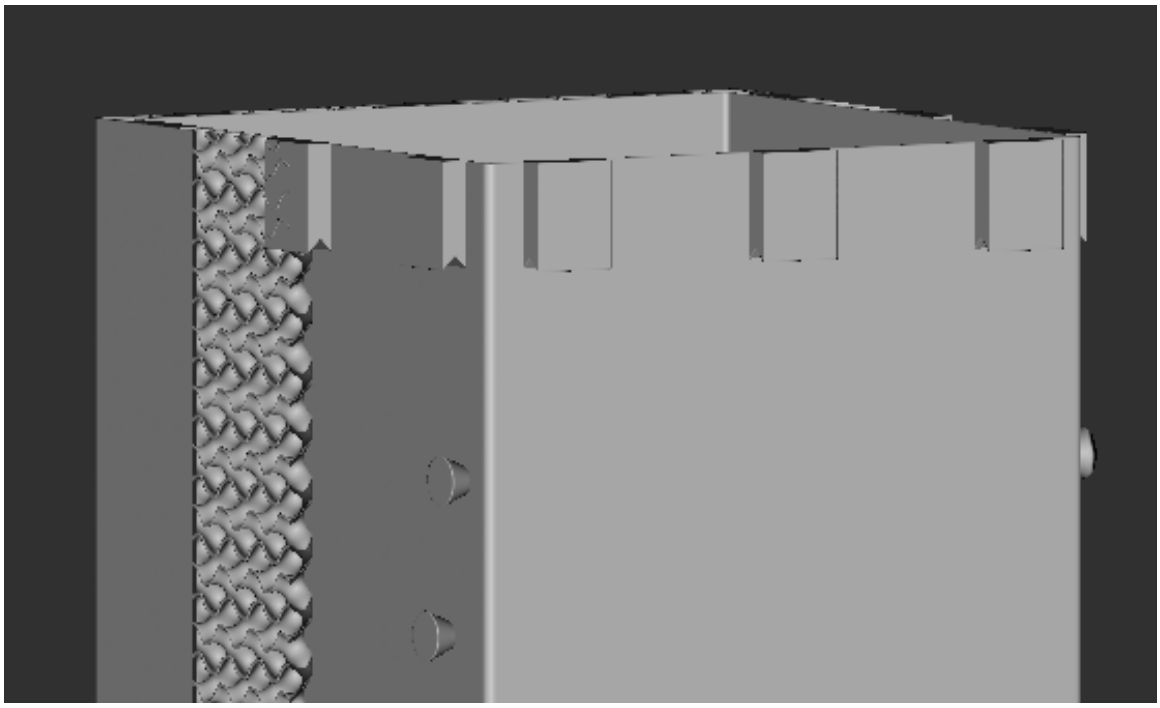

Figure 6.5. Cutaway View of Interface Bosses

There are many advantages and benefits of AM; however one of the greatest hurdles the technology has yet to overcome is the ability to produce parts that meet strict dimensional tolerances. These tolerances are essential for interfaces to ensure a precise fit between the two parts. Under these considerations the male/female tab was designed as a solid structure in the "As Printed" modeled to be post processed through traditional subtractive manufacturing methods.

To ensure the truss pattern was identical between the two models, a pattern was generated in Solidworks, extruded into a solid volume, and imported directly into Turbo. It is important to note that the pattern was modified to eliminate the overhang of the final truss segment. As seen in Figure 6.6, instead of a triangular cut out, a diamond shape was used to maintain a print angle of 45 degrees or greater. As

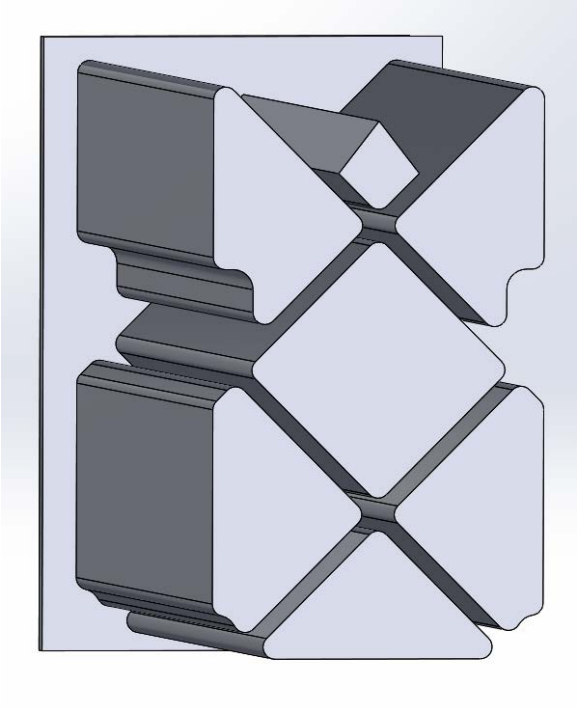

Figure 6.6. Truss Cutout Extrusion

discussed in Chapter III, the final cutout in this region would be obtained through electrical discharge machining (EDM) in post processing. Within Turbo the solid cutout was converted to an implicit, aligned, and subtracted from the Turbo model through a boolean operation. The boolean subtract operation removed any implicit volume of the original model that intersected with the truss pattern volume. This process eliminated any mismatch that may have occurred in attempting to replicate the truss pattern under the fundamentally different Computer Aided Design (CAD) environments.

A few more modifications were made to the "As Printed" model to improve the quality of the final build. One millimeter of additional material was added to the exterior of rail sections and half a millimeter was added to the interior of railing. The excess material provided margin for post processing of railings to the mandated 1.6 µm surface finish [20]. Additional material was added to the base (1 mm) and the top

(3mm) of the build as well. Finally, the entire model was scaled by 1% as a means to compensate for shrinkage that occurs after the part cools. The value of 1% was determined based of prior studies of AM parts at the Air Force Institute of Technology (AFIT). The final "As Printed" models incorporating the features discussed in this section are shown in Figure 6.7. The bus structure was printed under the same print parameters from the metamaterial study, previous listed in Table 5.3.

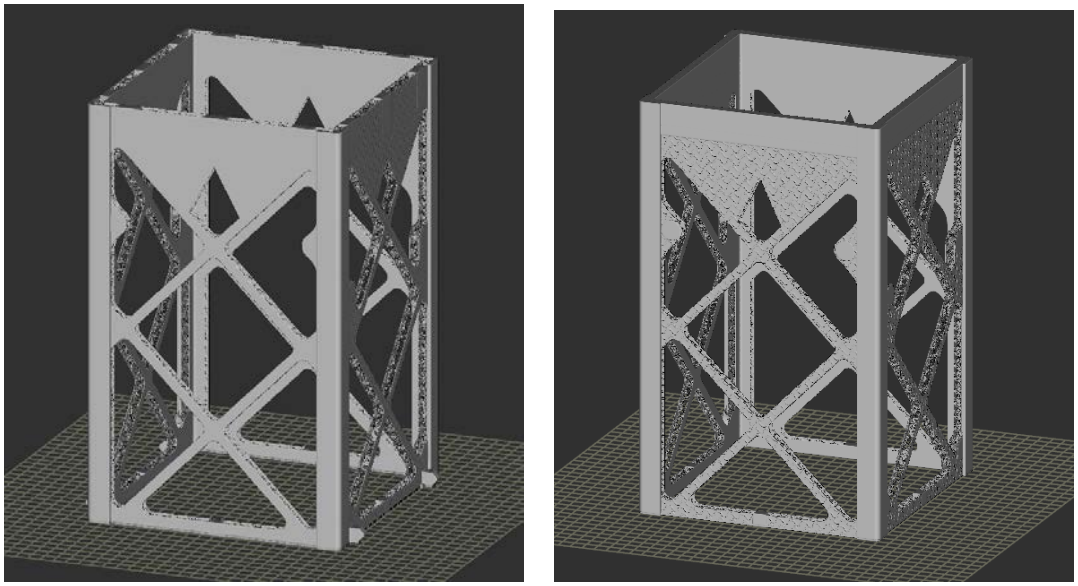

(a) Female Section **(b)** Male Section

Figure 6.7. "As Printed" Models

6.2.2 Bus Structure Design Results

Prior to printing the full structure, a partial build was conducted to verify the design choices and print quality. The first 50 millimeters of the male part was printed as shown in Figure 6.8. Measurements of the test build validated the "As Printed" dimensions and scaling required to produce a final width of 100 mm. This led to the decision to reduce the additional interior railing thickness from 0.5 mm to 0.25 mm to reduce mass before the final build. After incorporating this modification the CLI file of the final "As Printed" models were generated and loaded onto the M2.

Figure 6.8. Test Build

Both the parts were printed on a single build plate requiring approximately 36 hours to print. The printed parts before post processing can be seen in Figure 6.9. Visual inspection of the print was very promising; however measurements of skin to skin widths along the Z-axis indicated the structures were convex in shape. Micrometer measurements were taken at the locations indicated in Figure 6.10 before and after the parts were removed from the build plate. The results of these measurements were included in Table 6.2. The measurements at location 1 were within the expected outcome, meeting the 100 +- 0.3 mm Poly Picosatellite Orbital Deployer (PPOD) requirement, while the midpoint measurements at location 2 were significantly greater, resulting in widths as great as 101.32 mm after build plate removal. A common trend occurred between locations after removing the parts from the build plate. The structure expanded at locations 1 and 2 while near the base at location 3 it contracted. This was expected because at the base the structure is constrained to the build plate, preventing the structure from contracting after cooling. It should also be noted that the "on build plate" measurement at location 2 of the male part

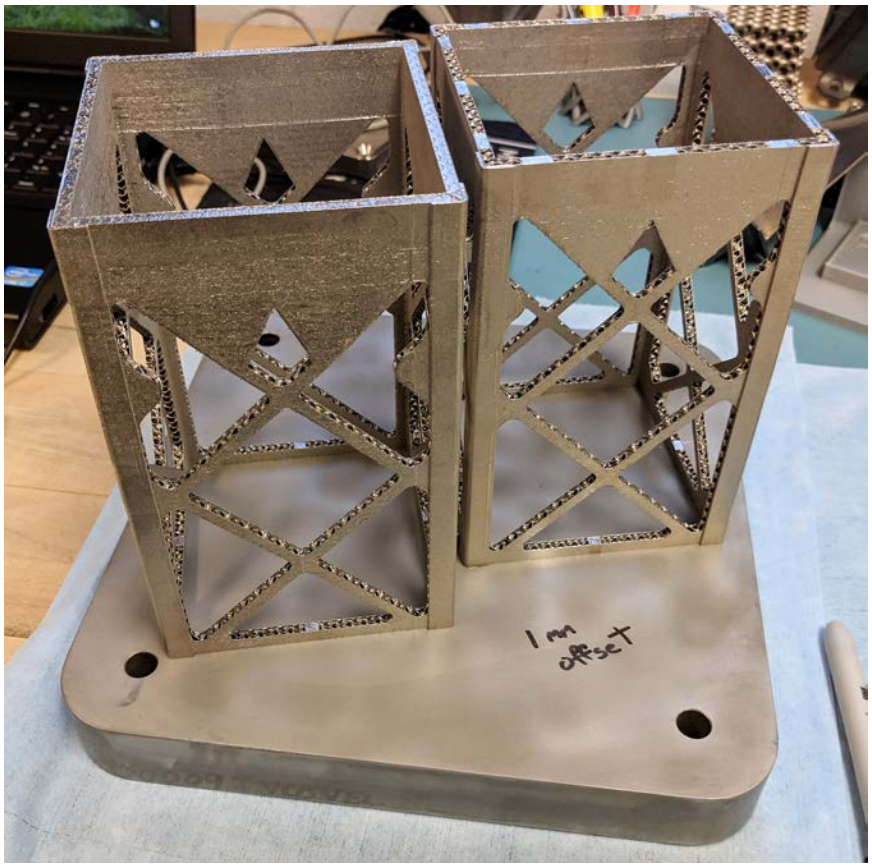

Figure 6.9. Chassis on Build Plate

may have been interpreted incorrectly as an increase of 0.81 mm was significantly larger than the increases measured at the remaining locations.

Based off of the final part measurements the print did not follow the model developed from previous builds and the expectation that the part would linearly shrink by approximately 1%. Many factors may have contributed to this discrepancy; however it is hypothesized that a main factor may have been the differences in thermal gradients during the printing process of a solid structure versus a thin wall TPMS structure. This hypothesis was supported by the measurements at location 1, which included structure with more material and solid components. At location 1, for the male part, the structure consisted entirely of solid inconel for the tabs to be machined from. The structure of the female part at location 1 was not completely solid; however

it contained a mixture of solid and TPMS structure. The completely solid section of the male part resulted in the desired dimension of 100 mm while the female measurement was slightly greater at 100.11 mm. This may also provide an explanation for how the dimensions at location two exceeded the scaled print width of 101 mm. It is possible that the middle of the structure swelled as the top shrunk and the base remained constrained. Determining the cause for these deviations require additional research and will be discussed further in Chapter VII.

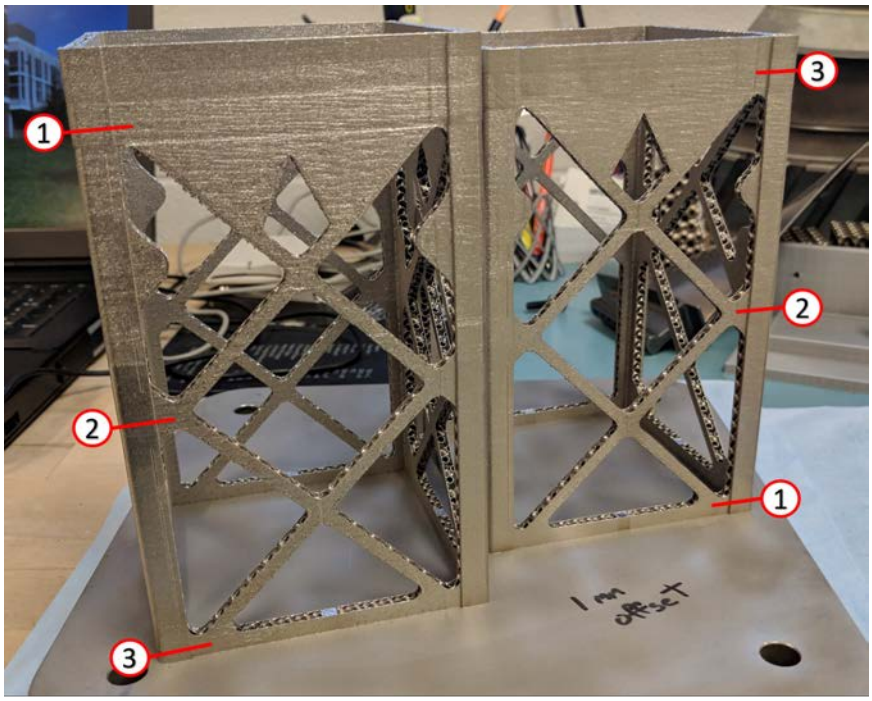

Figure 6.10. Width Measurement Locations

Table 6.2. Width Measurements

Female		
Location	On Build Plate (mm)	Off Build Plate (mm)
1	99.95	100.11
2	100.71	100.84
3	100.43	100.08

Male		
Location	On Build Plate (mm)	Off Build Plate (mm)
1	99.82	100.00
2	100.51	101.32
3	100.58	100.33

The convex shape of the parts posed a significant challenge for post processing. Machining the 8.5 mm rails to meet the 100 mm requirement would remove the

entire outer skin at the rail skin interface. Additionally, after reducing the additional interior railing thickness to 0.25 mm from 0.5mm there was insufficient thickness to machine down the railings. Due to limited resources and schedule constraints it was not possible to reprint the parts. The decision was made to measure the physical dimensions of the PPOD to determine the absolute allowable dimensions constraining the CubeSat's rail dimensions. The minimum rail width was measured to be 6.75 mm and the maximum allowable rail to rail width was 3.967" (100.7 mm). Based off these values, the rail width was reduced to 7 mm, followed by a 45 deg transition to ensure a transition from the railing to the outer skin. A drawing of this design has been included in Figure 6.11 for reference. The nominal width was chosen to be 3.962" (100.64 mm) to account for a 0.005" machining tolerance, an expected max value of 3.967" (100.76 mm) and minimum value of 3.957" (100.51 mm). This value ensured the final assembly would fit in the PPOD while maximizing the wall thickness of the railing.

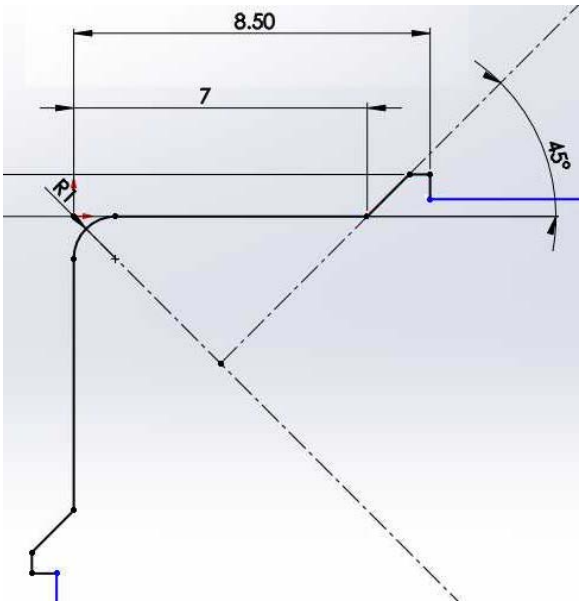

Figure 6.11. Rail Design Modification

Despite the efforts to maximize the remaining rail material, the end mill broke

Figure 6.12. Rail Breakthrough

through one of the eight half rails as shown in Figure 6.12. The other seven half rails remained intact; however it was visually apparent that the remaining thickness was well below the desired 0.25 mm. Although this would degrade structural integrity of bus structure, it was determined that the impact would be minimal to the overall stiffness of the bus. The primary purpose of the rails were to provide an interface with the PPOD rails. The overall bus stiffness is driven by the truss elements. The main concern of these flaws was the ability to withstand the GEVS qualification testing. The thin walls would be particularly susceptible to cracking under significant vibrational loading. The remaining post processing was successfully completed, yielding the final "As Designed" parts depicted in Figure 6.13.

The final bus structure was assembled from the male part, female part, and two end plates. Solar Panels were attached to demonstrate the successful integration of the solar panel mounts to the structure (Figure 6.14) eliminating the need for additional support structure and hardware. The total mass of the bus structure (no solar panels), including fasteners, was measured at 480 grams, meeting the upper bound of the requirements for a mass efficient space structure discussed in Section 3.3. In comparison to Roberts' lattice based aluminum chassis (934 g) this represented

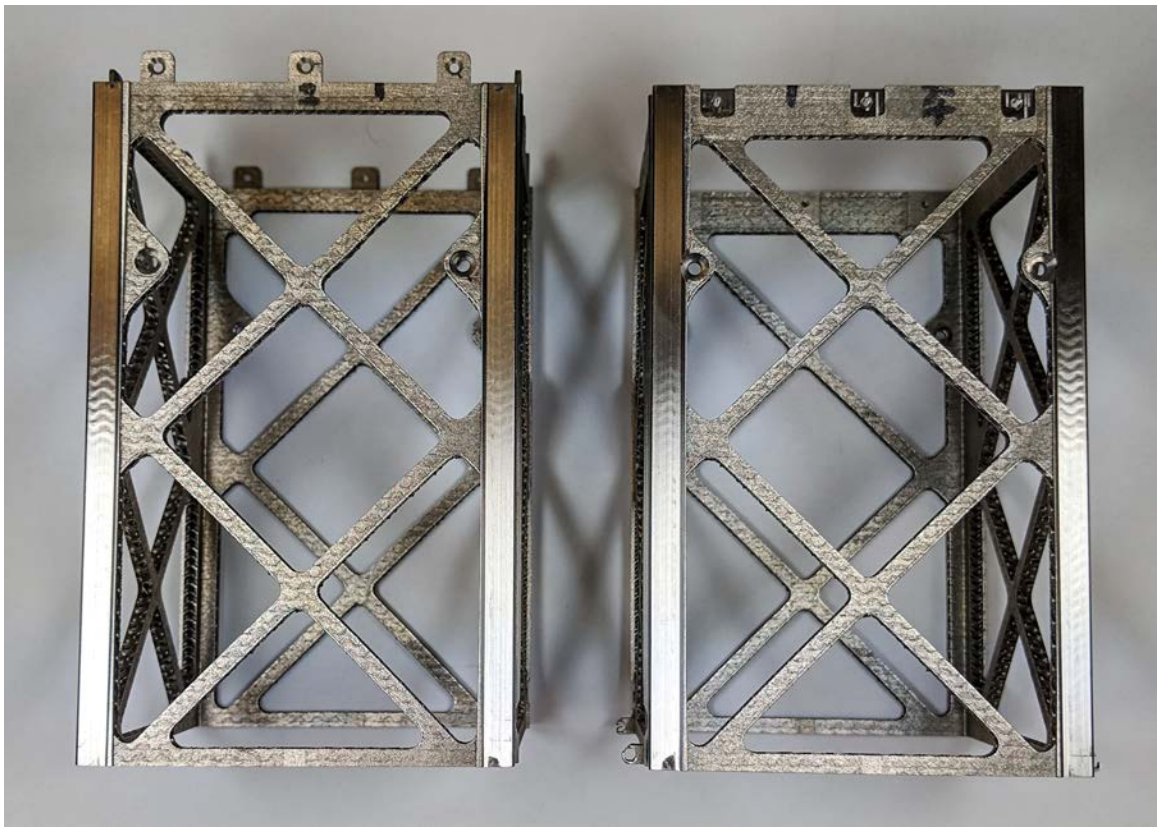

(a) Side View

(b) Top View

Figure 6.13. "As Designed" Parts

a 48.6% reduction in mass, a considerable accomplishment considering the density of inconel is over three times greater than aluminum. However, the inconcel chassis was nearly twice the mass of Pumpkin Inc's skeletonized chassis (252 g). In the next section modal analysis will be conducted on each chassis to evaluate stiffness to weight of each chassis.

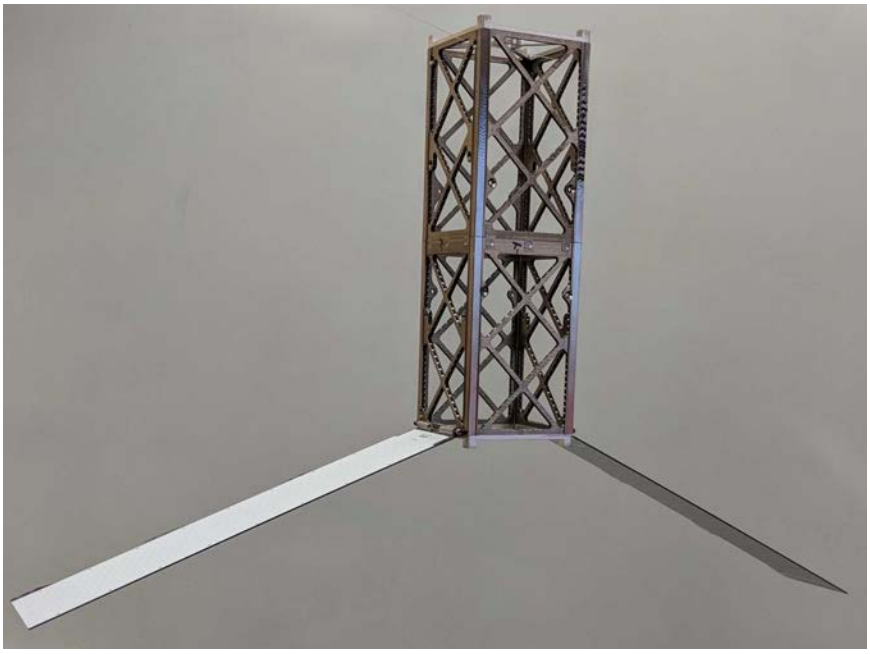

Figure 6.14. CubeSat with Solar Panel Attached

6.3 Modal Analysis

6.3.1 Modal Analysis Methodology

Based off the same principles as discussed in Chapter V, the stiffness to weight ratio of the bus structure was evaluated through modal analysis. The chassis was evaluated against the aluminum lattice based chassis from Roberts' research and a commercial design available from Pumpkin Inc. All three chassis were evaluated empty and the TPMS chassis and lattice chassis were also evaluated with three 1-kg mass stacks. The mass stacks were used to represent the additional mass of a

potential payload. The maximum mass permitted for a 3U CubeSat was 4 kg per the CubeSat specifications requirements [20], thus three kilograms was the maximum mass that could be added to the aluminum chassis under a worst case scenario. Although additional mass could have been added to the inconel chassis to achieve 4 kg, maintaining the same "payload" masses enabled a consistent evaluation between the two bus structures. As established in Section 2.3.2, the threshold for the first fundamental frequency is greater than 70 Hz. A separate modal analysis was conducted independent of the GEVS qualification test for two reasons. With the chassis integrated with the PPOD it is impossible to decouple the response of the bus structure from the PPOD/bus system. Laser vibrometry provides a higher fidelity response and the ability to visualize the mode shapes that are being excited.

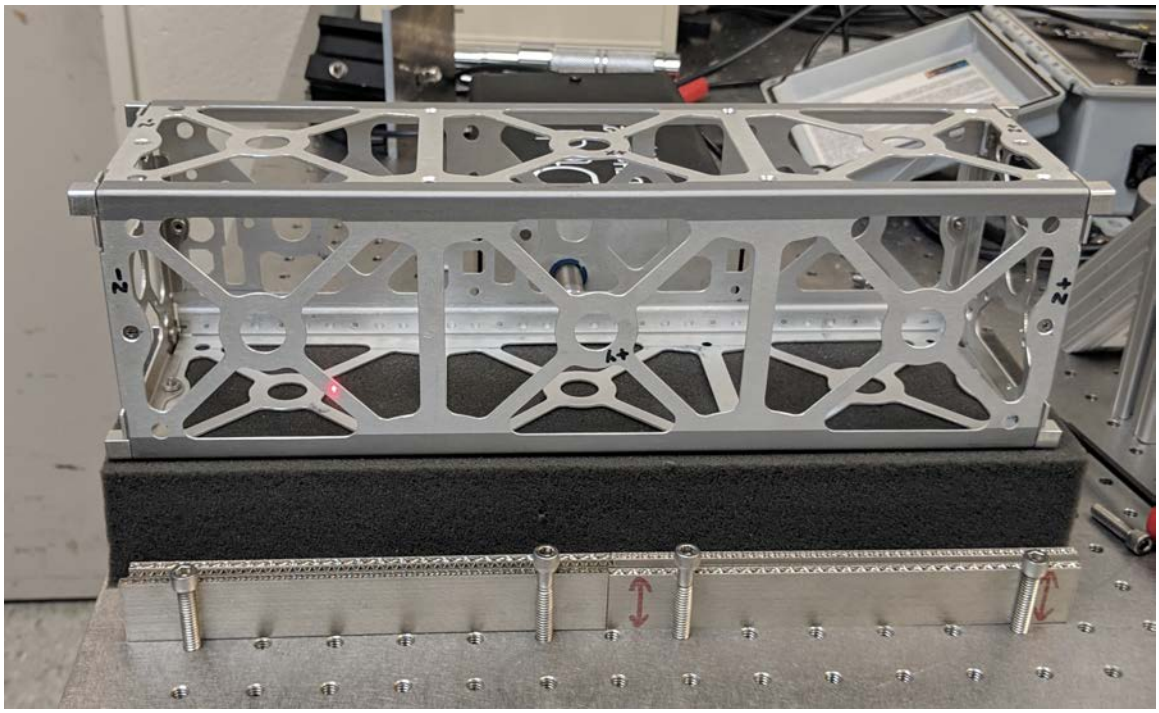

Figure 6.15. Foam Support (Pumpkin Skeletonized Chassis)

A quasi free-free boundary condition was employed for this modal analysis. Instead of hanging the chassis from a nylon cord as was done in Section 5.2.2, the chassis was placed on a soft foam support (Figure 6.15). The foam provided enough rigidity

to support the mass of the various bus structures with and without mass stacks while allowing displacement in each degree of freedom. It was believed the foam support significantly increased the damping of the system; however the impact on the natural frequency of the bus structure would be negligible.

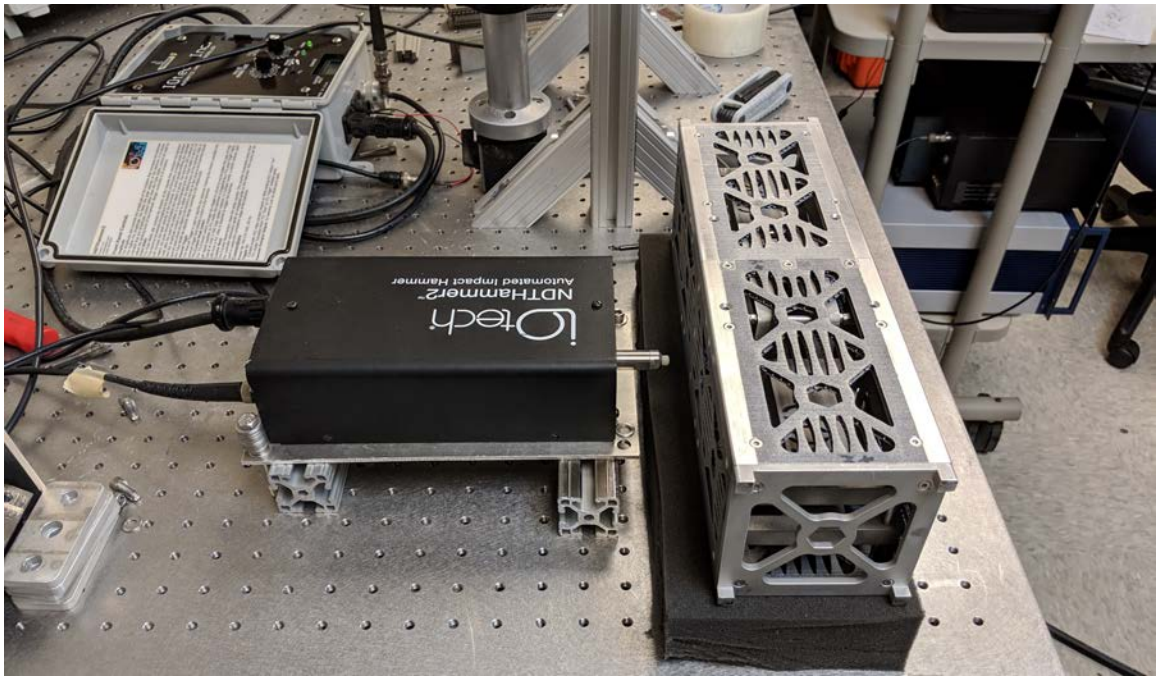

Figure 6.16. Auto Hammer Setup showing Foam Support and Hammer Impact Location

The bus structures were considerably larger and more massive than the beams tested in the metamaterial study requiring a greater input excitation than provided by the air horn used in Section 5.2.2. Therefore, an auto hammer was used in this setup as illustrated in Figure 6.16. The auto hammer was triggered by signal generator outputting a square wave at a set frequency: 1 Hz for empty chassis, 2 Hz for chassis including paylaod mass stacks. The set frequency ensured the intervals were sufficient for the chassis to return to rest in between impacts as well as complete the required acquisition period.

Under this setup, the Polytec spectrum analyzer was triggered by a 5% rising voltage signal from the impact hammer. The frequency response of the bus structure

was calculated from the auto hammer's impact pulse and the velocity data from PSV-400 laser vibrometer. A force window was applied to the impact signal to reduce noise that may have occurred after striking the chassis, while an exponential window was applied to the laser vibrometer data. The acquisition parameters varied between runs and is included with the results data. The scan grid necessarily were varied between runs as well. Figure 6.17 provides a representative example of what was applied.

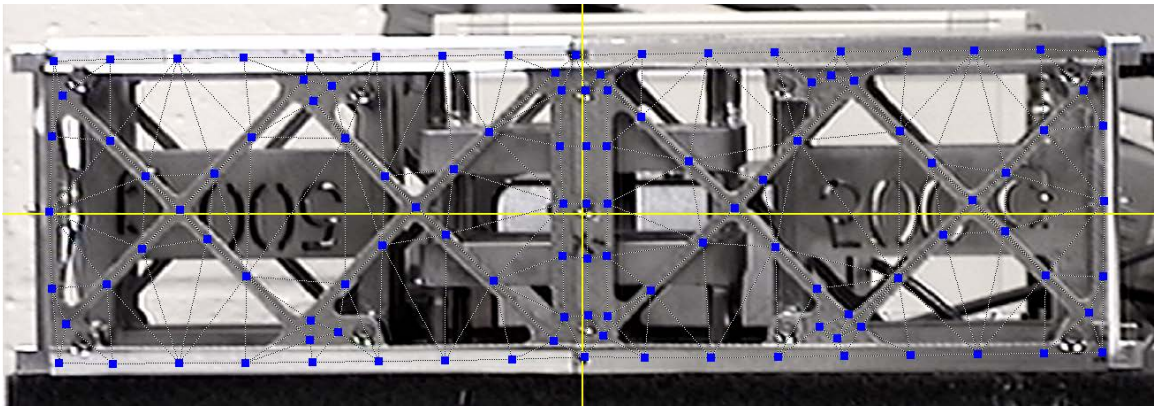

Figure 6.17. Chassis Scan Grid (blue points indicating where measurements were recorded)

6.3.2 Modal Analysis Results

In this section the results of the modal analysis of the three bus structurees will be discussed. The laser vibrometer acquisitions settings for the different bus configurations are shown in Table 6.3. A longer sampling time was necessary for the mass stack configurations. Due to the additional mass, the settling time of the system increased, a result of the soft foam support. The bandwidth was set to 4 kHz, however the frequency limits of the frequency response plots displayed in this section were set from 200-2000 Hz. The displayed frequencies were limited to narrow the scope to the region of interest.

The Pumpkin Inc. chassis is comprised of an asymmetrical design. Therefore, the frequency response of each axis varied. The results from the axis with the lowest

Table 6.3. Chassis PSV-400 Laser Vibrometer Acquisitions Settings

Settings	Empty Chassis	Chassis w/ Mass Stacks
Averages	3	3
Bandwidth	4 kHz	4 kHz
Spectral Lines	3200	6400
Sample Time	800 ms	1.6 s
Frequency Interval	1.25 Hz	625 mHz
Sensitivity	VD-08 10 mm/s/V	VD-08 20 mm/s/V

frequency are shown in Figure 6.18. The frequency of the first mode was measured at 441.3 Hz. The corresponding mode shape for this frequency was out of plane deflection of the center truss element. This mode shape was expected due to minimal thickness of the aluminum truss members.

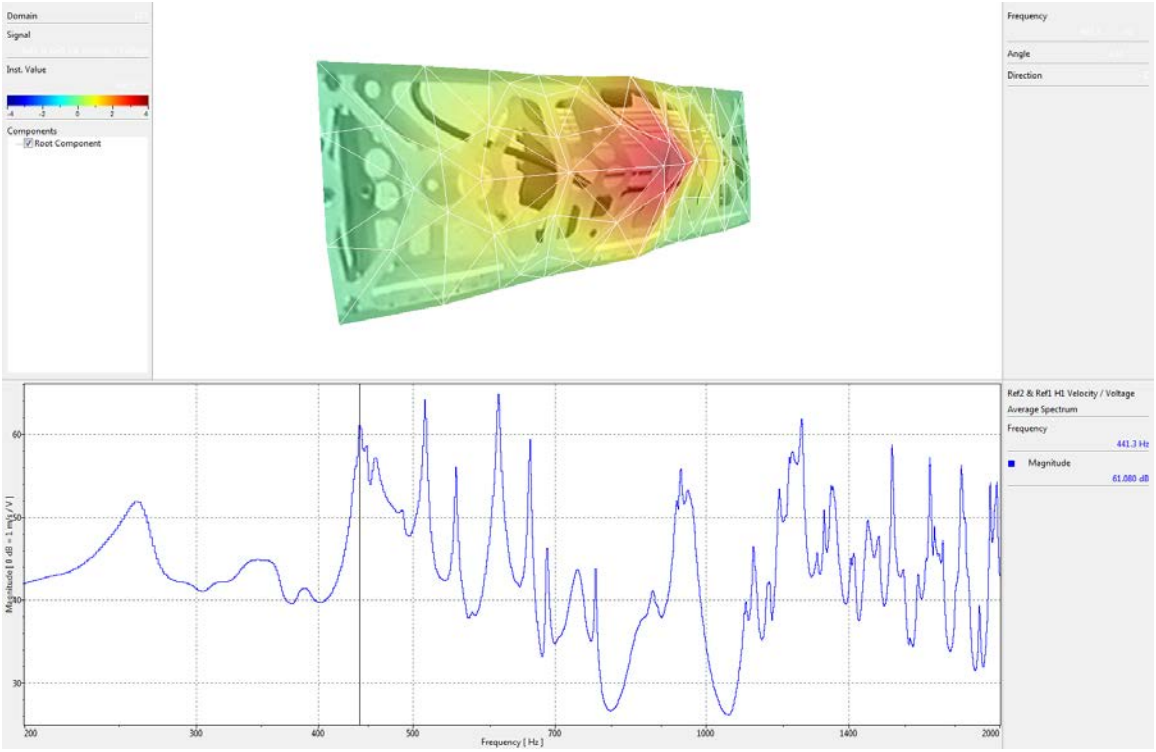

Figure 6.18. Modal Analysis of Pumpkin Inc. Skeletonized Chassis (Empty)

Roberts' lattice based aluminum chassis was comprised of a symmetrical design. Due to symmetry the frequency and mode shape were independent of the axis mea-

sured. The results of the modal analysis are shown in Figure 6.19. The frequency of the first mode was 875.6 Hz. Unlike the Pumpkin Inc. chassis, the first fundamental mode shape was a 'full body' (global) mode rather than a mode corresponding to individual truss elements. The 4 mm thickness of the truss elements and the additional support structure contributed to this difference.

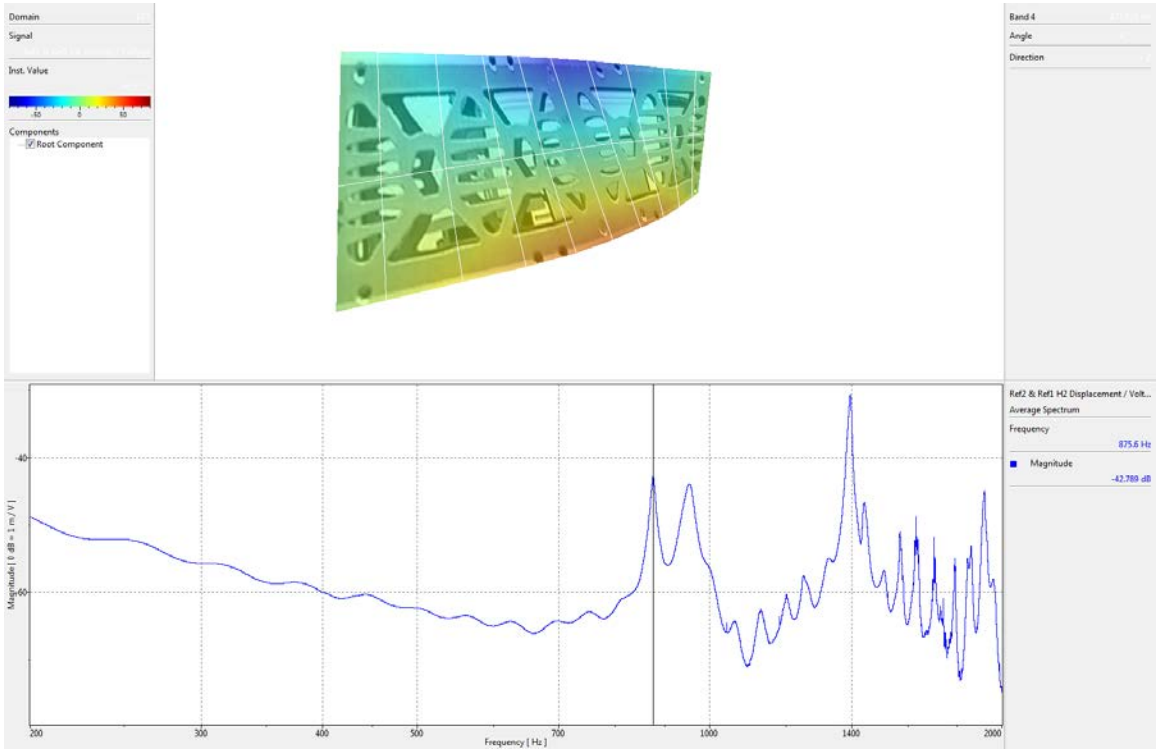

Figure 6.19. Modal Analysis of Lattice Based Aluminum Chassis (Empty)

The inconel chassis design was technically asymmetric. However, the variations between the X-axis and Y-axis were due minor changes to accommodate the different orientations of the mass stacks. These major structural support elements were consistent throughout the design. It was found that the frequency responses of each axis were equivalent within the interested frequency range. Therefore, only the results from the X-axis were included as seen in Figure 6.20. The frequency of the first mode was measured at 698.8 Hz. The corresponding mode shape was similar to the modes shape observed from the aluminum chassis. Although the quantity of truss elements

were reduced, the elements were sufficiently stiff to drive this frequency higher than the observed global mode shape.

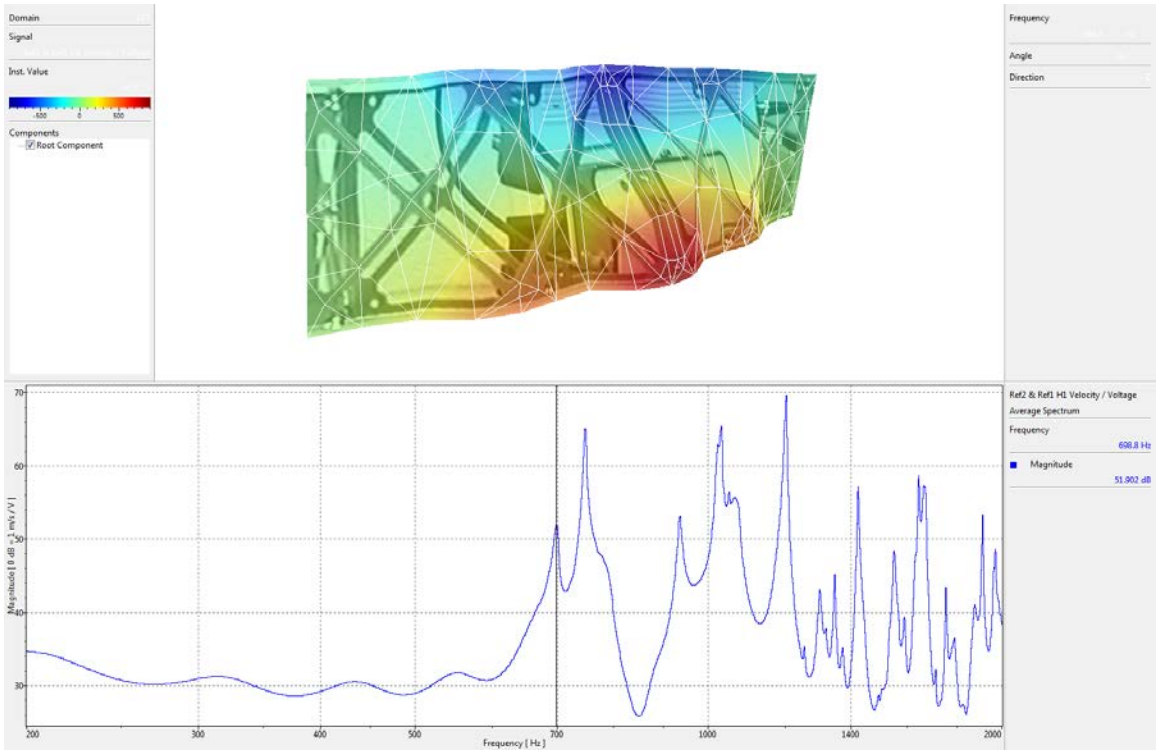

Figure 6.20. Modal Analysis of Inconel Chassis (Empty)

Figure 6.21 provides the results after inclusion of the three mass stacks. Two of the mass stacks were installed in alignment with the X-axis and the third mass stack was installed in line with the Y-axis. Although the structure was symmetric, the non-symmetric loading resulted in different responses between to the two axis. The X-axis resulted in a lower frequency of 463.75 Hz. The mode shape consisted of first bend of the entire structure. This mode shape was consistent between the two axes.

The final analysis was conducted on the inconel chassis with the three mass stacks. The mass stacks were installed in the same configuration as the lattice based chassis. Similarly, the lower frequency was found to be in the X-axis for this configuration. The frequency of the first mode was measured to be 446.4 Hz. Consistent with the lattice chassis, the corresponding mode shape was also the first bend for both axes.

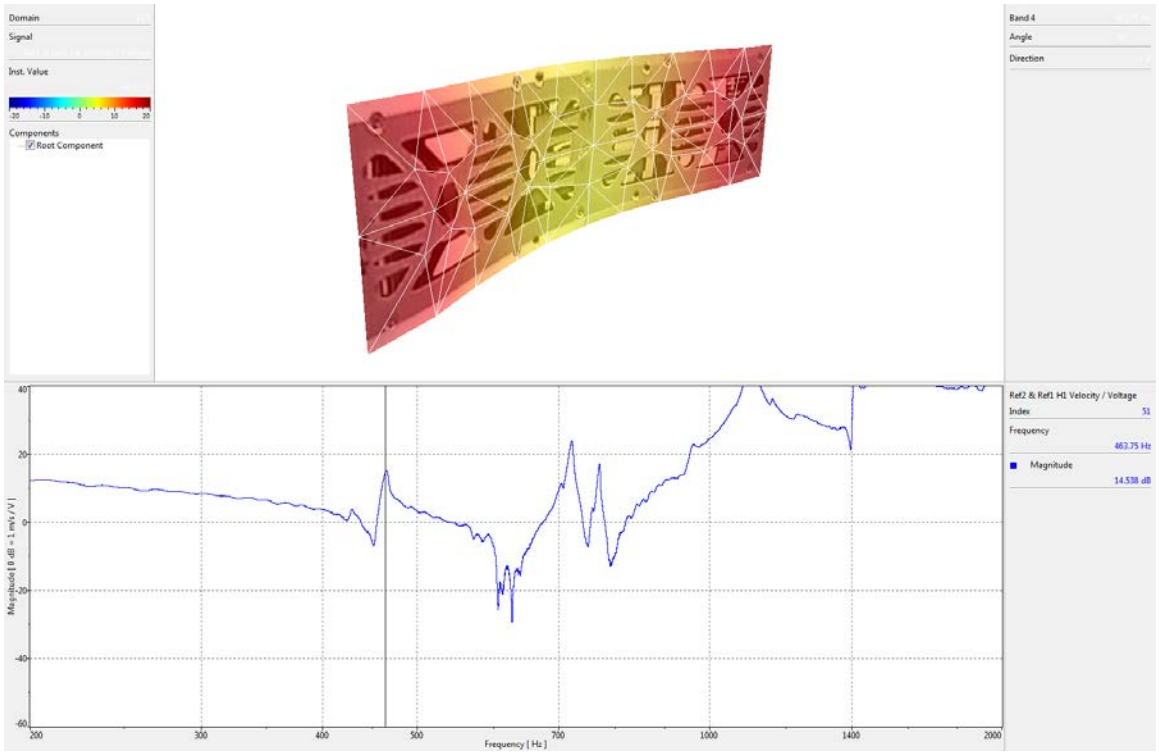

Figure 6.21. Modal Analysis of Lattice Based Aluminum Chassis (Mass)

The final results and masses of each test configuration was tabulated in Table 6.4. The lattice based aluminum chassis demonstrated the highest first mode frequency for both the empty and mass stack configurations. Despite the lower mass of the pumpkin chassis, the frequency was the lowest. The low frequency was driven by the thin structure of the truss elements. However, it is important to note that the frequency of the reported mode shape was well over 70 Hz and would not be significantly affected by the additional mass of an integrated payload. The inconel TPMS based chassis designed in this research was lower than the aluminum chassis, but not by a large margin. Focusing on the more relevant mass stack configuration, the frequency of the lattice based aluminum chassis was only 3.89% greater than the inconel chassis. More importantly, both frequencies were well above 70 Hz. Although the inconel did not demonstrate the highest stiffness-to-weight ratio as determined from natural frequency, it still exceeded performance expectations predicted by the

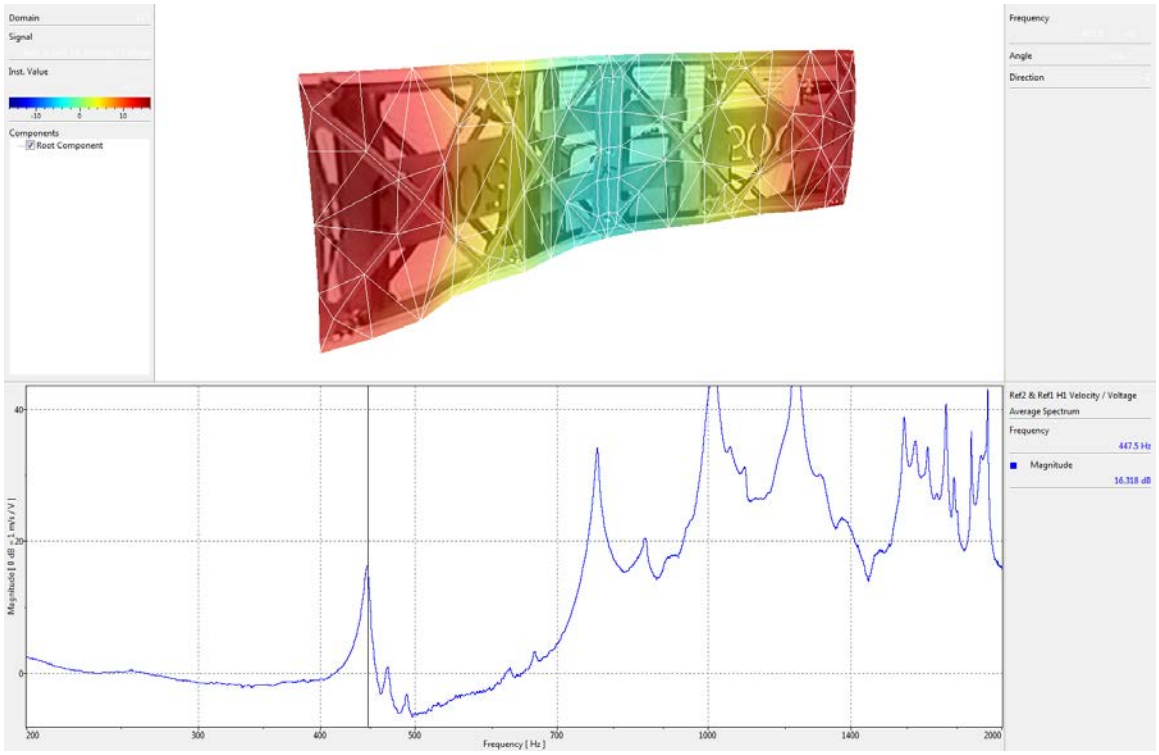

Figure 6.22. Modal Analysis of Inconel Chassis (Mass)

analysis. This study verified the stiffness performance of a lightweight mass efficient structure produced from high density, small melt pool track width material.

As discussed in previous sections, the final design was constrained due to equipment and resource limitations at AFIT. Fabricating the main body of the chassis in one section would further increase the stiffness of the structure and eliminate considerable mass required for the interface of the male/female tabs. The solid structure of these tabs had greater impact on the inconel chassis due to the higher material density. Further research should be conducted to evaluate the performance of a structure designed without these limitations.

Table 6.4. Modal Analysis Results

Chassis	Total Mass (g)	Frequency (Hz)
Pumpkin	252	441.3
Aluminum - Lattice	934	875.6
Inconel - TPMS	480	698.8
Aluminum - Lattice (w/ Mass Stacks)	4083	463.75
Inconel - TPMS (w/ Mass Stacks)	3634	446.4

6.4 GEVS Qualification Test

6.4.1 GEVS Qualification Test Methodology

The GEVS qualification test was conducted to determine if the bus structure could meet the requirements of a flight rated CubeSat bus. This was based on whether the coupled PPOD/bus system maintained a natural frequency above 70 Hz and to verify the bus structure could physically withstand vibrational loads of the launch environment. The goal of this test was to best replicate the process required for a flight rated CubeSat. Under these considerations the bus structure was tested with the three 1-kg mass stacks installed to replicate expected payload mass and provide a more realistic test environment.

Fasteners on space systems are required to have at least two independent locking mechanisms. To meet this requirement, the fasteners were torqued as well as head staked using a two-part epoxy. The M3 fasteners were torqued to 8 in-lb using a calibrated torque screwdriver. This value was based off of a previous study conducted at AFIT for which it was determined that torque values of 6 to 10 in-lb provided sufficient clamping force for M3 fasteners under GEVS vibration loads for a 6U chassis [77]. The AFIT fastener torque study was only conducted for M3 fasteners therefore the M2 fasteners were set to 4 in-lb based off recommendations from previous vibration tests. After torquing and staking each fastener, a torque stripe was applied to each

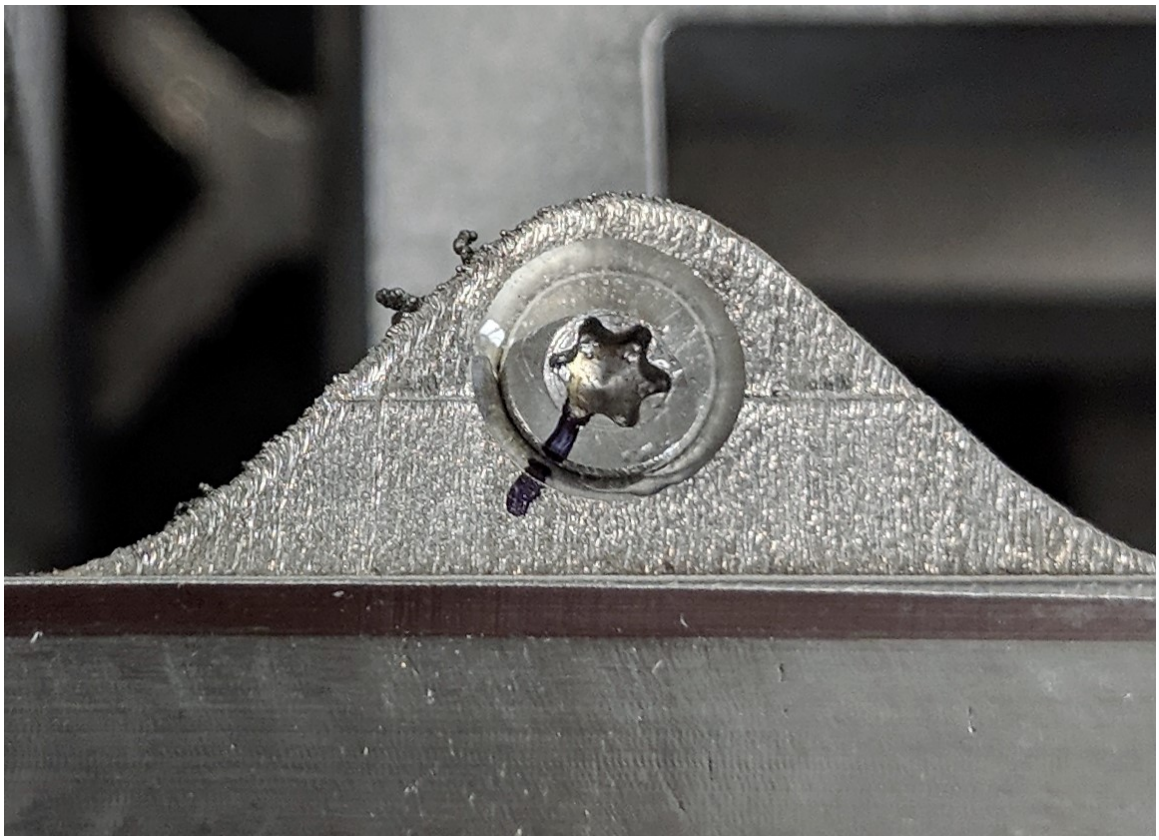

Figure 6.23. Staked Fastener with Torque Stripe

fastener head with a felt tipped marker. If a fastener rotates during testing the straight line drawn will be broken, providing a visual indication that the fastener may have came loose. Figure 6.23 provides an example of a staked fastener with a torque stripe applied. Additionally, Figure 6.23 illustrates the effect of print direction and overhangs on print quality. The part was printed from left to right in the figure. To the left of the fastener, the edge of the structure has a rough finish and two sections of the TPMS infill extended past the boundary of the walls. These sections were a byproduct of the melting deeper than the current layer, melting additional powder particles below the unsupported structure.

The CubeSat bus structure was integrated into a 3U TestPOD in accordance with integration procedure of the 3U TestPOD User's Guide. A TestPOD is a modified PPOD designed specifically by Cal Poly for qualification testing. For simplicity,

the TestPOD will be referred to as a PPOD in this thesis. The first step of the integration process required an acceptance check of bus structure. The 3U CubeSat Acceptance Checklist was included in Appendix C. As expected, the bus did not pass the acceptance checklist due to the manufacturing issues discussed in Section 6.2.2. The remaining steps however were still conducted to ensure the chassis was properly integrated into the PPOD and ready for qualification testing.

The bus structure underwent a 0 dB GEVS random vibration qualification profile for all three axes. Before and after each random vibration profile a sine sweep was conducted. As discussed in Section 2.3.2, frequency shifts in pre and post vibe sine sweeps indicate a change in stiffness generally due to structural and/or mechanical failure. In addition to the sine sweeps, modal analysis was conducted after completing the full three axis GEVS profile. This was conducted to isolate the frequency response of the chassis from the PPOD to verify if the chassis was degraded and the effect on its mode shape.

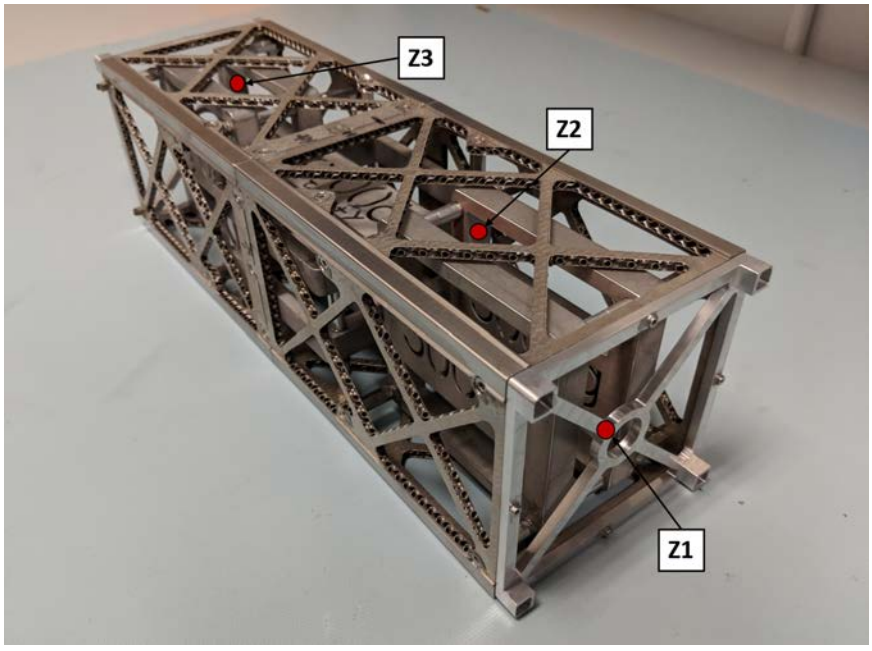

Figure 6.24. Accelerometer Locations - Z Axis

Seven PCB ultra lightweight accelerometers were used to monitor the accelera-

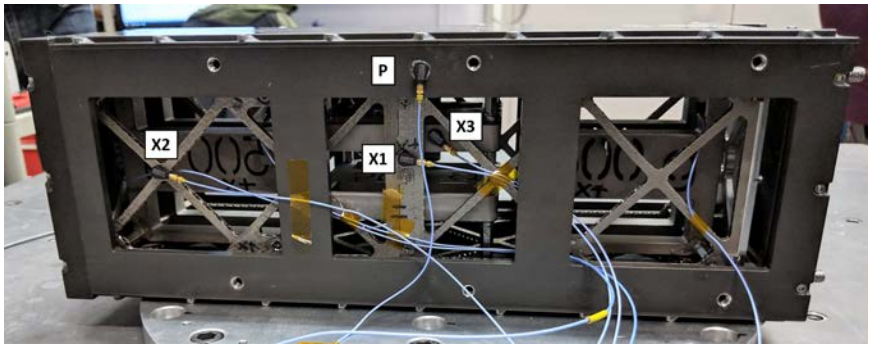

Figure 6.25. Accelerometer Locations - X Axis

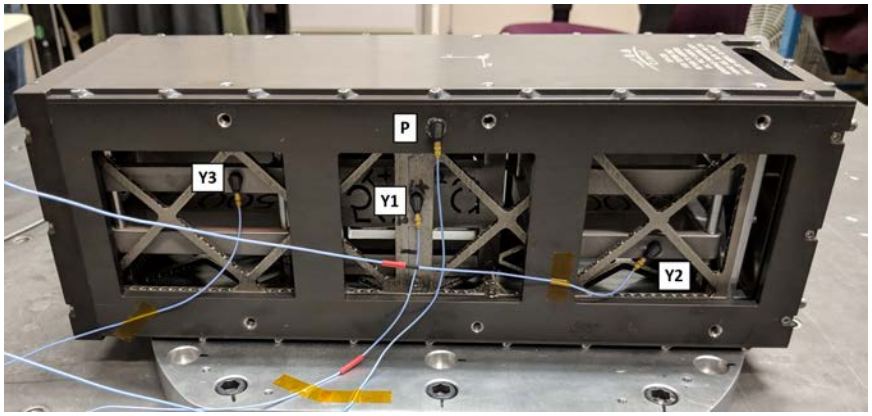

Figure 6.26. Accelerometer Locations - Y Axis

tion imparted on the bus structure and PPOD and evaluate the frequency response during sine sweeps. The accelerometers were attached using beeswax to the locations depicted in Figures 6.24-6.26. The locations were chosen to capture areas of greatest displacement according to the mode shapes witnessed in the topology study in Chapter III. Two accelerometers were placed on each axis; the final accelerometer was place on the exterior of the PPOD in line with direction of vibration. The test setup for the X/Y and Z axis are shown in Figure 6.27. The bus structure was rotated along the Z axis within the PPOD in lieu of changing the orientation of the shaker table or PPOD. This enabled the Y and X axis test to be conducted in the same setup.

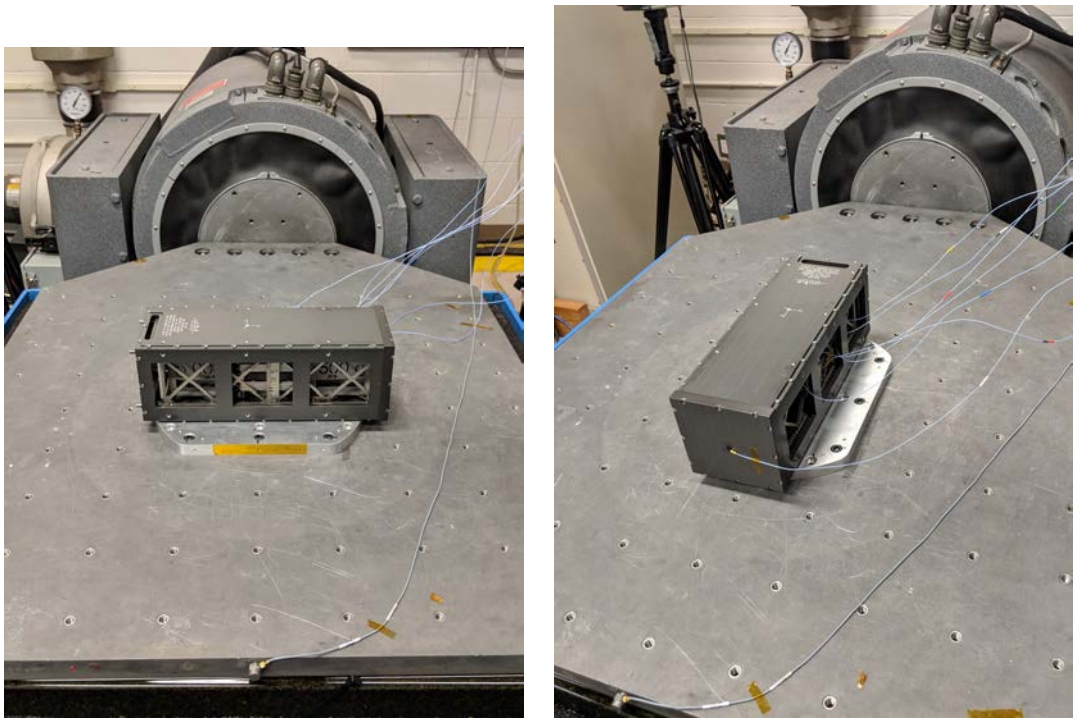

(a) X/Y Axis **(b)** Z Axis

Figure 6.27. Shaker Table Setup

6.4.2 GEVS Qualification Test Results

The GEVS qualification test began by testing the bus structure in the Z-axis. The vibration profile completed without any visual indications of failure. The post-sine sweep revealed a shift of approximately 50 Hz of the peaks from the pre-sine sweep, indicating a reduction in stiffness. The system was run through a second vibrational profile to determine whether the system would further degrade or settle at these new frequencies. The second post sine sweep indicated there were minimal to no changes in the system after the second random vibration. The results of each sine sweep are included in Figure 6.28. Only the Z1 channel was included to reduce confusion of overlaying 12 signals. The other channels reflected the same response at varying magnitudes.

After completing the Z-axis profiles, the system was rotated in line with the X and

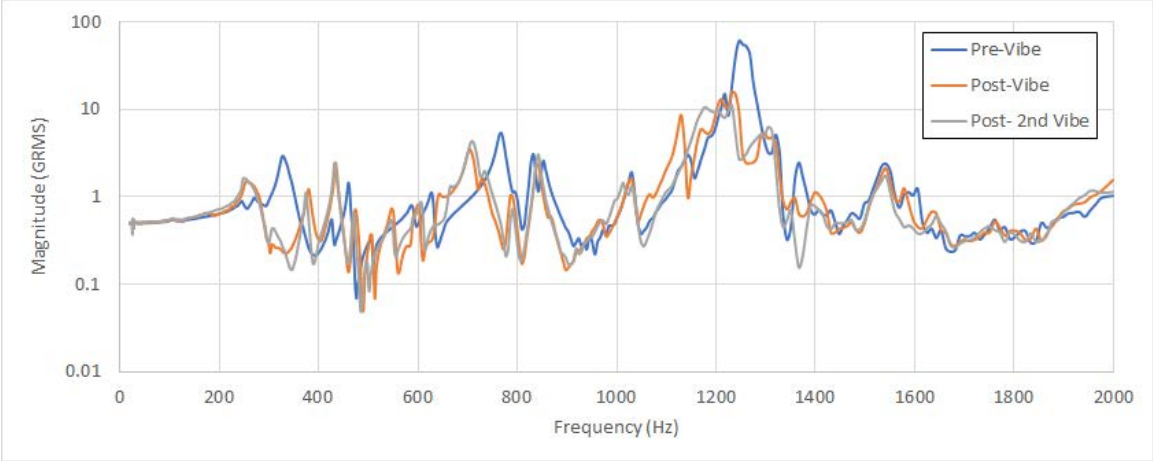

Figure 6.28. Sine Sweep Before and After Random Vibration (Z-Axis)

Y axes. The next test was conducted in the chassis' Y-axis. A similar result as the Z-axis was observed for the Y-axis. As shown in Figure 6.29, the sine sweep followed the same trend. The frequency shift occurred after the first vibrational profile, in the same direction as the Z-axis. The third sine sweep, conducted after the second vibrational profile, matched the peaks of the second sine sweep.

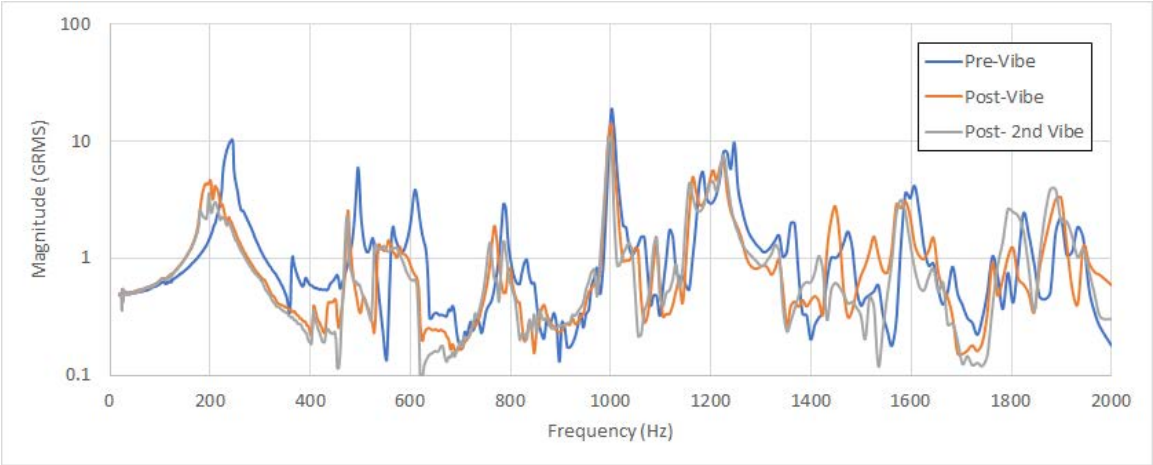

Figure 6.29. Sine Sweep Before and After Random Vibration (Y-Axis)

Testing the X-axis required the chassis to be removed and re-integrated with the X-axis in line with the direction of vibration. Upon completion of the required steps the system was excited in the X-axis. Consistent with the previous axes, the

frequencies shifted left (lower frequency). However, after the second vibration profile, the following sine sweep indicated an additional frequency shift. For the Z and Y axis it was concluded that the initial shift may have been due to the structure shifting and settling in the PPOD. This shift has been observed in numerous other tests with the PPOD at AFIT. Three consecutive shifts would indicate a structural failure may have occurred.

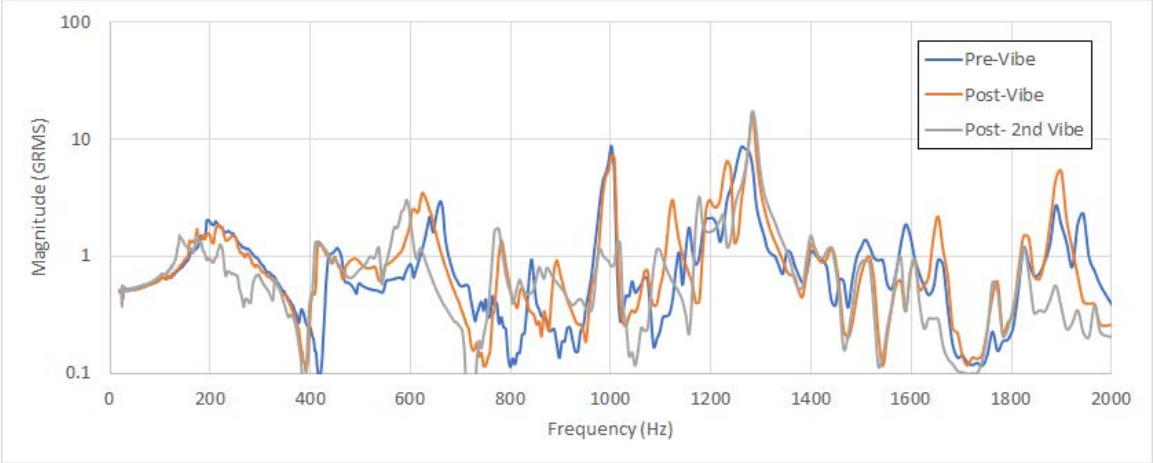

Figure 6.30. Sine Sweep Before and After Random Vibration (X-Axis)

Upon removal from the PPOD, visual inspection of the chassis provided no indications of structural failure. Inspection of the fasteners' torque stripes and staking verified all fasteners remained in place throughout the tests. However, inspection of the PPOD revealed a considerable quantity of metal residue within the enclosure. In particular, it was noted that the residue was especially concentrated in two locations, as identified in Figure 6.31. The first area was on the rails near the male/female interface at the midsection of the bus structure. The second location was on the rail that was in contact with the exposed substructure of the flawed rail. The vibration load may have caused the rough surface of the exposed substructure to grind against the contacting surface, breaking off metal particles that were discovered within the PPOD. This is a major concern for operational application. Floating metal residue

could come in contact with sensitive electronics, potentially shorting connections and causing severe damage, failure, or degradation to the system.

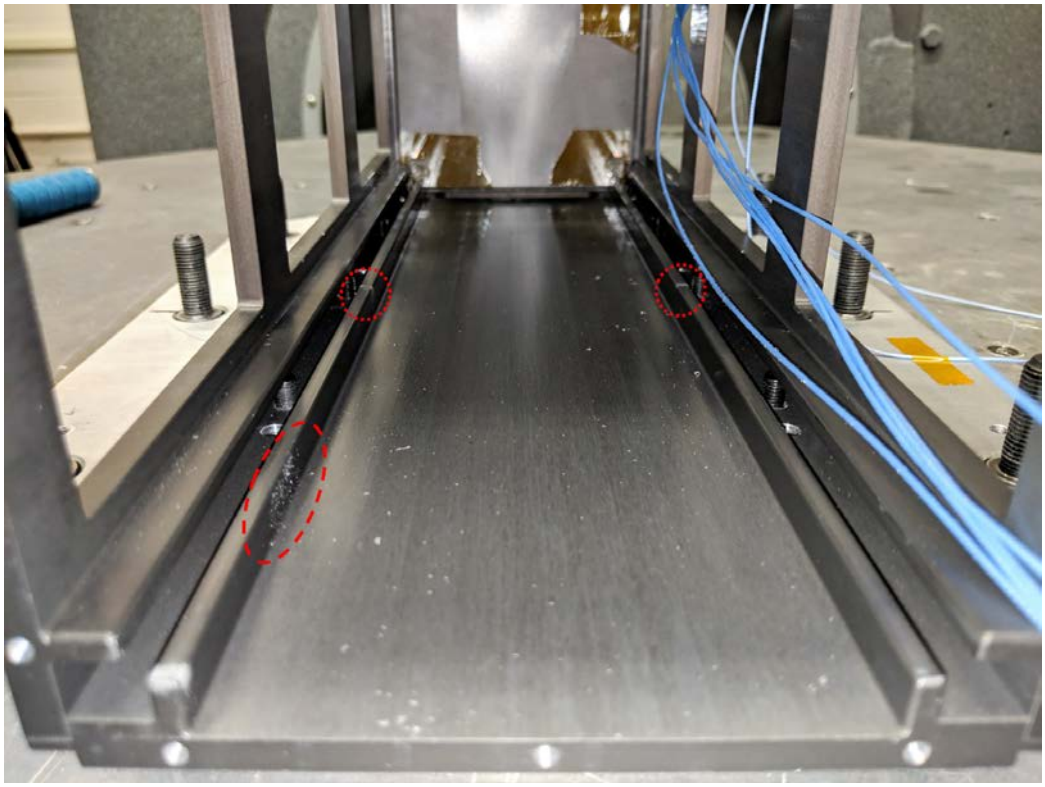

Figure 6.31. Metal Residue in PPOD after Vibration Testing

Modal analysis of the chassis, separate from the PPOD. was conducted to aid in the identification of any structural failure. An analysis with the laser vibrometer was conducted on both axes to compare the post vibe results to the initial frequency responses measured in Section 6.3.2 of this chapter. The results of the Y-Axis indicated a frequency shift occurred at the first mode (Figure 6.32). Analysis in the X-axis provided an unexpected result. In addition to shifting left, the magnitude of the first mode was drastically reduced. The reduction was so acute, the peak was practically eliminated from the frequency response plot.

The results of the modal analysis indicated a failure must have occurred. The bus structure was disassembled to inspect each part of the bus assembly. Upon removal

of the middle mass stack, a loose standoff was identified. No other damage to the bus structure, fasteners, or mass stacks was identified. A new standoff was installed on the mass stack and the chassis was reassembled. A second modal analysis was conducted to verify the effect of the loose standoff. The magnitude of the first mode peak was restored, as shown in Figure 6.33. It was concluded that the loose connection between the mass stack and the chassis transformed the mass effectively into a Tuned Mass Damper (TMD) [78]. Functioning as a TMD, the magnitude of the frequency at this mode was effectively eliminated.

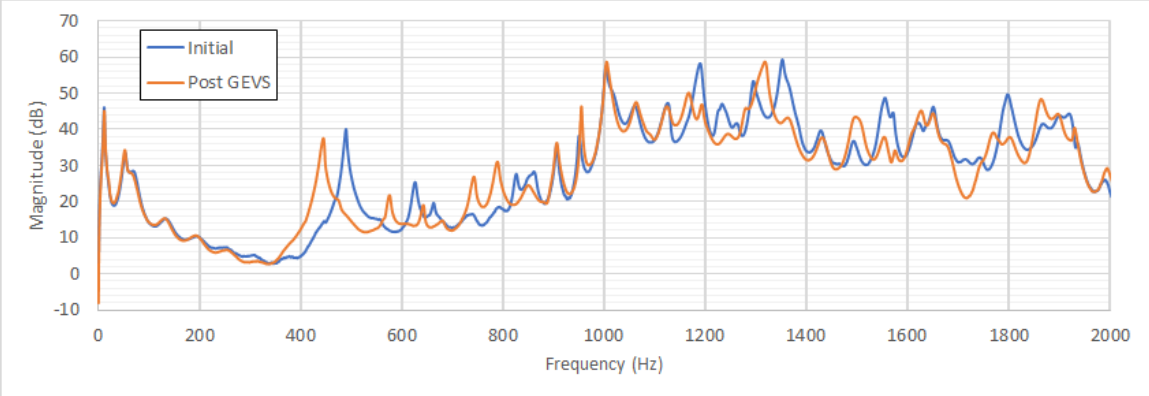

Figure 6.32. Modal Analysis of Inconel Chassis with Mass Stacks Pre/Post GEVS (Y-Axis)

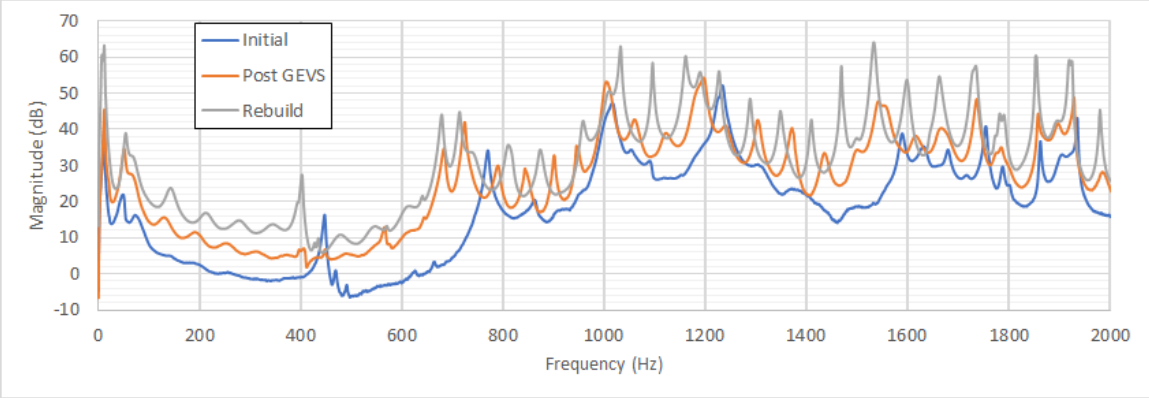

Figure 6.33. Modal Analysis of Inconel Chassis with Mass Stacks Pre/Post GEVS (X-Axis)

The final verification of the structural integrity of the bus structure was achieved

through a modal analysis without the mass stacks. Figures 6.34 and 6.35 illustrated the results of these analyses. The results indicate a minimal effect on the first two modes. However, divergence from the baseline can be see at the third and fourth mode. The third mode was shifted left while the fourth mode split into two separate peaks where the original fourth mode peak was located.

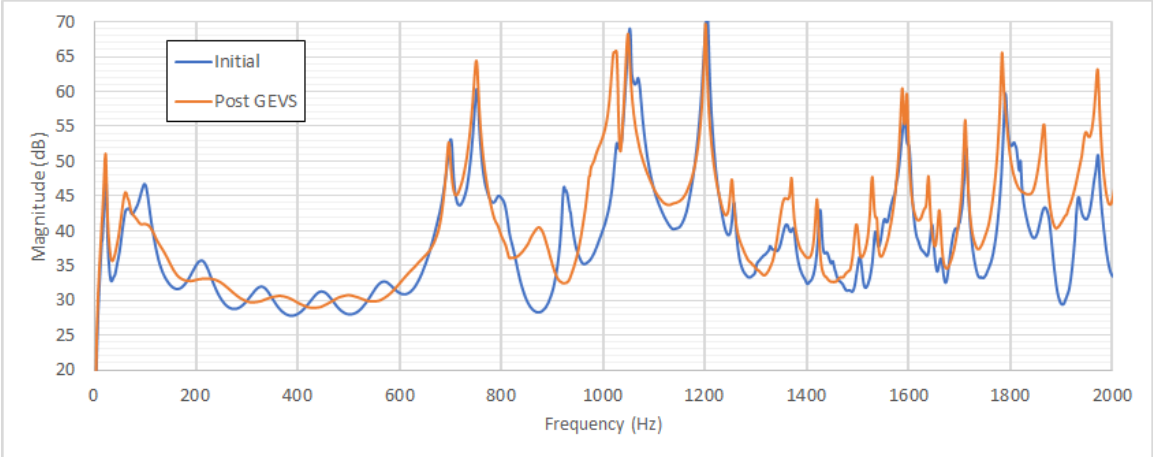

Figure 6.34. Modal Analysis of Empty Inconel Chassis Pre/Post GEVS (X-Axis)

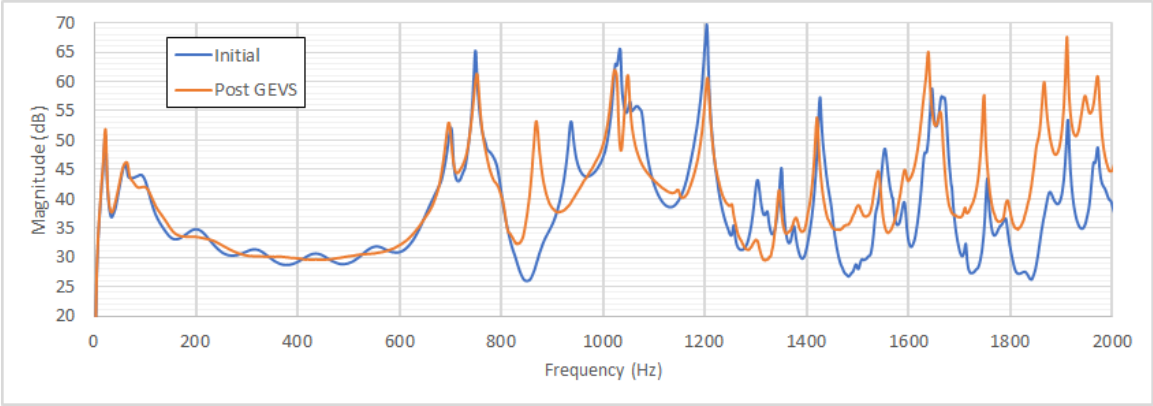

Figure 6.35. Modal Analysis of Empty Inconel Chassis Pre/Post GEVS (Y-Axis)

Determining whether the GEVS qualification test was successful can be subjective when purely evaluating the structural integrity of the CubeSat. In regards to meeting the desired 70 Hz minimum requirement, the TPMS based bus structure well exceeded the threshold. Although a significant shift occurred after the first run, the coupled

frequency response of the chassis/PPOD system remained consistent in subsequent random vibration profiles. The exception was found for the X-axis due to a failure of a mass stack standoff, independent from the structure of the bus. The initial reduction of stiffness may have been caused by partially melted powder breaking free from the main structure. Alternatively, considerable residual stress develops throughout the AM print process. No stress relief measures were taken prior to testing and may have contributed to these abnormal results. Based on the results and conclusions discussed in this section it was determined that the GEVS qualification test was successful. Further studies are recommended to determine the cause of this initial frequency shift.

6.5 Summary

This chapter discussed the results of the final bus structure design and fabrication, evaluation, and qualification testing. The fabrication process highlighted the advantages and disadvantages of implementing current AM technologies. It was shown a mass efficient structure could be fabricated from a high density material such as Inconel 718. The modal analysis compared the various bus structures and evaluated the chassis' performance in terms of stiffness-to-weight. A three axis vibrational qualification test with payload mass simulators installed was conducted following the GEVS generalized random vibration test levels. The qualification test verified the structure met the required frequency threshold and could survive the vibrational load imparted during launch. However, the test also identified concerns that would need to be addressed for operational feasibility. The following chapter will summarize the findings from this research, discuss the significance of these findings, and provide future research recommendations.

VII. Conclusion and Recommendations

7.1 Summarized Findings

The research in this thesis examined the application of metamaterials for multifunctional space structures enabled via Additive Manufacturing (AM). The design and evaluation of the bus structure of a CubeSat required a comprehensive multifaceted approach. Four studies were conducted within this research to investigate the feasibility and performance of such a structure.

In the first study, the topology of the bus structure was evaluated through Finite Element Analysis (FEA). The study yielded a high stiffness and lightweight design; while meeting the geometric constraints imparted by Poly Picosatellite Orbital Deployer (PPOD) integration requirements. Additionally, the topology design established a threshold of the maximum density of the metamaterial to ensure the final design of the bus would be mass efficient.

A trade study of materials commonly used in AM was conducted in the second study. The study investigated which material would enabled the fabrication of high stiffness-to-weight metamaterials. The emphasis on superior material printability, a necessary characteristic for enabling thin walled structures with fine features drove the results towards high stiffness, high density, and small melt pool track width materials. It was concluded SS 316, Ti6Al4V, and Inconel were all viable alternatives. All three materials exhibited a roughly equivalent specific stiffness. SS 316 benefited due to its superior printability and material cost. Ti6Al4V provided superior performances characteristics but was limited by its significantly greater cost. Inconel 718 resulted in the most well rounded alternative. Depending on the preferences and needs of the space system developer, any of these three materials were determined to be viable solutions.

The third study examined the design and performance of various Triply Periodic Minimal Surface (TPMS) based metamaterials. The study demonstrated that superior characteristics could be designed into a metamaterial. The stiffness-to-weight ratio of all but one of the TPMS sandwich beams exceeded the performance of a 7075-T6 aluminum beam; providing increases up to 17.8% for TPMS based metamaterials. Additionally, control of the design variables, enabled the equivalent material properties of the metamaterial to be tailored as necessary. This control allowed a significant reduction in the equivalent density to meet the limit imposed by the topology study. Experimentally, it was concluded gyroids were the superior type of TPMS. Finally, the study demonstrated the viability of modeling TPMS structures through shell based elements.

The final study leveraged the results of the previous studies to design, evaluate, and qualify a 3u bus structure. The results of the design and fabrication of the chassis highlighted the benefits and disadvantages of current AM processes. The final mass of the structure, printed in Inconel 718, was 480 grams. Solar panel mounts were integrated directly to the outer skin of the structure. These features demonstrated a mass efficient multifunctional bus structure could be produced from a high density material through the application of metamaterials and AM. However, difficulties in accurately and precisely printing parts to the desired dimensions demonstrated the immaturity of the current AM processes. These inaccuracies drove design changes that exceeded the physical acceptance criteria of an operational 3U CubeSat. A simple solution to this issue would be to design interfaces and machined surfaces with large margins to ensure sufficient material is present to overcome the differences between the design and printed part. However, the the additional material required in this solution would add a significant amount of mass to the structure. The preferred, but more complex solution, would require investigation into the print parameters and

thermal loading of fine structures. Optimizing the print parameters may eliminate or dramatically reduce the swelling, shrinkage, and residual stresses that occurred during the print process.

Modal Analysis of a commercial solid aluminum 3U chassis, lattice based aluminum chassis, and the TPMS based Inconel chassis designed in this study concluded the Inconel chassis did not provide the highest stiffness-to-weight ratio. The lattice based chassis exhibited higher natural frequencies. However, adding representative payload mass to the system demonstrated the Inconel chassis provided similar frequency values at nearly half the structural mass, a significant improvement. The structural integrity of the bus and coupled PPOD/Cubesat frequency threshold was validated through vibration testing in accordance with General Environmental Verification Standard (GEVS) random vibration requirements. Tests result validated the systems natural frequency was well above the required 70 Hz threshold. Sine sweeps conducted before and after each random vibration resulted in a frequency shift after the initial random vibration of each axis. Sine sweeps conducted after subsequent randoms vibrations indicated the structure had stabilized at the lower frequency. An exception was observed in the X-axis, in which the frequency peak continued to shift. Further analysis indicated the issue was not related to the structure of the chassis. The cause was traced to a loose standoff on one of the mass stacks.

7.2 Research Significance

This research provided several valuable insights into future small satellite design. Due to the complexity and non-availability of commercial Computer Aided Design (CAD) software capable of generated TPMS geometries, FEA of structures integrating these geometries had not been seen in literature to date. The ability to accurately model these complex structures and evaluate them computationally, will significantly

accelerate their use in future design. Specifically, this will enable for optimization of the metamaterial design, resulting in TPMS based metamaterials far exceeding the performance demonstrated experimentally in this research.

The performance of the Inconel chassis demonstrated the structure was over designed despite efforts to minimize volume of the topology and final mass. This point is reinforced when considering the extremely lightweight design of the Pumpkin Inc skeletonized chassis. The minimalist approach of Pumpkin Inc.'s design leverages the additional stiffness provided by the payload within the chassis. In a larger 6U form factor, the support from payload significantly decreases and longer unsupported spans are required. In even larger 12U and 27U Cubesats the 1U payload stacks can only be mounted to a maximum of three faces of the exterior structure, significantly reducing any stiffness provided by the payload stack. In these larger CubeSats, the advantages of the metamaterials demonstrated in this research would provide considerable benefits compared to traditional materials. Additionally, it is important to consider the effects of the constraints imposed on the final design due to limitations imposed by equipment available for this research. The material was constrained to Inconel 718 and the M2 build chamber could not accommodate the height of a full 3U structure, requiring a two part male/female design. It was estimated the two part design increased the total mass by approximately 97 grams compared to a single structure design. Printing the part with less dense Ti6Al4V, could further decrease the mass by an estimated 147 grams. The resulting mass of a single structure Ti6Al4V chassis would be an impressive 236 grams; 16 grams lighter than the sheet aluminum Pumpkin Inc. chassis. This reinforces the potential of incorporating the ideas covered in this research to produce superior lightweight space structures.

Finally, significant benefits in terms of rapid deployment and cost savings can be attained through the use of AM. The bus structure in this research was printed

over a 36 hour period. An additional five days of post processing were required to produce the final design. The total cost, including labor, was estimated to be $8K, while the Pumpkin Inc. skeletonized chassis can be purchased for $2.25K. However, as advances in AM technologies are made, the design space will expand and the dimensional accuracy will improve, reducing post processing. These improvements will significantly reduce the time and cost to produce functional AM parts. Coupling these improvements and the efficiencies of mass production, it may be possible to produce an AM CubeSat bus structure in a matter of days at equivalent cost.

7.3 Future Work

Many of the studies conducted in this research were limited in scope due to time constraints. Further investigation is necessary to thoroughly explore advantages of metamaterials and AM in space systems. A few pertinent avenues of research will be discussed in this section.

Beginning with the topology study, it is recommended a comprehensive topology optimization study be conducted. As seen with the Pumpkin chassis, the topology of the bus structure is critical to the performance. This would enable the stiffness-to-weight ratio to be targeted such that a fully loaded chassis would meet the 70 Hz threshold while determining the absolute minimum mass required.

The Finite Element Model (FEM) developed in this research was completed after selecting the metamaterial for the bus structure design. Further research should be conducted to optimize the equivalent material properties of the TPMS metamaterials. The design could be optimized through computational analysis and validated through the experimental analysis conducted in this research. Additionally, expanding the FEM to the entire bus structure would enable potential designs to be evaluated without the expense of experimental testing.

Finally, it would be beneficial to apply the concepts of this research to larger 12U or 27U CubeSat for a specific payload. As discussed previously, additional stiffness from the application of metamaterials provided excessive stiffness for a 3U CubeSat. A larger bus would provide a design space in which metamaterials and AM could truly demonstrate their benefits compared to traditional manufacturing. A known payload would enable the bus structure to be customized to the specific needs of the payload and its mission, demonstrating the flexibility of AM design.

7.4 Conclusion

AM has an important role in the future designs of space systems. Only AM provides capability to produce metamaterials with superior performance characteristics such as the TPMS based sandwich beams discussed in this research. These technologies are necessary to improve existing designs, which are limited to incremental improvements within the traditional design space. However, until dimensional accuracy of the modern printers improve, application of AM will be limited in scope.

Appendix A. TPMS Shell Matlab Script

```
%% Generate a STL of a TPMS based structure
%   Author: Ryan O'Hara, 02-05-18
%   Edited: Michael Macchia, 01-15-19

clear all
close all
clc

fileName='ScwarzP_375Width';
t=0;
v=0.01; % isovalue - isosurface connects points that have the specified
       % value much the way contour lines connect points of equal ...
          elevation
phi=0; % phi offset for period

start=0; % period starting value

% period=2*pi; % period
finalHt=[3.75 25.4 156];% final height of resulting shape [x y z]
per = [.628 .628 .628];  % Periodicity chosen in nTop [x y z]

cellUnitSize = 20*per/pi;  % cell unit size in each direction
cells= finalHt./cellUnitSize; % number of unit cell desired [x y z]
period=cells*2*pi; % period

meshHt=finalHt./period;% mesh scaling factor based on final ht
                       % *Note needed to scale from period to actual
                       % engineering height
meshResolution=.1; % mm
meshSpacing=finalHt/meshResolution;
nX=meshSpacing(1);  % index for spacing of x-grid
nY=meshSpacing(2);  % index for spacing of y-grid
nZ=meshSpacing(3);  % index for spacing of z-grid

x=linspace(start,period(1),nX)+phi; %1-d x-array
y=linspace(start,period(2),nY)+phi; %1-d y-array
z=linspace(start,period(3),nZ)+phi; %1-d z-array
[Xx,Yy,Zz]=meshgrid(x,y,z); %3-d matrix

%% Define the Function that describes the shape you would like
% Fshape=cos(Xx).*sin(Yy)+cos(Yy).*sin(Zz)+cos(Zz).*sin(Xx); % Gyroid
Fshape=cos(Xx)+cos(Yy)+cos(Zz)-t; % Schwarz P

%% Generate a Surface
FVI=isosurface(Xx,Yy,Zz,Fshape,v); % Generate the Iso-Surface
FVC=isocaps(Xx,Yy,Zz,Fshape,v);    % Generate Iso-Caps (closed ...
   surface, if desired)
for i=1:3
```

```
47 FVI.vertices(:,i)=FVI.vertices(:,i)*meshHt(i);% Scale the ...
       Iso-Surface Vertices
48 end
49 %% Plot Unit Cell
50 close all;
51 figure;  %  Create a New Figure
52 p1=patch(FVI); % Patch the Iso-Surface Only
53 set(p1, 'FaceColor', 'red', 'EdgeColor', 'black'); % Set Surface Colors
54 daspect([1 1 1]) % Adjust the Aspect Ratio
55 view(3) % Orient the View
56 grid on  % Turn the Grid On
57 axis equal % Set Axis Equal
58
59 %% Output STL
60 patch2stl([fileName '.stl'],FVI) % Use Custom patch2Stl function to ...
       output a surface stl
```

Appendix B. "patch2stl" Matlab Function

```
function patch2stl(filename,p,mode)
%PATCH2STL   Write STL file from patch (vertices/faces) data.
%   PATCH2STL('filename',p) writes a stereolithography (STL) file
%   for a patch mesh defined by P. P must be a structure with 'VERTICES'
%   and 'FACES' fields.
%
%   PATCH2STL(...,'mode') may be used to specify the output format.
%
%     'binary' - writes in STL binary format (default)
%     'ascii'  - writes in STL ASCII format
%
%   Example:
%
%       tmpvol = zeros(20,20,20);       % Empty voxel volume
%       tmpvol(8:12,8:12,5:15) = 1;     % Turn some voxels on
%       fv = isosurface(tmpvol, 0.99);  % Create the patch object
%       patch2stl('test.stl',fv)        % Save to binary .stl

%   Based on surf2stl by Bill McDonald
%
%   Author: Sven Holcombe, 07-30-08

error(nargchk(2,3,nargin));

if (ischar(filename)==0)
    error( 'Invalid filename');
end

if (nargin < 3)
    mode = 'binary';
elseif (strcmp(mode,'ascii')==0)
    mode = 'binary';
end

if (~(isfield(p,'vertices') && isfield(p,'faces')))
    error( 'Variable p must be a faces/vertices structure' );
end

if strcmp(mode,'ascii')
    % Open for writing in ascii mode
    fid = fopen(filename,'w');
else
    % Open for writing in binary mode
    fid = fopen(filename,'wb+');
end

if (fid == -1)
```

```
48      error('patch2stl:cannotWriteFile', 'Unable to write to %s', ...
            filename);
49  end
50
51  title_str = sprintf('Created by patch2stl.m %s',datestr(now));
52
53  if strcmp(mode,'ascii')
54      fprintf(fid,'solid %s\r\n',title_str);
55  else
56      str = sprintf('%-80s',title_str);
57      fwrite(fid,str,'uchar');          % Title
58      fwrite(fid,0,'int32');            % Number of facets, zero for now
59  end
60
61  nfacets = 0;
62  % Main loop
63  for i=1:length(p.faces)
64      p123 = p.vertices(p.faces(i,:),:);
65      val = local_write_facet(fid,p123(1,:),p123(2,:),p123(3,:),mode);
66      nfacets = nfacets + val;
67  end
68
69  if strcmp(mode,'ascii')
70      fprintf(fid,'endsolid %s\r\n',title_str);
71  else
72      fseek(fid,0,'bof');
73      fseek(fid,80,'bof');
74      fwrite(fid,nfacets,'int32');
75  end
76
77  fclose(fid);
78
79  disp( sprintf('Wrote %d facets',nfacets) );
80
81
82  % Local subfunctions
83
84  function num = local_write_facet(fid,p1,p2,p3,mode)
85
86  if any( isnan(p1) | isnan(p2) | isnan(p3) )
87      num = 0;
88      return;
89  else
90      num = 1;
91      n = local_find_normal(p1,p2,p3);
92
93      if strcmp(mode,'ascii')
94
95          fprintf(fid,'facet normal %.7E %.7E %.7E\r\n', ...
                n(1),n(2),n(3) );
96          fprintf(fid,'outer loop\r\n');
97          fprintf(fid,'vertex %.7E %.7E %.7E\r\n', p1);
```

```
98          fprintf(fid,'vertex %.7E %.7E %.7E\r\n', p2);
99          fprintf(fid,'vertex %.7E %.7E %.7E\r\n', p3);
100         fprintf(fid,'endloop\r\n');
101         fprintf(fid,'endfacet\r\n');
102
103     else
104
105         fwrite(fid,n,'float32');
106         fwrite(fid,p1,'float32');
107         fwrite(fid,p2,'float32');
108         fwrite(fid,p3,'float32');
109         fwrite(fid,0,'int16');  % unused
110
111     end
112
113 end
114
115
116 function n = local_find_normal(p1,p2,p3)
117
118 v1 = p2-p1;
119 v2 = p3-p1;
120 v3 = cross(v1,v2);
121 n = v3 ./ sqrt(sum(v3.*v3));
```

Appendix C. CubeSat Acceptance Checklist

3U CubeSat Acceptance Checklist

Project: MacchiaThesis
Organization: AFIT
Satellite Name: Inconel 3U

Date/Time: 29JAN2019/1230
Location: AFIT Environmental Lab
Satellite S/N: N/A

Engineers: Michael Macchia
Dustin Graves

Mass (< 4 kg)	3.634 kg	**RBF Pin** (≤6.5mm)	
Spring Plungers	Option A / B Functional Y / N N/A	**Rails Anodized**	Y (N)
Deployment Switches	Functional Y / N N/A	**Deployables Constrained**	Y / N N/A

Mark on the diagram the locations of the RBF pin, connectors, deployables, and any envelope violations.

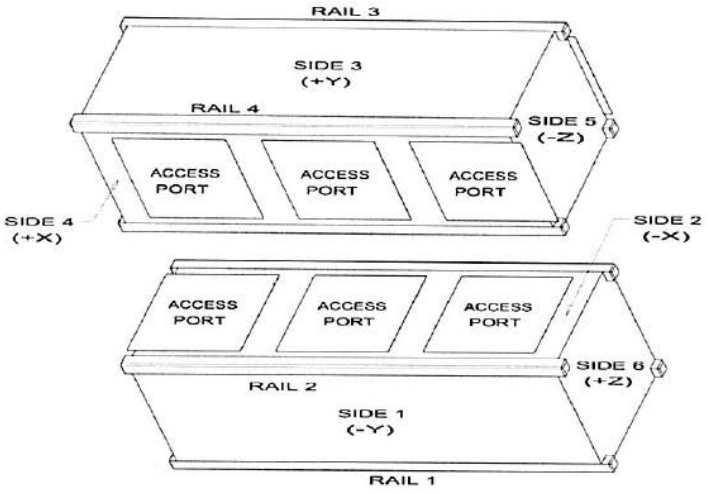

Authorized By:
IT #1: MM
IT #2: DPL
Passed: Y (N)

List Item	As Measured				Required
Width [x-y]	Side 1 (-Y)	Side 2 (-X)	Side 3 (+Y)	Side 4 (+X)	
+Z	100.52	100.56	100.50	100.62	100.0 ± 0.1mm
Middle	100.67	100.69	100.57	100.64	100.0 ± 0.1mm
-Z	100.54	100.64	100.48	100.64	100.0 ± 0.1mm
Height [x-y]	Rail 1 (+X, -Y)	Rail 2 (-X, -Y)	Rail 3 (-X, +Y)	Rail 4 (+X,+Y)	
	339.9	339.91	339.9	339.9	340.5 ± 0.3mm
	Rail 1 (+X, -Y) length x width	Rail 2 (-X, -Y) length x width	Rail 3 (-X, +Y) length x width	Rail 4 (+X, +Y) length x width	
+Z Standoffs	8.5 x 8.41	8.43 x 8.48	8.5 x 8.49	8.51 x 8.46	≥ 6.5mm
-Z Standoffs	8.52 x 8.54	8.47 x 8.48	8.48 x 8.51	8.49 x 8.51	≥ 6.5mm
Protrusions	Side 1 (-Y)	Side 2 (-X)	Side 3 (+Y)	Side 4 (+X)	Side 5 (-Z)	Side 6 (+Z)	
	ϕ	6.1	ϕ	6.3	ϕ	ϕ	≤ 6.5mm

Bibliography

[1] M. Swartwout, "The first one hundred CubeSats : A statistical look," *Journal of Small Satellites*, vol. 2, no. 2, pp. 213–233, 2013. [Online]. Available: http://www.jossonline.com/

[2] ——, "You say 'Picosat', i say "CubeSat': Developing a better taxonomy for secondary spacecraft," *IEEE Aerospace Conference Proceedings*, vol. 2018-March, pp. 1–17, 2018.

[3] ——, "Cheaper by the dozen: The avalanche of rideshares in the 21st century," *IEEE Aerospace Conference Proceedings*, pp. 1–12, 2013.

[4] NRO, "National Reconnaissance Office 2013 Innovation Campaign: The CubeSat Program," 2013. [Online]. Available: http://www.nro.gov/about/innovation/2013-05.pdf{%}5Cnhttp://www.nro.gov/about/innovation/{%}5Cnhttp://www.nro.gov

[5] B. A. Corbin, "The Value Proposition of Distributed Satellite Systems for Space Science Missions," Ph.D. dissertation, Massachusetts Institute of Technology, 2015.

[6] C. Jilla and D. Miller, "A Multiobjective, Multidisciplinary Design Optimization Methodology for the Conceptual Design of Distributed Satellite Systems," *9th AIAA/ISSMO Symposium on Multidisciplinary Analysis and Optimization*, 2002. [Online]. Available: http://arc.aiaa.org/doi/10.2514/6.2002-5491

[7] J. D. Fielding *et al.*, "Department of Defense Joint Additive Manufacturing Roadmap," *Defense Manufacturing Conference*, no. November, pp. 1–31, 2016. [Online]. Available: http://ammo.ncms.org/documents/Resources/Other/DMC{_}DoD{_}AM{_}Roadmap{_}Briefing{_}30{_}Nov{_}2016{_}FINAL.pdf

[8] NASA Spaceflight, "Rocket Lab launches first operational Electron mission NASASpaceFlight.com," 2018. [Online]. Available: https://www.nasaspaceflight.com/2018/11/rocketlab-operational-electron-launch-five-payload/

[9] ——, "Rocket Lab Electron launches ELaNa-XIX mission NASASpaceFlight.com," 2018. [Online]. Available: https://www.nasaspaceflight.com/2018/12/rocket-lab-nasa-mission-electron-elana-xix/

[10] Space.com, "SpaceX Launching 64 Satellites Today: Watch It Live," 2018. [Online]. Available: https://www.space.com/42604-spacex-falcon9-ssoa-launch-webcast.html

[11] K. A. Roberts, "Design and Testing of an additively manufactured CubeSat Structural Bus," Master's Thesis (AFIT-ENY-MS-18-M-289), Air Force Institute of Technology, 2018.

[12] O. Al-Ketan *et al.*, "Topology-mechanical property relationship of 3D printed strut, skeletal, and sheet based periodic metallic cellular materials," *Additive Manufacturing*, vol. 19, pp. 167–183, 2018. [Online]. Available: http://dx.doi.org/10.1016/j.addma.2017.12.006

[13] B. J. Horais *et al.*, "The Use of Additive Manufacturing for Fabrication of Multi-Function Small Satellite Structures," *Conference on Small Satellites*, 2013. [Online]. Available: http://digitalcommons.usu.edu/cgi/viewcontent.cgi?article=2929{&}context=smallsat

[14] S. H. Huang *et al.*, "Additive manufacturing and its societal impact: A literature review," *International Journal of Advanced Manufacturing Technology*, vol. 67, no. 5-8, pp. 1191–1203, 2013.

[15] W. J. Sames *et al.*, "The metallurgy and processing science of metal additive manufacturing," *International Materials Reviews*, vol. 61, no. 5, pp. 315–360, 2016.

[16] D. Systemes, "Abaqus 6.14 Online Documentation," 2014. [Online]. Available: http://dsk.ippt.pan.pl/docs/abaqus/v6.13/index.html

[17] Concept Laser, "Mlab cusing R Metal laser melting system," Concept Laser, Tech. Rep., 2018. [Online]. Available: https://www.concept-laser.de/fileadmin/Machine{_}brochures/CL{_}Mlab{_}200R{_}DS{_}EN{_}A4{_}2{_}v1.pdf

[18] ——, "M2 cusing Metal laser melting system," Concept Laser, Tech. Rep., 2018. [Online]. Available: www.ge.com/additive

[19] Polytec, "PSV-400 Scanning Vibrometer 1-D and 3-D Vibration Measurement, Imaging and Analysis 2 Vibrations Made Visible," Polytec, Tech. Rep., 2005. [Online]. Available: www.polytec.com/int/vib-university

[20] A. Mehrpavar *et al.*, "Cubesat design specification," *The CubeSat Program, California Polytechnic State*, 2013.

[21] E. Mabrouk, "What are smallsats and cubesats?" *NASA*, Mar 2015. [Online]. Available: https://www.nasa.gov/content/what-are-smallsats-and-cubesats

[22] D. F. Everett *et al.*, *Space Mission Engineering: The New SMAD*. Microcosm Press, 2015.

[23] P. S. Corporation, "Canisterized satellite dispensor (csd) data sheet," *Planetary Systems Corporation,Tech. Rep.*, 2015.

[24] ——, "Payload specifications for 3u, 6u, 12u, and 27u," *Planetary Systems Corporation,Tech. Rep.*, 2016.

[25] D. G. Miller, "Vibrational Analysis of a 12U Chassis," Master's Thesis (AFIT-ENY-MS-16-M-229), Air Force Institute of Technology, 2016.

[26] T. NASA Goddard Space Flight Center, Greenbelt, Maryland, "General Environmental Verification Standard (GEVS) For GSFC Flight Programs and Projects," NASA, Tech. Rep., 2018.

[27] C. Sheffield, "Lecture notes on CubeSat Environmental Testing, ASYS 632," Air Force Institute of Technology, Tech. Rep., July 2017.

[28] L. Meirovitch, *Fundamentals of Vibrations*. Waveland Press, 2010.

[29] A. Lou and C. Grosvenor, "Selective Laser Sintering , Birth of an Industry," *the University of Texas at Austin, Department of Mechanical Engineering 100 Years*, pp. 1–19, 2012. [Online]. Available: www.me.utexas.edu/news/2012/0712{_}sls{_}history.php{#}ch4

[30] Sandia National Laboratories, "Creating a complex metal part in a day is goal of commercial consortium." [Online]. Available: https://www.sandia.gov/media/lens.htm

[31] Arcam, "History - Arcam AB." [Online]. Available: http://www.arcam.com/company/about-arcam/history/

[32] I. A. Manriquez-Frayre and D. L. Bourell, "Selective Laser Sintering of Binary Metallic Powder," Center for Materials Science and Engineering, Tech. Rep., 1990. [Online]. Available: http://sffsymposium.engr.utexas.edu/Manuscripts/1990/1990-09-Frayre.pdf

[33] W. Gao *et al.*, "The status, challenges, and future of additive manufacturing in engineering," *CAD Computer Aided Design*, vol. 69, pp. 65–89, 2015. [Online]. Available: http://dx.doi.org/10.1016/j.cad.2015.04.001

[34] ASTM International, "F2792-12a - Standard Terminology for Additive Manufacturing Technologies," *Rapid Manufacturing Association*, pp. 10–12, 2013. [Online]. Available: http://www.ciri.org.nz/nzrma/technologies.html

[35] L. E. Murr *et al.*, "Metal Fabrication by Additive Manufacturing Using Laser and Electron Beam Melting Technologies," *Journal of Materials Science and Technology*, vol. 28, no. 1, pp. 1–14, 2012. [Online]. Available: http://dx.doi.org/10.1016/S1005-0302(12)60016-4

[36] J. Kruth *et al.*, "Lasers and materials in selective laser sintering," *Assembly Automation*, vol. 23, no. 4, pp. 357–371, dec 2003. [Online]. Available: https://www.emeraldinsight.com/doi/10.1108/01445150310698652

[37] L. M. Sochalski-Kolbus *et al.*, "Comparison of Residual Stresses in Inconel 718 Simple Parts Made by Electron Beam Melting and Direct Laser Metal Sintering," *Metallurgical and Materials Transactions A: Physical Metallurgy and Materials Science*, vol. 46, no. 3, pp. 1419–1432, 2015.

[38] W. Sames *et al.*, "Effect of Process Control and Powder Quality of Inconel 718 Produced using Electron Beam Melting," *The Minerals, Metals & Materials Society*, 2014. [Online]. Available: https://www.tms.org/Superalloys/10.7449/2014/Superalloys{_}2014{_}409{_}423.pdf

[39] Custompartnet.com, "DMLS - Direct Metal Laser Sintering." [Online]. Available: http://www.custompartnet.com/wu/direct-metal-laser-sintering

[40] I. Yadroitsev and I. Smurov, "Selective laser melting technology: From the single laser melted track stability to 3D parts of complex shape," *Physics Procedia*, vol. 5, no. PART 2, pp. 551–560, 2010. [Online]. Available: http://dx.doi.org/10.1016/j.phpro.2010.08.083

[41] D. Buchbinder *et al.*, "High power Selective Laser Melting (HP SLM) of aluminum parts," *Physics Procedia*, vol. 12, no. PART 1, pp. 271–278, 2011. [Online]. Available: http://dx.doi.org/10.1016/j.phpro.2011.03.035

[42] I. Yadroitsev *et al.*, "Strategy of manufacturing components with designed internal structure by selective laser melting of metallic powder," *Applied Surface Science*, vol. 254, no. 4, pp. 980–983, 2007.

[43] L. Thijs *et al.*, "Fine-structured aluminium products with controllable texture by selective laser melting of pre-alloyed AlSi10Mg powder," *Acta Materialia*, vol. 61, no. 5, pp. 1809–1819, 2013. [Online]. Available: http://dx.doi.org/10.1016/j.actamat.2012.11.052

[44] M. E. Orme *et al.*, "A Demonstration of Additive Manufacturing as an Enabling Technology for Rapid Satellite Design and Manufacturing." *Sampe*, no. August, p. 1, 2017. [Online]. Available: https://www.researchgate.net/publication/306578773{_}A{_}DEMONSTRATION{_}OF{_}ADDITIVE{_}MANUFACTURING{_}AS{_}AN{_}ENABLING{_}TECHNOLOGY{_}FOR{_}RAPID{_}SATELLITE{_}DESIGN{_}AND{_}FABRICATION

[45] D. Brackett *et al.*, "Topology Optimization for Additive Manufacturing," Tech. Rep., 2011. [Online]. Available: http://sffsymposium.engr.utexas.edu/Manuscripts/2011/2011-27-Brackett.pdf

[46] Jonaco Machine, "High Tolerance Machining," 2019. [Online]. Available: http://www.jonaco.com/high-tolerance-machining/

[47] E. Sachs *et al.*, "Three-Dimensional Printing: Rapid Tooling and Prototypes Directly from a CAD Model," *CIRP Annals - Manufacturing Technology*, vol. 39, no. 1, pp. 201–204, 1990.

[48] G. Sossou *et al.*, "An additive manufacturing oriented design approach to mechanical assemblies," *Journal of Computational Design and Engineering*, vol. 5, no. 1, pp. 3–18, 2018. [Online]. Available: https://doi.org/10.1016/j.jcde.2017.11.005

[49] D. Espalin *et al.*, "3D Printing multifunctionality: Structures with electronics," *International Journal of Advanced Manufacturing Technology*, vol. 72, no. 5-8, pp. 963–978, 2014.

[50] M. G. Lee *et al.*, "Mechanical analyses of Shellular, an ultralow-density material," *Acta Materialia*, vol. 103, pp. 595–607, jan 2016. [Online]. Available: https://www.sciencedirect.com/science/article/abs/pii/S1359645415300409

[51] S. C. Han *et al.*, "A New Type of Low Density Material: Shellular," *Advanced Materials*, vol. 27, no. 37, pp. 5506–5511, oct 2015. [Online]. Available: http://doi.wiley.com/10.1002/adma.201501546

[52] S. C. Kapfer *et al.*, "Minimal surface scaffold designs for tissue engineering," *Biomaterials*, vol. 32, no. 29, pp. 6875–6882, oct 2011. [Online]. Available: https://www.sciencedirect.com/science/article/pii/S0142961211006776

[53] D. W. Lee *et al.*, "Stiffness and yield strength of architectured foams based on the Schwarz Primitive triply periodic minimal surface," *International Journal of Plasticity*, vol. 95, pp. 1–20, 2017. [Online]. Available: http://dx.doi.org/10.1016/j.ijplas.2017.03.005

[54] S. Torquato *et al.*, "Multifunctional Composites: Optimizing Microstructures for Simultaneous Transport of Heat and Electricity," *Physical Review Letters*, vol. 89, no. 26, p. 266601, dec 2002. [Online]. Available: https://link.aps.org/doi/10.1103/PhysRevLett.89.266601

[55] D. J. Yoo, "Porous scaffold design using the distance field and triply periodic minimal surfacemodels," *Biomaterials*, vol. 32, no. 31, pp. 7741–7754, nov 2011. [Online]. Available: https://www.sciencedirect.com/science/article/pii/S0142961211007903

[56] D. Yoo, "New paradigms in hierarchical porous scaffold design for tissue engineering," *Materials Science & Engineering C*, vol. 33, pp. 1759–1772, 2013. [Online]. Available: http://dx.doi.org/10.1016/j.msec.2012.12.092

[57] D.-J. Yoo, "Recent trends and challenges in computer-aided design of additive manufacturing-based biomimetic scaffolds and bioartificial organs," *International Journal of Precision Engineering and Manufacturing*, vol. 15, no. 10, pp. 2205–2217, oct 2014. [Online]. Available: http://link.springer.com/10.1007/s12541-014-0583-7

[58] P. Göransson, "Acoustic and vibrational damping in porous solids," *Philosophical Transactions of the Royal Society of London A: Mathematical, Physical and Engineering Sciences*, vol. 364, no. 1838, pp. 89–108, 2006. [Online]. Available: http://rsta.royalsocietypublishing.org/content/364/1838/89

[59] A. Simone and L. Gibson, "Effects of solid distribution on the stiffness and strength of metallic foams," *Acta Materialia*, vol. 46, no. 6, pp. 2139–2150, mar 1998. [Online]. Available: https://www.sciencedirect.com/science/article/abs/pii/S1359645497004217

[60] ——, "The effects of cell face curvature and corrugations on the stiffness and strength of metallic foams," *Acta Materialia*, vol. 46, no. 11, pp. 3929–3935, jul 1998. [Online]. Available: https://www.sciencedirect.com/science/article/abs/pii/S135964549800072X

[61] I. Maskery *et al.*, "Insights into the mechanical properties of several triply periodic minimal surface lattice structures made by polymer additive manufacturing," *Polymer (United Kingdom)*, vol. 152, pp. 62–71, 2017. [Online]. Available: https://doi.org/10.1016/j.polymer.2017.11.049

[62] D.-J. Yoo and K.-H. Kim, "An advanced multi-morphology porous scaffold design method using volumetric distance field and beta growth function," *International Journal of Precision Engineering and Manufacturing*, vol. 16, no. 9, pp. 2021–2032, aug 2015. [Online]. Available: http://link.springer.com/10.1007/s12541-015-0263-2

[63] S. M. Giannitelli *et al.*, "Current trends in the design of scaffolds for computer-aided tissue engineering," *Acta Biomaterialia*, 2014. [Online]. Available: http://dx.doi.org/10.1016/j.actbio.2013.10.024

[64] S. Khaderi *et al.*, "The stiffness and strength of the gyroid lattice," *International Journal of Solids and Structures*, vol. 51, no. 23-24, pp. 3866–3877, nov 2014. [Online]. Available: https://www.sciencedirect.com/science/article/pii/S002076831400256X

[65] O. Al-ketan *et al.*, "On Mechanical Properties of Cellular Steel Solids with Shell-like Periodic Architectures Fabricated by Selective Laser Sintering," 2018.

[66] PC/104 Consortium, "PCI/104-Express and PCIe/104 Version 3.0," PC/104 Consortium, Tech. Rep., 2015.

[67] F. Calignano *et al.*, "Manufacturing of thin wall structures in AlSi10Mg alloy by laser powder bed fusion through process parameters," *Journal of Materials Processing Technology*, vol. 255, pp. 773–783, may 2018. [Online]. Available: https://www.sciencedirect.com/science/article/pii/S092401361830030X{#}bbib0055

[68] Special Metals Corporation, "INCONEL® alloy 718 www.specialmetals.com," Tech. Rep., 2007. [Online]. Available: http://www.specialmetals.com/assets/smc/documents/inconel{_}alloy{_}718.pdf

[69] Concept Laser, "CL 20ES Stainless steel," Concept Laser, Tech. Rep., 2017. [Online]. Available: www.concept-laser.de

[70] ——, "CL 100NB Nickel-based alloy," Concept Laser, Tech. Rep., 2017. [Online]. Available: www.concept-laser.de

[71] ——, "CL 41TI ELI Titanium alloy," Concept Laser, Tech. Rep., 2017. [Online]. Available: www.concept-laser.de

[72] ——, "CL 30AL / CL 31AL Aluminium alloys," Concept Laser, Tech. Rep., 2017. [Online]. Available: www.concept-laser.de

[73] GE Additive CL Orders, "AM Powder Pricing," Email.

[74] D. M. Buede and W. D. Miller, *The engineering design of systems: models and methods*. John Wiley & Sons, 2016.

[75] T. Irvine, "Bending Frequencies of Beams, Rods, and Pipes Revision S," 2012. [Online]. Available: http://www.vibrationdata.com/tutorials2/beam.pdf

[76] ASM Aerospace Specification Metals Inc., "ASM Material Data Sheet, 7075-T6." [Online]. Available: http://asm.matweb.com/search/SpecificMaterial.asp?bassnum=ma7075t6

[77] C. Garlisi *et al.*, "ASYS 632 Project: Proximity Detection," Air Force Institute of Technology, Tech. Rep., September 2018.

[78] G. P. Cimellaro and S. Marasco, "Tuned-mass dampers," *Geotechnical, Geological and Earthquake Engineering*, vol. 45, no. June, pp. 421–438, 2018.

REPORT DOCUMENTATION PAGE

Form Approved
OMB No. 0704–0188

1. REPORT DATE *(DD–MM–YYYY)*	2. REPORT TYPE	3. DATES COVERED *(From — To)*
22-03-2019	Master's Thesis	Sept 2018 — 21 March 2019

4. TITLE AND SUBTITLE

Application of Metamaterials for Multifunctional Satellite Bus enabled via Additive Manufacturing

5a. CONTRACT NUMBER

5b. GRANT NUMBER

5c. PROGRAM ELEMENT NUMBER

6. AUTHOR(S)

Macchia, Michael A., Captain

5d. PROJECT NUMBER

5e. TASK NUMBER

5f. WORK UNIT NUMBER

7. PERFORMING ORGANIZATION NAME(S) AND ADDRESS(ES)

Air Force Institute of Technology
Graduate School of Engineering and Management (AFIT/EN)
2950 Hobson Way
WPAFB OH 45433-7765

8. PERFORMING ORGANIZATION REPORT NUMBER

AFIT-ENY-MS-19-M-230

9. SPONSORING / MONITORING AGENCY NAME(S) AND ADDRESS(ES)

10. SPONSOR/MONITOR'S ACRONYM(S)

11. SPONSOR/MONITOR'S REPORT NUMBER(S)

12. DISTRIBUTION / AVAILABILITY STATEMENT

DISTRIBUTION STATEMENT A:
APPROVED FOR PUBLIC RELEASE; DISTRIBUTION UNLIMITED.

13. SUPPLEMENTARY NOTES

14. ABSTRACT

Space systems require materials with superior stiffness to weight ratios to provide structural integrity while minimizing mass. Additive manufacturing processes enable the design of metamaterials that exceed the performance of naturally occurring materials in addition to allowing the integration of non-structural functions. This research explored the use of a high stiffness, high density, small melt pool track width AM material, Inconel 718, to enable the production of metamaterials with finer features possible than can possibly be created using a lower density aluminum alloy material. Various metamaterials were designed utilizing thin wall triply periodic minimal surface infilled sandwich structures. The performance characteristics of these metamaterials were evaluated through modal analysis; demonstrating a 16-18% greater stiffness-to-weight ratio than 7075-T6 aluminium. These results were successfully applied to a multifunctional, lightweight, 3U CubeSat chassis design, fabricated from Inconel 718; resulting in a structurally mass efficient satellite bus. Additionally, modal analysis was conducted on the CubeSat chassis loaded with representative payload masses to evaluate the dynamic modal response of the final structure. Vibration testing was conducted in accordance with NASA General Environmental Verification Standard qualification standards, demonstrating the survivability of the chassis under launch conditions. It was shown this metamaterial based design approach could provide a lighter, stiffer chassis than manufactured from traditional aluminum alloy components.

15. SUBJECT TERMS

TPMS; CubeSat; Additive Manufacturing; Modal Analysis

16. SECURITY CLASSIFICATION OF:			17. LIMITATION OF ABSTRACT	18. NUMBER OF PAGES	19a. NAME OF RESPONSIBLE PERSON
a. REPORT	b. ABSTRACT	c. THIS PAGE			Maj Ryan O'Hara, AFIT/ENY
U	U	U	UU	150	19b. TELEPHONE NUMBER *(include area code)* (937)255-3636, x4542; ryan.ohara@afit.edu